HIGH INTENSITY LASER DEPOSITION OF
DIAMOND-LIKE CARBON THIN FILMS

By

FAN QIAN

A DISSERTATION PRESENTED TO THE GRADUATE SCHOOL
OF THE UNIVERSITY OF FLORIDA IN PARTIAL FULFILLMENT
OF THE REQUIREMENTS FOR THE DEGREE OF
DOCTOR OF PHILOSOPHY

UNIVERSITY OF FLORIDA

1996

To Kak, for her love and support.

ACKNOWLEDGMENTS

I wish to acknowledge the help from various people who made the completion of this study possible. First, I would like to thank my advisors, Dr. Rajiv Singh at the University of Florida and Dr. Peter Pronko at the University of Michigan, for giving me this unique opportunity to carry out the experiments as part of a collaborative research project between these two schools. Their constant encouragement and insightful guidance through out this intriguing yet sometimes strenuous endeavor are much appreciated. I owe my special thanks to Subrata Dutta, a fellow student whom I have been working with during the past two years. His help in setting up the experiments and his knowledge in laser optics have proven to be indispensable for this study. Together we have struggled through the oftentimes frustrating start-up period, battled with the customarily unpredictable laser system, and enjoyed the delight of a successful run. I would like to acknowledge the assistance I have received from some of the other students at the University of Michigan, including Paul, Marc, Detao, Jonathan, Rob, Anchun, Allen and Xinbin. Thanks also to my friends Don, Dongu, John, Rajan, Jenfon and Jakie at the University of Florida, who have kept me in touch with the school I am officially associated with.

During the course of this research project, I have received assistance from people beyond the scope of my daily contact. I would like to express my appreciation to Dr. Clark from the Applied Physics Department at UM, Mr. Mansfield and Mr. Rollins from the EMAL facility of UM, Dr. Weber from the Ford Research Laboratory, Dr. Brown from Oak Rridge National Laboratory, and Drs. Davis, Kowalchyk, and Pelletier from the Kaiser Optical Systems, for their help in some of the sample analyses.

Last but not least, I extend my thanks to the administrative staff I have been associated with at the Center for Ultrafast Optical Science, University of Michigan, whose courtesy and corporation made the days and months here more memorable. Marni, Fayne, Autumn, Serina, Tammy, Martha, Julie and Judy are among them.

TABLE OF CONTENTS

CHAPTERS

LIST OF TABLES

LIST OF FIGURES

Abstract of Dissertation Presented to the Graduate School
of the University of Florida in Partial Fulfillment of the
Requirements for the Degree of Doctor of Philosophy

HIGH INTENSITY LASER DEPOSITION OF
DIAMOND-LIKE CARBON THIN FILMS

By

FAN QIAN

August, 1996

Chairman: Rajiv K. Singh
Major Department: Materials Science and Engineering

We have deposited hydrogen-free diamond-like carbon (DLC) films at laser intensity in the 10^{14} - 10^{15} W/cm^2 range, with 100 femtosecond (FWHM) Ti:Sapphire laser beams. The films were studied with scanning probe microscopy (SPM), variable angle spectroscopic ellipsometry (VASE), Raman spectrometry, and electron energy loss spectroscopy (EELS). DLC films with good scratch resistance, excellent chemical inertness and high optical transparency in the infrared (IR) range were made at room temperature. As the laser intensity was increased from 3 x 10^{14} to 6 x 10^{15} W/cm^2, the films showed an increased surface particle density, a decreased optical transparency (85% $\rightarrow$ 60%) and Tauc bandgap (1.4 $\rightarrow$ 0.8 eV), as well as a lower sp^3 content (60% $\rightarrow$ 50%). The carbon ion kinetic energy was measured as a function of laser intensity with a Faraday ion collector. The time-of-flight (TOF) spectra exhibited a double-peak distribution, with a high energy suprathermal ion peak preceding a slower thermal component. The most probable ion kinetic energy demonstrated an $I^{0.55}$ dependence, when the laser intensity was

varied from 3×10^{14} to 6×10^{15} W/cm^2. The ion kinetic energy increased from 300 to 2000 eV within this range. The kinetic energy of suprathermal ions increased from 3 keV to over 20 keV and showed an $I^{0.33}$ dependence. These ions are speculated to have originated from an electrostatic acceleration field established by the suprathermal electrons, due to resonant absorption of the intense laser beams.

In comparison, we have deposited DLC films with conventional Nd:YAG laser beams (7 ns @ FWHM). These films also became more absorbing with decreased Tauc bandgaps (2.4 $\rightarrow$ 0.9 eV) and a deteriorating surface topography, as a function of increasing laser intensity in the 2×10^{10} - 6×10^{11} W/cm^2 range. TOF spectra of the nanosecond pulse induced plasma exhibited only a single peak distribution with no suprathermal ion peaks. The most probable ion kinetic energy increased with laser intensity from 200 to 1900 eV and exhibited an $I^{0.40}$ dependence. However, no significant difference in film quality was observed for the nanosecond Nd:YAG and femtosecond Ti:Sapphire laser beams.

CHAPTER 1
INTRODUCTION AND OVERVIEW

Background and Motivation

The interaction between laser beams and various forms of materials has been the subject of immense research efforts, ever since the invention of the lasers. Much attention has been directed at understanding the fundamentals of the laser-solid-plasma phenomena. The advances in laser plasma physics also led to various practical applications in this area. In the field of materials science, the use of laser beams to deposit thin films has shown great promise in the synthesis of many advanced materials.

As a member of the physical vapor deposition (PVD) family, pulsed laser deposition, or PLD, known for well over two decades, has gained prominence in the deposition of a wide variety of thin film materials. They include superconductors, semiconductors, dielectrics, metals, biomaterials, among others. In the PLD technique, a high-powered laser beam is directed onto a solid target, creating a high pressure, high temperature plasma with various excited target species (ions, neutrals, electronically excited atoms, clustered microparticles, etc.). The ensuing hydrodynamic expansion of this plasma in vacuum/gas medium leads to the deposition and growth of films with unique physical and chemical properties. This technique can deposit not only materials which reproduce stoichiometry and properties of the bulk target, but also films with desired properties very different from that of the starting material. The advantage of laser deposition lies primarily in the simplicity of system set-up, good deposition parameter control, low contamination level, and possible low temperature epitaxial growth.

1

The deposition characteristics of PLD differ significantly from conventional thermal evaporation methods. The PLD technique is first distinguished by the formation of a high temperature (10^4 - 10^5 K) plasma, and ejected target species with high charged states and high kinetic energies (~10 - 1000 eV, which is approximately one to three orders of magnitude higher than the energies expected from conventional evaporation methods), followed by the forward-directed nature of the ablated materials. The energetic nature of laser induced plasma is believed to have played an important role in synthesizing certain thermodynamically metastable materials, such as diamond-like carbon (DLC), cubic silicon carbide (c-SiC), and cubic boron nitride (c-BN), etc.

DLC film, a unique form of carbon, has drawn great attention over the years, primarily due to its prospect as an alternative to diamond films. While DLC films may be inferior to diamond in terms of thermal stability, their microhardness, chemical inertness, and optical transparency in the infrared (IR) and partially in the visible spectrum are quite similar. In addition, a smoother surface topography, better adhesion to the substrates and relative ease in fabrication have made DLC films a more desirable choice in certain applications.

Most successful PLD depositions of DLC thin films conducted so far have employed either excimer lasers (KrF, ArF, XeCl, etc.), or Q-switched solid state lasers such as various frequency modified Nd:YAG beams. These lasers all have pulse duration in the nanosecond range. Depending on the laser energy and beam diameter focused on the target, laser intensities in the 10^8 - 10^{11} W/cm^2 range are most commonly achieved. Past experiments have indicated that at this intensity range, the diamond-like component, i.e., the fraction of sp^3 bonded carbon atoms increased as a function of increasing laser intensity. The plasma formed under these conditions was found to consist of ionized carbon particles with moderately high kinetic energies, increasing from several electronvolts up to several hundreds of electronvolts as a function of increasing laser intensity. On the other hand, as a kinetic condensation process, formation of the

metastable diamond-like sp^3 bonding structure is expected to be destroyed under excessive high energy ion bombardment. In other words, the more stable sp^2 graphitic structure will again be favored under such conditions. For the nanosecond lasers, however, this reversion phenomenon has yet to be clearly demonstrated. Because substantially higher laser energy is often of very limited availability, while submicron beam spot required to achieve higher intensity is limited by diffraction and coherence effects.

This motivated us to look into new laser systems which can produce higher intensity levels. Instead of nanosecond lasers, we have deposited DLC films using laser beams with a 100 femtosecond (FWHM) pulse duration. The laser system employed in our study was a solid state Ti:Sapphire laser system developed at the Center for Ultrafast Optical Science, University of Michigan. It is based on the latest chirped pulse amplification (CPA) techniques. By using this system, we were able to push the intensity up to the 10^{14} - 10^{15} W/cm^2 range with moderate laser energies. The laser plasma created under these conditions was studied through time-of-flight (TOF) experiments. This study was intended to establish a correlation between the carbon ion kinetic energy and the DLC film properties, as a function of laser intensity. Similar experiments were also conducted using a conventional Q-switched Nd:YAG laser (7 ns @ FWHM) beam, which served as a reference system to that of the femtosecond study.

Femtosecond laser deposition of thin film materials remains a largely unexplored territory in the field of materials science. These ultrashort laser pulses enable the generation of extremely high laser intensities, which may have significant application for the synthesis and processing of advanced materials such as DLC. Though certain similarities will be present, the laser-matter-plasma interactions associated with the ultrashort femtosecond pulses are expected to be distinctively different from that in the nanosecond regime. Most research efforts so far are limited to the phenomena associated with high field plasma physics. These include high-harmonic generation, high-brightness, short pulse X-rays formation and wakefield plasma acceleration. With the advance of

ultrashort laser techniques, scientists are just beginning to explore their potential value in the areas of thin film deposition, micromachining, as well as medical-surgical procedures.

Due to the lack of comparable information, on the subject of femtosecond laser deposition of thin films, we have limited our investigation to the study of DLC film deposition characteristics. This approach is merited by the findings that DLC film quality is a strong function of the laser intensity for nanosecond laser pulses. Our intention in this study was to look beyond the relatively matured nanosecond laser deposition techniques, into an area where new phenomena associated with the ultrashort laser-matter interactions may be beneficial to the synthesis of advanced materials such as DLC, c-BN, and β-C_3N_4.

Dissertation Outline

The primary objective of this study was to investigate the effects which a high intensity, femtosecond laser generated plasma would have on thin film materials. Diamond-like carbon (DLC), because of its monoatomic nature and relatively well established correlation between the film properties and laser intensity in the nanosecond range, was chosen as the model material.

Chapter 2 first gives a general review on the subject of diamond-like carbon thin film depositions. This includes an introduction to the DLC concept, its atomic structure and properties, accompanied by a discussion of the state of the art deposition techniques and associated film formation mechanisms. Aspects of the laser-solid-plasma interactions within the intensity regime relevant to those used in our study are discussed.

Chapter 3 accounts for the experimental aspect of this study. A detailed description of the unique femtosecond Ti:Sapphire laser system is given. Deposition system set up and DLC thin film deposition conditions are outlined, followed by a discussion of the time-of-flight (TOF) experiments.

Chapter 4 presents the results of each experiment described in Chapter 3, including the carbon ion kinetic energy measured as a function of laser intensity through TOF, and DLC film properties characterized by various techniques. Topics relevant to these results are discussed.

The conclusions from this dissertation are summarized in Chapter 5.

CHAPTER 2
LITERATURE REVIEW

Diamond-like Carbon (DLC) Thin Films

Structure and Property

Carbon atoms, when bonded with each other, have three basic types of electron hybridization: one-dimensional sp^1 bonding in an acetylene like structure, trigonal sp^2 bonding in a layered, threefold graphite structure, and tetrahedral sp^3 bonding found in a fourfold-coordination diamond structure.

In a tetrahedral diamond structure, the four L shell carbon electrons in the 2s and 2p orbitals are reconfigured: one of the two 2s electrons is elevated to the 2p orbital, the three electrons in the 2p orbital then recombine with the remaining 2s electron, giving rise to four new sp^3 orbitals. These hybrid atomic orbitals are labeled sp^3 since each one is now a combination of one s and three p orbitals. The sp^3 orbital configuration allows the development of an extremely strong bond when combined with a sp^3 orbital from another carbon atom. The concentration of these bonding electrons optimizes the repulsive and attractive forces between themselves and both carbon nuclei. By convention, a directional sp^3 orbital is called a sigma (σ) orbital, and the bond a σ bond. Every tetrahedron of these hybridized sp^3 atoms combines in space with four other carbon atoms at an angle of $\sim109°$ to form the three dimensional diamond lattice structure, as shown in Figure 2-1 [1]. Each carbon atom in a diamond structure is therefore said to be sp^3 bonded and has four σ bonds. The sp^3 C-C bond in diamond has a bond length of 1.54 Å and a bond energy of 370 kJ/mol.

6
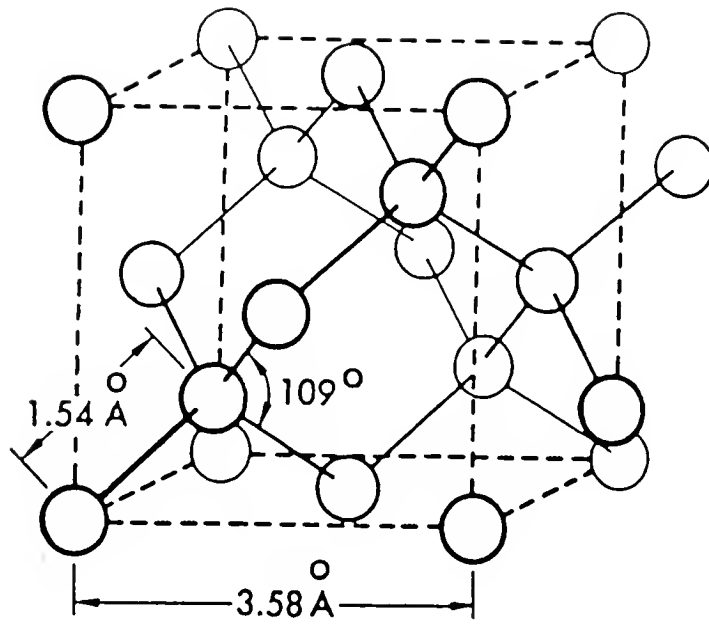
Fig. 2-1 Lattice structure of diamond.
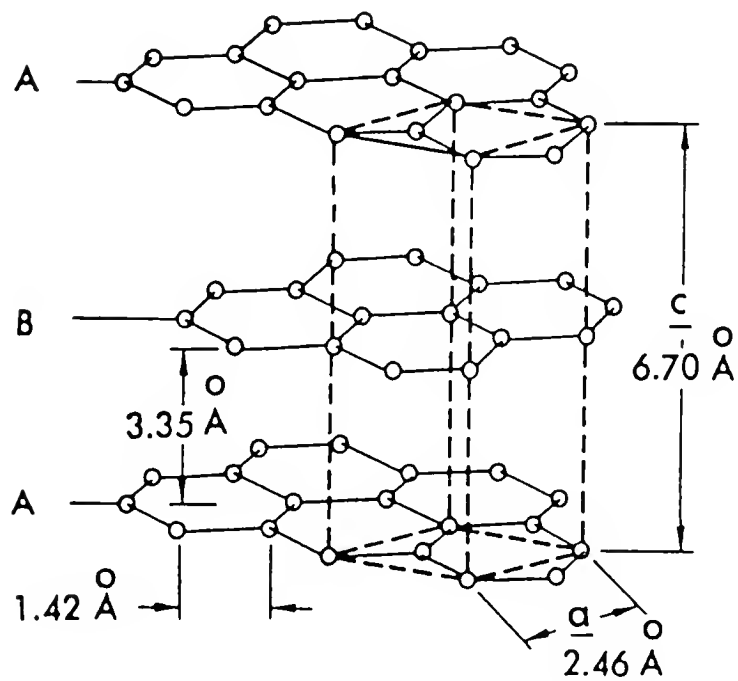
Fig. 2-2 Lattice structure of graphite.

In a graphitic carbon structure, one of the two ground level 2s electrons is excited and combined with the two 2p electrons to form three hybrid sp^2 orbitals, plus a fourth unhybridized free 2p orbital electron. The three sp^2 orbitals form a 120° angle from each other in the same plane. Each sp^2 orbital is called a σ orbital and the bond a σ bond. The fourth non-hybridized p electron forms a non-symmetrical orbital perpendicular to this plane, and it is available to form a subsidiary π bond with other carbon atoms. This configuration is responsible for the layered hexagonal lattice structure of graphite in space, as illustrated in Figure 2-2 [1]. Each carbon atom in a graphite is said to be sp^2 bonded and has three σ bonds and one π bond. The σ and π bond in graphite have a bond length of 1.42 Å and 3.35 Å, respectively. The σ bond in graphite is thus shorter and with a bond strength of 570 kJ/mol, is even stronger than that of diamond, due to the more overlapped sp^2 electron density configuration in graphite. The π bonds, however, are much weaker with a bond energy of only 7 kJ/mol. These frail van del Waals π bonds are responsible for the softness of graphitic materials.

Similarly, in an acetylene like structure, one 2p electron combines with an excited 2s electron to form two sp^1 hybridized orbitals. These sp orbitals form an angle of 180°, making the sp molecule linear in space. Each carbon atom is said to be sp^1 bonded and has two σ bonds and two π bonds.

As a result of these different bonding structures, carbon has several allotropes. They include graphite, diamond, and fullerene molecules. Another form of carbon, most commonly known as diamond-like carbon, or DLC, can be considered as its fourth allotrope. The name diamond-like is arguably originated from the work of Aisenberg and Chabot [2], who first deposited hard carbon films with properties determined to be similar to that of diamond. Ions extracted from a carbon arc in argon were used in their experiment. Subsequent work by other researchers led to an explosive growth of interest in this unique material.

DLC can be considered as a metastable form of carbon covering the spectrum between diamond and graphite. But unlike crystalline graphite or diamond, which respectively consists of 100% sp^2 hybridized carbon atoms and 100% sp^3 hybridized carbon atoms, DLC films have a mixture of sp^3 and sp^2 hybridized bonds and are generally amorphous. This is due to the lack of a long range order of the sp^3 and sp^2 bonds in DLC films. On the other hand, DLC films possess properties similar to those of diamond rather than graphite, including high mechanical hardness, high electrical resistivity, excellent chemical inertness and optical transparency. For these same reasons, they have been one of the most actively researched thin film materials over the past two decades, as an alternative to diamond coatings.

Diamond-like carbon films can be broadly categorized into two forms:

1. Hydrogenated DLC (a:C-H, 'a' as amorphous) prepared using hydrocarbon gas mixtures, mainly through chemical vapor deposition (CVD) techniques.

2. Hydrogen-free DLC (a:C) films fabricated through physical vapor deposition (PVD) processes, using a solid graphite target.

Hydrogenated DLC films (a:C-H) are often deposited at elevated temperatures with a mixture of hydrogen and various kinds of hydrocarbon agents, such as methane, ethylene, or acetylene [3-5]. Most commonly used techniques in making these films include hotfilament discharge, DC glow discharge, RF plasma discharge and other variations of similar CVD processes. The deposition mechanism is thought to be similar to that of CVD diamond. The presence of dissociated atomic hydrogen is believed to preferentially remove sp^2 bonds, thus in effect promote the growth of diamond-like sp^3 bonds. Hydrogenated DLC films usually contain planar sp^2 hybridized carbon clusters that are interconnected by tetrahedral sp^3 bonds in a random fashion. These films often contain a large amount of hydrogen varying from about 10% up to 60%, and they are considerably softer than diamond [6]. The ratio of the sp^3/sp^2 bonds was found to scale with the percentage of hydrogen in the films [7,8]. A reduction of hydrogen concentration causes

degradation toward graphite [9].

Hydrogen-free DLC films (a:C) are most commonly deposited through ion beam sputtering [10], direct ion beam deposition [11], magnetron sputtering [12], cathodic arc discharge [13], and pulsed laser depositions (PLD) [14]. These films are hard, chemically inert, and optically transparent in the infrared (IR) and near IR spectrum. They usually have a somewhat higher film density but lower optical bandgap when compared with hydrogenated DLC films.

A common feature amongst various PVD deposition processes is the presence of ionized carbon species in the plasma. The bombardment of the exposed substrates with these ions, which often have medium kinetic energies ranging from tens to hundreds of electronvolts, has proven to be instrumental in attaining a condensed structure with a high volume fraction of sp^3 bonded carbon atoms. One inherent advantage to these non-equilibrium techniques, where the plasma kinetic energy is much higher than that achieved by purely thermal methods, is that substantially lower substrate temperatures are required for these processes. This makes it possible to deposit high quality DLC films on heat sensitive materials. Also, virtually free of C-H absorption bands, these hydrogen-free DLC films offer some unique advantages when used in certain optical applications because the scattering losses are greatly reduced. The growth of these a:C films is self-seeding at room temperature, and substrates require little or no preliminary preparation. Wear and tribological applications also benefit from the low surface friction generally displayed by these films. In this case, they are better suited than CVD diamond films which have rough facets and routinely require high growth temperatures.

The concept of DLC is very inclusive. It comprises a tremendous amount of carbon-based thin film materials. Their structures often depend upon the preparation methods. As a result, the properties of these DLC films vary drastically from one another. However, two parameters are considered to have the most impact on DLC film quality, regardless of the deposition technique: kinetic energy and elemental composition of the

primary plasma. For hydrogenated DLC films, as the impact energy increases, one obtains material from graphitic polymer to dense hydrocarbon to dense a:C-H. For a:C films, sp^2 based carbon films are expected at low energies and diamond-like sp^3 based films at higher energies. An ion beam or plasma generated from a solid carbon target generally contain various types of polyatomic ions, neutrals, and electronically excited carbon microclusters (C_n^{m+}, C_n, etc.). In certain sputtering processes such as ion beam assisted deposition or laser deposition, the carbon energy usually has a Maxwellian-like distribution. The polyatomic species at the low energy tail sometimes do not have enough energy, upon impact to overcome their binding energies and break up into monoatomic particles at the substrate surface. This could contribute to the development of undesirable surface particulates and also suppress the sp^3 bonding formation that is believed to be favored by energetic/monoatomic ions. Similar notions hold when hydrocarbon sources used in the CVD processes are considered. Species of the general form C_xH_y, $(C_xH_y)_n^+$, etc. can be present in the plasma. Though the structure of these hydrocarbon precursors are often not well known, the deposited a:C-H films are rarely found to depend on the type of hydrocarbon used as the carbon source.

Table 1 summarizes some of the DLC film properties as well as those of diamond, CVD diamond, and graphite.

Applications

Due to their unique microstructure with high percentage of sp^3 bonded atoms, DLC films possess many properties comparable to that of diamond. Some of their most notable assets include high hardness, low friction, high electrical resistivity, excellent chemical inertness and good optical transparency in the IR and near IR wavelength. They are beginning to find usage in a wide range of areas. The following sections briefly discuss some applications of the DLC films.

Table 1. Properties of diamond, CVD diamond, graphite and DLC.

	Diamond	CVD diamond	Graphite	a:C	a:C-H
Density (g/cm^3)	3.51	3.3 - 3.5	2.2	1.6 - 3.1	1.5 - 2.0
Hardness (kg/mm^2)	10000	6000 - 10000	-	1200 - 8500	1200 - 5000
Bandgap (eV)	5.45	5.0 - 5.5	0.0	0.0 - 2.6	1.2 - 2.5
Resistivity (ohm-cm)	$10^{16} - 10^{18}$	$10^{12} - 10^{-17}$	$10^{-5} - 10^{-6}$	$0 - 10^{16}$	$10^5 - 10^{16}$
Refractive index (@ 632 nm)	2.42	2.2 - 2.4	~3.0	1.6 - 2.4	1.8 - 2.2
Microstructure	crystalline	crystalline	crystalline/ amorphous	amorphous	amorphous
Thermal stability	metastable	metastable	stable	metastable	metastable
Bonding structure	100% sp^3	~100% sp^3	100% sp^2	sp^3/sp^2	sp^3/sp^2/sp^1

Wear and tribological. Because of their superior hardness and extremely low friction coefficients (< 0.04 at low humidity), DLC films can be used as wear reducing coatings [15]. A DLC coated silica optical fiber can inhibit the permeation of moisture, thus reduce the risk of brittle fracture [16]. Ion beam deposited DLC coatings have found commercial use as protective/decorative layers on polycarbonate sunglasses, where they were found to be more scratch resistant than most other coatings [17]. Overcoat for magnetic thin film recording disks is yet another possibility for DLC films [18,19], because of their excellent

surface smoothness and hardness.

Optical. Though DLC films are less transparent than diamond in the visible spectrum, they nonetheless have high transparency in the IR and near IR range. Moreover, DLC films can be made at low temperatures and have an atomically smooth surface, making them more suited as protective coatings for IR windows. On the other hand, CVD diamond can only be deposited at relatively high substrate temperatures, thus limiting the available optical windows for use as substrates. In addition, because CVD diamond films often display growth facets with roughness up to several microns, extensive post-deposition modification of the film surface is also required to minimize light scattering. ZnS and ZnSe IR windows coated with DLC films were found to be highly transparent in the 3 - 15 μm range and exhibited large improvement in chemical and abrasion resistance over uncoated ones [17]. DLC could suit well as protective layers for similar soft IR windows such as MgF_2, Ge, and CdTe, allowing them to be used in a corrosive environment. By varying the refractive index of DLC films, they can also be used as anti-reflection (AR) IR window coatings. Furthermore, due to their high damage threshold, hard DLC films with high sp^3 content could serve well as protective layers for high-power laser windows [20].

Microelectronics. DLC films with high extinction coefficients have a dark appearance and they have been used to provide an increased contrast enhancement ratio in liquid-crystal displays (LCD) [21]. With a high electrical resistivity and breakdown voltage up to 10^6 V/cm, DLC films are being used as insulating layers in some electronic devices. These include high-energy-density, high-voltage capacitors [22], metal-insulator-semiconductor (MIS) devices [23], as well as metal-insulator-metal (MIM) devices [24]. DLC films are also being considered as photoresists in lithographic applications. Through selective graphitization of DLC film by laser/oxygen exposure, the patterned DLC film can act as an in-situ mask for underlying silicon substrates [25].

Biological and medical. DLC is a biocompatible material [26]. It may find use as biomedical coatings for heart implants, hip joints and other prostheses.

High internal stress and relatively low thermal stability are among the factors limiting the usefulness of DLC films. Hydrogen-free DLC films deposited with ion beam or lasers routinely have compressive stress up to several gigapascals. This high internal stress prevents the deposition of DLC films beyond a few microns on rigid substrates. The compressive stress depends strongly on preparation method. It increases with film thickness and is relieved through peeling and buckling of the films [27,28]. Compressive stress also contributes to poor adhesion between the DLC film and the substrate. This problem, however, can be alleviated through the deposition of carbide-forming materials such Si, Ti, W, or Ge as buffer layers. Alternatively, a better film adhesion can be achieved by increasing the carbon ion energies to form an intermediate carbide layer at the interface.

Most DLC films exhibit high hardness, low optical absorption and high electrical resistivity at room temperature, but their properties rapidly deteriorate at elevated temperatures. A graphitization process starts at a couple of hundred degrees Celsius. This thermal annealing process breaks down the tetrahedral sp^3 bonds and encourages the carbon atom diffusion to form trigonal sp^2 bonds, which are thermodynamically more stable. Transformation from DLC to a fully graphitic structure is completed at about 500 to 600 °C, at which point the films become soft, electrically conductive, and highly absorbing. Hua et al. have deposited DLC films with a KrF excimer laser beam (248 nm, 12 ns FWHM), at a laser intensity of 8×10^8 W/cm^2 [29]. They measured the film density as a function of substrate temperature, using the grazing-angle X-ray reflectivity technique. From 22 °C to 300 °C, the film density was found to have decreased from 3.1 g/cm^3 to 2.4 g/cm^3 (corresponding to sp^3 fractions of 77% and 17%, respectively), along with a decline of optical bandgap from 2.2 eV to 0 eV. This observation clearly indicated a graphitization process in progress. In an earlier experiment conducted by Capano et al.

[30], a KrF excimer laser (248 nm, 25 ns FWHM) was used to deposit DLC films at substrate temperatures ranging from room temperature to 600 °C. Raman spectroscopy and grazing-angle X-ray reflectivity technique, respectively, were used to study the DLC microstructure and film density. A graphitization process was observed to have occurred at temperatures higher than about 200 °C, leading to a decreased film density [31]. Similar findings were reported by Ong et al. [32].

Though many applications are being discovered for diamond-like carbon films, industrial scale deposition of DLC films has so far been very limited. This is largely due to the fact that there still lacks a suitable technique, which can sustain a reasonable deposition rate without compromising the film quality. Instead, the current state of research has mainly been focused a somewhat different subject: what is the deposition mechanism that leads to the best film quality, i.e., DLC films with the highest sp^3 bonding contents?

Deposition Mechanisms

Maximization of the diamond-like sp^3 bonding content has been a main objective in making DLC films. Ever since the successful synthesis of CVD diamond, much attention has been directed at finding a suitable low pressure, low temperature technique for the deposition of DLC films. This is because both DLC and diamond contain the metastable sp^3 bonds. The deposition mechanism for the stabilization of sp^3 versus sp^2 bonding structure in a DLC film is still under dispute, not unlike the situation on CVD diamond film depositions several years ago. Various deposition techniques have been tested, generating a vast amount of information on the DLC film properties as a function of deposition parameters. From these experimental results, several models on the formation and stabilization of sp^3 bonds have been proposed. Some of the most notable include:

1. Preferential sputtering of sp^2 versus sp^3 sites, first proposed by Spencer et al. from an earlier DLC work in the 70's [33];

2. Stabilization of the sp^3 structure due to high intrinsic stress in DLC film, suggested by McKenzie et al. [34,35];

3. Sp^3 bonding formation resulting from energetic carbon ion quenching on substrates, proposed by Robertson [36].

In the preferential sputtering model, Spencer [33] hypothesized that the tetrahedral sp^3 bonds will be more resistant to sputtering than the trigonal sp^2 bonded carbon atoms. At ion impact energy range of 50 - 500 eV, the incident ion flux can simultaneously deposit new carbon materials and resputter non-sp^3 structures during film growth. Lifshitz et al. [37] offered a similar "sub-plantation" mechanism based on the estimation that the displacement threshold for graphitic carbon atoms is less than half that of diamond (30 eV vs. 80 eV). Thereby a preferential displacement of the sp^2 sites by influx ions would eventually lead to an accumulation of the sp^3 sites. However, neither of these two models could explain the initial nucleation of sp^3 bonded structure. They also have ignored the fact that resputtering of the sp^2 bonds is an unlikely event at the energy range considered because carbon has extremely low sputter yield when compared to other materials [38,39]. Moreover, the large difference between the suggested displacement threshold of graphite and diamond sites was also put into question, by a more recent measurement from Koike et al. [40], who found both of them to be approximately 40 eV.

Through their work on mass-filtered, plasma vacuum arc deposition of DLC films, McKenzie et al. [34] presented a stress induced sp^3 formation mechanism. They suggested that the high compressive stress generated by energetic ion impact could serve as the driving force for converting sp^2 bonds to the metastable sp^3 bonding structure, in the interior of DLC films. This proposition was based on the pressure-temperature phase diagram of diamond and graphite. They found in their experiment that by negatively biasing the substrate at between 20 and 70 V, a maximum compressive stress of 7 GPa was present inside the films. These DLC films had a maximum density of 3.1 g/cm^3, corresponding to a sp^3 bonding percentage of 70%. If the substrate bias was lower than

20 V or higher than 70 V, the compressive stress was found to fall back to lower values, accompanied by a decrease in film density. The exact ion charge state was not clearly stated in their experiment, as the mass filtering mechanism did not provide a complete selection of single species. However, if assuming singly charged C^+ ions are the predominant species in the ion beam, one concludes that the highest sp^3 bonding percentage can be expected at an ion kinetic energy between 20 and 70 eV.

Kelires' [41] work appeared to support the above observation. He concluded that the high intrinsic stress in ion deposited DLC film was a result of high free energy of the sp^3 sites. These sp^3 sites in DLC films have a free energy approximately 0.3 eV higher than that of the sp^2 sites. The extra free energy can introduce a compressive stress of up to 15 GPa in the film. This intrinsic stress can be interpreted as the work done by incident ions to compress/convert the sp^2 sites to sp^3 sites in the McKenzie model.

More recently, Robertson [36] has suggested a coupled energetic ion condensation /thermal quenching model. He reasoned that the bonding hybridization in a DLC film would adjust itself according to the local density: more sp^2 bonds at lower density and more sp^3 bonds at higher density. A high film density requires an incident carbon ion to have at least enough energy to penetrate the first few atomic layers and enter an interstitial site. The accumulation of these ions will lead to an increase in the local film density. As a result, the local bonding will reform around these sites to become bulk bonding at the appropriate bonding hybridization, i.e., DLC film with high sp^3 contents. Conversely, if the ions have excessively high energies, they will be able to penetrate deeper into the layers. The potential film density increment induced by these ions, however, will not be able to materialize due to the lack of a sufficient energy dissipation mechanism in the local area. A thermal relaxation process will instead take over, resulting in a decreased film density and hence an overall more graphitic bonding structure with mostly sp^2 bonds. Using a thermal spike model to describe the density increment/reduction process, he obtained an estimated optimal ion kinetic energy of 60 eV.

Fallon et al. [42] have, in a related experiment, observed this energy to be around 140 eV using a mass-filtered, singly charged C^+ ion beam.

Rossi et al. [43] have also conducted similar experiments and they later determined that the optimum carbon ion energy to be somewhere between 150 and 200 eV.

Laser Deposition of DLC

Ion beam deposition (IBD) of DLC films, using a mass-filtered carbon ion beam has attracted much attention as of late. State of the art IBD techniques have been able to produce hydrogen-free DLC films with up to 75% sp^3 carbon bonds, as well as high hardness and electrical resistivity, as demonstrated by the work of Fallon and Rossi [42,43]. A relatively precise control over the carbon ion kinetic energy distribution and its charge state is the main advantage of this technique. However, a low deposition rate (up to several tens of nanometers per hour at best) continues to be its drawback. Over the past few years, another versatile thin film deposition technique called pulsed laser deposition, or PLD, has emerged as a worthy alternative in making DLC films with comparable qualities.

In a typical pulsed laser deposition process, a solid target is irradiated by a high-powered laser beam in a high vacuum environment. Target materials are removed by the intense laser beam in the form of a highly excited plasma. Due to the large pressure gradients present within the hot plasma, it expands rapidly in a beam-like fashion in front of the target surface. This plasma is then allowed to condense onto a substrate placed at a short distance away from the target. Background gas pressure up to several hundred millitorr and/or elevated substrate temperatures are sometimes applied to achieve desired deposition rate and film properties. The usefulness of the PLD technique resides primarily in its simplicity in set up and the ability to generate a highly energized plasma, the latter being the key to the formation of metastable materials such as DLC.

Early attempts to make DLC films with laser beams were initiated by Fujimori et al. in the early 80's [44,45]. They used a continuous wave (CW) CO_2 laser to vaporize a powdered graphite target. Carbon films were deposited onto fused silica substrates at room temperature, with a laser intensity of 5 x 10^3 W/cm^2. Only conductive, graphitic films were formed at first. They were then able to improve the film quality, indicated by higher film electrical resistivity and optical transmittance, by introducing a simultaneous Ar ion bombardment on the substrate. In light of these results, subsequent research efforts have since shifted to further increase the laser-solid energy coupling, with laser sources capable of generating much higher intensities. Pulsed excimer lasers, with their combined features of moderately high energy and short pulse duration, became a logical choice. The experiments carried out in the mid-80's by Marquart [46], Pompe [47], and Sato [48] earmarked the maturing of PLD technique in making DLC films.

The research groups led by Marquart [46] and Pompe [47], respectively, used Q-switched nanosecond Nd:YAG lasers in their experiments. Marquart et al. [46] were able to produce DLC films at peak laser intensities ranging from 3 to 13 x 10^{10} W/cm^2. The extinction coefficient and optical bandgap of their films were measured to be 0.3 and 0.4 eV, respectively. They studied the plasma electron temperature as a function of laser energy, by taking X-UV emission spectra during deposition. Scratch resistance tests were also performed on the DLC films. They discovered that both the plasma electron temperature and the film hardness increased as a function of increasing laser energy. The electron temperature and film hardness appeared to have reached a maximum value at laser intensities of 5 x 10^{10} W/cm^2 and higher. This observation prompted them to conclude that there existed a threshold laser intensity of 5 x 10^{10} W/cm^2, beyond which hard, diamond-like carbon films were formed, and below which only soft, graphitic ones were made. They further suggested that a plasma electron temperature of 40 eV, measured at the threshold laser intensity of 5 x 10^{10} W/cm^2, coincided with the resputtering energy for sp^2 bonded carbons as proposed by Spencer [33] in the

preferential-sputtering mechanism. Pompe et al.[47] also asserted that carbon films with some diamond-like characteristics could be deposited with Nd:YAG laser pulses. Raman spectroscopy was used for the first time as an analytical tool in DLC film characterization, by linking the Raman band position to the presence of sp^3/sp^2 carbon bonds. However, Pompe's experiment did not report any direct measurement of the film properties such as film transmittance or hardness. The laser intensities used in their experiments were also lower than the critical value of 5 x 10^{10} W/cm^2 observed by Marquardt.

Sato et al. [48] took a slightly different approach by employing a XeCl excimer laser (308 nm, 10 ns FWHM) to deposit DLC films. Typical peak laser intensity used in their experiment was estimated to be 3 x 10^8 W/cm^2, well below the critical density of 5 x 10^{10} W/cm^2 observed by Marquardt [46]. Quality DLC films with an electrical resistivity up to 10^8 Ω-cm, an optical bandgap of 1.4, and a refractive index of 2.1 - 2.2 were obtained at substrate temperature of 50 °C. Higher substrate temperatures produced only opaque and conductive carbon films. At even higher laser intensities an increase of the deposition rate was compromised by the presence of higher particle densities on the film surface. One notable feature emphasized by these researchers was the presence of small percentage of carbon ions (estimated to be ~ 0.01%) in the laser induced plasma. The authors went on to suggest that this ionized plasma was likely to be responsible for the production of carbon films with diamond-like characteristics. This is believed to be the first time a direct correlation between the DLC film quality and an ionized plasma was established.

The late 80's and early 90's saw an explosion of research activities in the laser deposition and characterization of DLC thin films. Several research groups, notably those led by Collins [49], Pappas [50], and Murray [51] have been among the most active in this area.

After realizing that a highly activated laser plasma is the key to produce carbon films with substantial diamond-like properties, researchers began to direct their focus to

further enhance the laser induced plasma. By doing so, they hoped to increase the degree of plasma excitation and to improve the uniformity of the strongly forward-directed laser plume. Several different paths were taken, including the use of laser beams with different wavelengths, deposition at higher laser intensities, and the addition of auxiliary plasma enhancement devices. A combination of these methods led to the so-called hybrid pulsed laser depositions.

Two of the most widely adopted hybrid techniques were introduced by Collins [49] and Krishnaswamy [52], respectively. The basic idea behind their modifications was the implementation of supplementary electrical discharges to the laser plasma.

Collins et al. [49] used a Nd:YAG laser (15 ns FWHM) operated at the fundamental wavelength of 1064 nm in their experiment. Peak laser intensity up to 5 x 10^{11} W/cm^2 was found to be necessary to produce quality DLC films. Furthermore, they incorporated an auxiliary discharge to further increase the laser plasma temperature by Joule heating in the volume of the ablation plume. A voltage ranging from - 2000 to 2000 V was applied to the discharge electrode placed between the target and substrate. When the space between the target and substrate was filled with laser induced plasma, a strong discharge plume with current up to 10 A was measured. A Rogowski coil was used to monitor the current change during the plume discharge. With this set up they were able to produce optically smooth DLC films at growth rates of up to 0.5 μm/hr over an area of 20 cm^2. In several ensuing experiments using the same technique, Davanloo et al. [53,54] claimed to have deposited a unique form of hydrogen-free DLC film, which appeared as a conglomerate of fined grained particles. These particles, when studied under a scanning tunneling electron microscope, were found to have grain sizes ranging from 100 to 200 Å. They were speculated to be constructed of diamond-like sp^3 bonds while the intergrainular material was made of defected graphite. The DLC film quality was found to depend strongly on the nature of the laser induced plume. Close to the center of the forward-directed plasma, where the carbon ions have the highest charge states/kinetic energies, one

obtained DLC films with the best optical transparency (with an extinction coefficient of 0.16 and an optical bandgap of 1.15 eV) and microhardness (with a film density of 2.9 g/cm^3 and a hardness of 1500 kg/mm^2). Higher laser intensities also resulted in lower extinction coefficients and higher optical bandgaps. Growth rate of 0.5 µm/hr over a 100 cm^2 area was obtained on various substrates, including Si, Ge, ZnS, and glass. The authors later termed these DLC films as 'amorphic diamond' to distinguish them from those deposited from ion beam deposited DLC films. In a more recent paper presented by the same research group[55], the authors showed the TEM picture of a gold coated replica of the "amorphic diamond" film. It was compared with that of a DLC film condensed from a mass separated C$^+$ ion beam with a kinetic energy of 2 keV. The topography of these "amorphic diamond" (alternatively termed as "nanophase diamond" by these authors) films appeared to more closely resemble that of a polycrystalline diamond structure: the nodules seemed to be disordered mixtures of the cubic and the rare hexagonal polytype (Lonsdaleite) of diamond. The authors went on to theorize that at laser intensities higher than about 10^{11} W/cm^2, the predominant species generated near the target surface would be multiple charged C^{3+} and C^{4+} ions. These highly charged carbon ions expanded in vacuum with their charge states frozen in, giving rise to a high energy ion source at distances up to 10 cm away from the target. The energetic condensation of these C^{3+} and C^{4+} ions, which possess kinetic energies up to 2 keV, facilitated the formation of the "nanophase diamond" structure. This energetic condensation process was also believed to have resulted in a unique chemical bonding, such that little residual compressive stress (0.7 - 0.8 GPa) was measured in the film. The film hardness was estimated to have a minimum value of 8000 kg/mm^2. This experiment is presumed to be the biggest success in making hydrogen-free DLC films to date. However, by closely examing some of the claims by these researchers, one finds areas of controversy that need to be further investigated. These include the "polycrystalline diamond" microstructure of the films, the presence of multiple-charged carbon ions as the predominant plasma species,

as well as the absence of neutral or clustered microparticles in the laser plasma. Though high intensity laser plasma has been found to generate carbon species with moderately high kinetic energies, the presence of multiple-charged ions such as C^{3+} and C^{4+} at a distance up to 10 cm away from the plasma source has yet to be experimentally confirmed. Moreover, if the microstructure of this "nanophase diamond" is indeed that of polycrystalline diamond, a film density measurement should have yielded a value substantially higher than 2.9 g/cm^3 observed in their experiments. The absence of any microstructual techniques, such as Raman spectroscopy or X-ray diffraction to verify the existence of diamond structure has left several unanswered questions as well.

Krishnaswamy et al. [52] have deposited DLC films using a XeCl excimer laser beam (308 nm, 40 ns FWHM). They employed a capacitor-discharge hybrid technique: a 0.5 μF capacitor was connected between a graphite ring electrode (2 cm in diameter, positioned at 0.65 cm away from target) and the graphite target. The capacitor was charged by a high DC voltage supply at up to 3000 V. This capacitively stored energy was automatically released when the laser plume filled the space between the target and substrate. A large discharge plume extending from the ablated spot onto the substrate was observed, indicating a further activation of the laser plasma. The enlarged plume led to a better film uniformity on various substrates. Insufficient data were available to compare the film qualities deposited with and without the plasma enhancement modifications.

Leppävuori et al. [56] also deposited DLC films with a XeCl excimer laser (308 nm, 20 ns FWHM), without any additional laser enhancement modification. They demonstrated that the best quality DLC films were made at room temperature with the highest available laser intensity of 8 x 10^9 W/cm^2.

Pappas et al. [50] have synthesized DLC films with a KrF excimer laser (248 nm, 30 ns FWHM) at a relatively low peak intensity of 1.4 x 10^8 W/cm^2. Depositions at or below room temperatures produced hydrogen-free, transparent DLC films with an extinction coefficient of less than 0.4 at 300 nm wavelength. Electron energy loss

spectroscopy (EELS) revealed that the sp^3 bonding fraction was on the order of 70% - 85%. The film electrical resistivity was measured at room temperature to increase from 10^2 to 10^8 Ω-cm, as a function of increasing laser intensity. These improved film properties were attributed to the energetic nature of the laser plasma, because the carbon ion kinetic energy was also observed to have increased as a function of increasing laser intensity. The use of an auxiliary plasma enhancement modification, similar to that employed by Krishnaswamy [52], was found to have yielded slightly inferior DLC films to those made with laser plasma alone.

In the experiment carried out by Xiong et al. [57], an ArF excimer laser (193 nm, 21 ns FWHM) was used to deposit hydrogen-free DLC films at a peak laser intensity of 5 x 10^8 W/cm^2. At room temperature, the DLC films were measured to have a mechanical hardness up to 4000 kg/mm^2 and a maximum optical bandgap of 2.6 eV. The highest sp^3 bond fraction was estimated through EELS measurement to be 95%. This result is believed to be the highest tetrahedral bonding percentage ever measured on a diamond-like carbon thin film, hydro- or unhydrogenated. The films were also found to have good thermal stability up to 800 °C, where the optical bandgap showed only a slightly lower value than that measured at room temperature. This also marked the first time a thermally stable DLC film was claimed to have been made, by any type of deposition techniques. Though no film electrical resistivity measurement was conducted in conjunction to further verify this result, the authors nonetheless made two interesting observations through their experiments:

1. High intensity laser induced laser plasma alone was sufficient to produce high quality DLC films, without any need for an auxiliary plasma enhancement system;

2. Laser beam with shorter wavelength in the UV range, in contrast to those in the IR range, appeared to have produced DLC films with superior qualities. The reason was attributed to a change in the optical penetration depth which decreases with shorter wavelength. Higher photon energy associated with shorter laser wavelength leads to a

more efficient coupling of the laser energy to the target, resulting in the production of atomic ion species and an increase of their kinetic energy. The authors speculated that atomic C^+ ions with a mean kinetic energy of 50 eV and over were present in the laser plasma.

Film deposition by sub-nanosecond lasers. The phenomena associated with the use of ultrashort, intense laser beams have been of interest in the high field physics community for well over a decade. High-harmonic generation, high-brightness, short pulse X-rays formation, wakefield acceleration, and possible thermonuclear fusion reactions are among the research subjects [58]. The use of ultrashort pulsed lasers in the deposition of thin film materials, however, remains an uncharted territory. Researchers are only beginning to explore the potential applications this unique technique might bring to the materials science related areas, such as medical-surgical procedure, micromachining, as well as thin film material processing [59-61].

We are aware of only one other research group that has conducted some preliminary experiments on the femtosecond laser deposition of thin film materials [62]. In their experiment a KrF excimer laser, with a 30 ns temporal duration (FWHM) at 248 nm wavelength, was compressed to deliver 500 femtosecond (FWHM) pulses. Depositions of DLC, silicon and copper thin films were carried out using both the 30 ns and 500 fs pulses, at laser intensities of 2.3×10^8 and 1.4×10^{13} W/cm^2, respectively. For the femtosecond laser pulses, the particle kinetic energy, mass distribution and optical emission spectra were found to be significantly different from the respective nanosecond results. While only atomic carbon ions were detected in the 500 femtosecond pulse induced plasma, cluster formation was found in the time-of-flight (TOF) spectra during the 30 ns laser ablation. This observation suggested a higher degree of target species atomization (existence of atoms or singly charged ions instead of molecular clusters in the plasma) with the use of shorter laser pulses. Both DLC and Si films showed improved qualities by using the femtosecond laser pulses, due to the fact that higher kinetic energies

(in the keV range) were obtained in the femtosecond laser induced plasma, without the formation of large particulates. The authors also suggested that there may exist a threshold laser intensity somewhere between 10^9 and 10^{13} W/cm^2, below which molecular carbon particles were favored and above which atomic carbon ions would be dominant.

Table 2 summarizes the properties of hydrogen-free DLC films deposited by various laser deposition techniques.

Table 2. Properties of DLC films deposited by laser beam.

Laser	λ(nm)	Intensity (W/cm^2)	sp^3 %*	n**	k**	Eg* (eV)	Resistivity (Ω-cm)*	Reference
CO_2	10600	$5x10^3$	0	-	-	0	0	44, 45
Nd:YAG	1064	$3-13x10^{10}$	-	-	-	0.4	-	46
Nd:YAG	1064	$5x10^{11}$	75	2.35	0.21	1.0	$>10^7$	49
Ruby	694	$6.7x10^8$	-	2.55	0.07	1.25	10^7	14
XeCl	308	$3x10^8$	-	2.2	0.04	1.4	-	48
XeCl***	308	$1.25x10^8$	-	2.4	0.14	1.27	-	52
XeCl	308	$1.25x10^8$	-	2.7	0.85	0.47	-	52
XeCl	308	$8x10^9$	-	2.5	0.12	2.2	$>10^4$	56
KrF***	248	$1.4x10^8$	15-27	2.53	0.14	1.5	$>10^6$	50
KrF	248	$1.4x10^8$	68	2.55	0.04	1.7	$>10^6$	50
KrF	248	$8x10^8$	77	-	-	2.2	-	29
ArF	193	$5x10^8$	95	2.56	0.02	2.6	-	57

* measured at room temperature

** measured at 632 nm wavelength

*** with plasma enhancement modification

There are tremendous amount of information available on the subject of DLC film fabrication using various laser deposition techniques. Though there still lacks a universally accepted description of the DLC formation mechanism, many research groups have reached the conclusions that:

1. Pulsed laser deposition is likely an ion assisted energetic condensation process;

2. The resultant DLC film quality is largely a function of the carbon particle kinetic energy and the subsequent energy dissipation mechanism;

3. Higher laser intensity usually gives rise to a more energized plasma, resulting in DLC films being more diamond-like.

In comparison, knowledge of the laser induced plasma, particularly its dynamic transport between the target surface and the substrate, which ultimately determines the resultant film quality, appears to be relatively scarce. The inadequacy in understanding the laser plume dynamics is partly due to the difficulties involved in analyzing the highly transient laser-plasma interaction processes, and partly because of the phenomenological approach often taken by the materials science community with respect to laser deposition of thin film materials.

Pappas et al. [63] have studied the vapor plume generated by a KrF excimer laser irradiation of a graphite target, at a peak laser intensity of 1×10^8 W/cm^2. This intensity resembled the conditions under which actual DLC films were produced. Laser induced fluorescence (LIF) and a Langmuir probe were used, respectively, to characterize carbon molecules and ions present in the plasma. They learned that both neutrals (in the form of a variety of small clusters) and ions were abundant in the laser plume, and the ions had significantly higher kinetic energies than the neutrals. The kinetic energy of both ions and neutrals increased as a function of increasing laser fluence (in units of J/cm^2), along with that of the electron temperature. At a 70° laser incident angle, the most probable kinetic energies for the C_2 molecules were measured to be ~ 12 eV, and up to 80 eV/atom for the C_n^+ ions. The ions were not mass resolved in their experiment, the authors thereby

assumed that all ions were singly charged. Laser ionization mass analysis (LIMA) using 266 nm radiation at similar laser intensity level revealed that the mass spectrum consisted almost entirely of C_n^+ ions, with n varies from 1 to 12. Most of the yield was weighted toward the lower n values. At a distance of 10 cm from the target surface, an ion fraction of 5 - 10% was estimated. The authors conclude that the films become more diamond-like as the laser intensity is increased, indicating that higher kinetic energy of the depositing particles is a critical factor in obtaining high quality DLC films. This observation seemed to have confirmed the energy-barrier model proposed by the same group in an earlier report [64]. In that study, the researchers suggested that conversion of the low density, low energy sp^2 graphite geometry to the higher density, metastable sp^3 geometry can be envisioned on a potential-average atomic distance diagram. On this diagram, the sp^2 and sp^3 bonding arrangement can be viewed as two minima which are the product of multiple atomic interactions that occur as the particles are incorporated onto the surface. Between them is the so-called potential barrier, which represents the energy required for the film structure to change from one configuration to the other. When deposition techniques such as thermal or electron beam evaporation is employed, carbons with thermal energy mostly less than1 eV (1eV = 1.16 x 10^4 K) are generated. They will subsequently condense into the thermodynamically stable sp^2 structure. In contrast, carbon particles generated by IBD or PLD techniques have much higher kinetic energies (generally between tens and hundreds of electronvolts). The impact of these highly energetic particles will force the initially sp^2 bonded carbon atoms to overcome the energy barrier into the metastable sp^3 configuration. Furthermore, the excessive energies carried by these particles, if not promptly quenched by the substrate, may again drive a sp^3 bonded atom back over the barrier to the equilibrium sp^2 structure. This qualitative study is in essence a prototype of the energetic ion bombardment/thermal quench model later proposed by Robertson [36].

Germain et al. [65] studied the plasma created during the interactions between a graphite target and a KrF laser beam (248 nm, 15 ns FWHM). Time and spatially-

resolved spectroscopy were collected at a distance of less than 2 mm away from the target, to detect the carbon particle charge state as well as its expansion velocity. At a vacuum pressure of 5×10^{-5} Torr and a laser fluence of less than 7 J/cm^2, the laser plume was found to contain mostly C_2 molecules (atomic C signal was lost in the background noise). These carbon neutrals had an expansion velocity of 9.4×10^5 cm/s, corresponding to a kinetic energy E of 11 eV. C^+ and C^{2+} ions, along with larger carbon clusters (charge state unresolved) became abundant at higher laser fluences. Their expansion velocities were determined to be in the $2 - 9 \times 10^6$ cm/s range (E = 25 - 500 eV), increasing as a function of laser fluence. The authors also reported the possible existence of carbon ions with even higher charge states. Good DLC film/substrate adhesion was achieved at room temperature with high laser fluences.

A more comprehensive investigation on the dynamics of laser-graphite interactions was later conducted by Murray and Peeler [66]. Through time-of-flight (TOF) experiments, they measured the kinetic energy of the carbon particles ablated from a graphite target with different laser beams. They used a Nd:YAG laser (15 ns FWHM) at the fundamental 1064 nm and frequency-doubled 532 nm wavelength, in addition to an excimer laser system (15 ns FWHM) running at 248 nm and 193 nm wavelength. Their results indicated that ablation of graphite with the 1064 nm radiation produced a series of low energy (E < 5 eV) clustered carbon C_n^+ ions (1 < n < 30). Irradiation of graphite with 532 nm and 248 nm laser beams resulted in the ejection of molecular carbon ions (C_2^+, C_3^+), which have kinetic energies between 20 and 60 eV. Also, ablation by the 193 nm laser beam generated mostly atomic C^+ ions with a mean kinetic energy of 600 eV. The DLC films deposited at various wavelengths were analyzed by electron energy loss spectroscopy (EELS). The authors found that large, low energy carbon clusters tended to induce the sp^2 graphitic film structure, while highly energetic, atomic carbon ions encouraged the formation of sp^3 bonded diamond-like films. The strong correlation between the film quality and the particle kinetic energy/laser wavelength supports

Cuomo's model [64] and the work by Xiong [57]. Table 3 tabulates the results from Murray's experiment [66].

Table 3. Kinetic energy of carbon particles as a function of laser wavelength [66].

Wavelength (nm)	Laser Intensity (W/cm^2)	Predominant Ions	Mean Kinetic Energy (eV)
1064	1.8×10^8	C_{11}^+	3.3
		C_{15}^+	4.5
532	1.8×10^8	C_2^+	38
		C_3^+	17
248	2×10^8	C_2^+	55
		C_3^+	18
193	2×10^8	C^+	600

In a related experiment, using a KrF excimer laser at a laser intensity of 2×10^8 W/cm^2, Peeler and Murray [67] compared DLC films made with and without charged carbon particles in the plume. Filtration of the carbon ions was achieved through the use of ion deflectors mounted in the path of the laser plume. DLC films made with neutral particles only and with both ions and neutrals were studied by valence/core level EELS. All the films were found to have similar sp^3 fractions at around 85%. Though the authors supported the notion that the formation of DLC film by PLD is likely an energetic condensation process, they questioned whether it is also an ion assisted process. A study by Diaz's group [68] seemed to endorse Peeler's argument. Using a frequency-doubled Nd:YAG laser beam (532 nm) at laser intensities in the 10^{10} W/cm^2 range, they produced DLC films with and without ionized carbons in the plume. Ions were filtered from the plume by imposing a strong magnetic field (up to 8 kGauss) in the plasma path. Raman

spectroscopy and thickness measurement were carried out on two films deposited under otherwise identical conditions, except the inclusion of ions for one sample. From the thickness difference between these two DLC films (800 Å with ions, and 700 Å without), a plasma ion fraction of ~12% was estimated. Obvious similarity between the two Raman spectra prompted the authors to conclude that the carbon atom electronic hybridizations are essentially the same for the two DLC films. The authors also conducted TOF experiments with a Faraday ion collector. They discovered that around 50% of the ejected ions were singly charged monomers (C^+), with the rest being clustered ions up to hexamers and hepamers. However, some of the authors' claims warrant a more careful look. It has been noticed by various other researchers that the Raman spectra of DLC films with vastly different sp^3/sp^2 ratios can exhibit rather similar features (explained in Chapter 4). Therefore without any other measurement of the film properties, such as their electrical resistivity or mechanical hardness, it would only be plausible at best to assert that ions are not a factor in affecting the DLC film formation.

In summary, along with ion beam depositions (IBD), pulsed laser deposition (PLD) has established itself as one of the premium techniques in producing high quality, hydrogen-free DLC films. The formation of diamond-like, tetrahedral sp^3 bonds is believed to be enhanced by the energetic plasma generated with high intensity laser beams. With accommodating substrate conditions such as low temperature, sufficient thermal quenching ability, DLC films with high hardness, high electrical resistivity, and a relatively large optical bandgap can be condensed from small carbon particles with high kinetic energies. The optimum kinetic energy, depending on the predominant species present in the laser induced plume, is projected to be between several tens to several hundreds of electronvolts. Higher laser intensity usually leads to the creation of carbon particles with higher kinetic energies, and in most cases, better film qualities. But the advantage gained from a more energized plasma is sometimes compromised by the addition of larger, clustered carbon particles found at high laser intensities. Also, due to the nature of the

laser beam profile and the beam-solid interactions, a wide spread of the particle energy distribution is often inevitable. This may also contribute to particulate formation on the film surface from those particles that do not have sufficient energy to break up upon impact. Though pulsed laser deposition of DLC film may be adequately described as an energetic condensation process, whether it is also an ion assisted one remains somewhat controversial. Moreover, there seems to exist a strong correlation between the film quality and laser wavelength, at least for laser beams with nanosecond pulsewidth. Lasers with shorter wavelengths in the UV range appeared to have produced more atomized carbon species with higher energies, leading to films with better qualities. This is in contrast to those lasers with wavelengths in the IR or near IR range, which seemed to generate larger, less energetic carbon clusters. It thus requires higher intensities for long wavelength lasers than short UV lasers to achieve similar plasma characteristics, otherwise the resultant films tend to be more graphitic. This can be contributed to the fact that absorption coefficients would increase as one moves to shorter wavelength, and the penetration depth into the target material is correspondingly reduced. It is a favorable situation as the laser energy is now consumed by thinner layers of the target, thereby the thermal coupling between laser and solid will be more efficient. The stronger absorption at shorter wavelengths is also believed to reduce the ablation density threshold. In consideration of this intriguing but not yet well resolved phenomenon, a high "effective" laser density, or volume laser intensity expressed in W/cm^3, seems to be more appropriate than the planar laser power density (W/cm^2) in describing the deposition parameter that favors the sp^3 bond formation.

It should also be noted that little information is available at the present time, on the subject of sub-nanosecond, high intensity laser deposition of DLC films. Nonetheless, early evidence suggested that at very high intensities, the laser induced plasmas are likely to have a higher degree of ionization and atomization, accompanied by high ion kinetic energies up to the keV range. These are essentially the same ingredients that have proven

to produce high quality DLC films for nanosecond laser pulses.

Laser-Solid-Plasma Interactions

The success of PLD technique in making DLC films is determined by the physical processes associated with the laser-target-plasma interactions.

Common features in the PLD technique include a laser generated plasma near the target surface and the subsequent hydrodynamic expansion of the plasma in vacuum. This high temperature, high pressure plasma contains different target carbon species, which move toward the substrate with high speed in a strong forward-directed fashion. The quality of the resultant DLC films is therefore a function of the energetic condensation of these particles upon reaching the substrates.

When considered in the time domain, the PLD process can generally be divided into three phases:

1. Interactions of the laser beam with the target material, resulting in heating/melting vaporization of its surface layers;

2. Interactions of the evaporated target species with the incident laser beam, giving rise to plasma heating and absorption;

3. Hydrodynamic plasma expansion in vacuum, leading to the characteristic nature of the PLD process.

For simplicity, the first two phases are often considered to start with the onset of the laser pulse and continue through the laser pulse duration, while the third phase commences after the pulse terminates. In actuality, however, these phases are often not separable due to substantial overlap amongst them. Since our investigation involves the use of a Nd:YAG and a Ti:Sapphire laser system, the following discussion of the laser-solid-plasma interactions will be limited to those generated by a single pulse of these nano- and femtosecond lasers.

Many thermo-physical phenomena associated with the beam-solid-plasma interactions are shared by these two types of laser pulses. However, due to each one's unique pulse duration and thus different attainable laser intensity levels, certain aspects of these three regimes could have distinctively different attributes.

The ensuing sections first address certain aspects of the laser-solid-plasma interactions, including a brief discussion of the plasma hydrodynamic model used to describe the evolution of plasma expansion. This will be followed by several examples of studies having dealt with the plasma generation and expansion induced by these two classes of lasers, in the intensity regimes that are relevant to DLC film depositions. Emphasis is given to those instances where measurements (or simulations) of carbon ion charge/kinetic energy distribution have been carried out as a function of laser intensity.

With a typical single pulse output, the laser-target-plasma interactions can be summarized as follows:

At the onset of laser pulse incident on the surface, the target electrons immediately absorb incident laser radiation and a thermal equilibrium state is reached amongst themselves within several femtoseconds ($\sim 10^{-14}$ s). These electrons then start to couple their energy to the lattice atoms, through electron-atom collisions. The lattice temperature is expected to rise and become the same as that of the electrons within about one picosecond ($\sim 10^{-12}$ s) [69]. As the surface layer is further heated, it will eventually melt and vaporize, creating a collections of electrons, ions, neutrals, as well as Rydberg state atoms in front of the target surface. In another word, a plasma is generated. There is no absolute definition of a plasma, but it can best be interpreted as a physical state of matter with high electrical conductivity and largely gaseous mechanical properties.

The initial plasma temperature and charge density, represented by those of the electrons, are relatively low. The plasma is thereby transparent to the incident laser beam. Electron-neutral inverse bremsstrahlung dictates the absorption of laser energy and the plasma temperature will rise rapidly as a function of time. As the plasma becomes more

ionized the electron-ion inverse bremsstrahlung takes over as the main absorption mechanism. Saha equations can then be used to predict the plasma ionization ratio. At sufficiently high temperatures (10000 °C or higher), a fully ionized plasma will develop. Here "fully ionized" refers to ions in the plasma with different charge states and not necessarily fully stripped ions.

With successively higher electron and ion densities, this hot plasma progresses to become more absorbing to the laser light, thus preventing the trailing laser pulse from reaching the solid target. In fact, depending on the laser wavelength and its intensity, the incident laser beam could be totally reflected at the so-called "critical surface", before the peak of the laser pulse arrives. This critical surface is defined as the plasma layer where the electron density reaches a threshold. The critical electron density n_c can be calculated, in cgs units, from the equation that describes a uniform, collision-less plasma with an unperturbed electron density:

$$\omega = \omega_p = (4\pi e^2 n_c / m_e)^{0.5} \tag{2-1}$$

where m_e is the electron mass, e the electron charge, ω the laser frequency, and ω_p the plasma frequency. For a frequency-doubled Nd:YAG laser of 532 nm wavelength, $\omega = 3.54 \times 10^{15}$ s^{-1}, and $n_c = 3.9 \times 10^{21}$/cm^3. For a Ti:Sapphire pulse of 780 nm wavelength, $\omega = 2.41 \times 10^{15}$ s^{-1} and $n_c = 1.8 \times 10^{21}$/cm^3. At the critical surface, the magnitude of the complex plasma index of refraction decreases from nearly one to zero, yielding a reflectivity of one.

Absorption of the laser energy in the plasma is a nonlinear process. It increases as square of the electron density and cube of the ion charge state. The high electron temperature generated by this inverse bremsstrahlung induces large thermal pressure gradients within the plasma. These steep thermal gradients will lead to a rapid expansion, or "blow-off" of the plasma in the direction largely perpendicular to the target surface, thus converting plasma thermal energy into expansion energy of the electrons and ions.

Since an electron has negligible mass compared to that of an ion, all the expansion energy can be considered to have been converted into ion kinetic energies. As a result of this expansion, the plasma density will quickly drop below the critical density. If this happens before the laser pulse terminates, any remaining laser pulse will again be able to reach the target surface. Further heating of the target is also provided through radiation loss from the plasma and via heat conduction in the solid. The ablated target species in the expanding plasma will recombine and cool, through radiative and three-body recombination processes. The degree of recombination and cooling depends on initial plasma conditions and background pressure. At pressures lower than about 10^{-4} Torr, any recombination between the plasma particles and ambient molecules can be considered negligible.

The phenomena discussed above are a series of dynamic processes. A successful modeling of these processes is difficult. This is because a plasma usually contains a large number of charged particles and each one of them generates its own electromagnetic field. The motion of each particle is in turn modified by this field. To fully describe the state of a plasma, each particle would require six equations to calculate its motion (position/velocity) and associated electromagnetic field. This makes a complete dynamic description of the above sequence of events practically impossible.

Historically, studies of laser induced plasma have instead treated it as a fluid: the individual motion equation of charged particles is averaged to give a distribution function of the plasma. This phase space distribution function $f(x, u, t)$, which gives the plasma density at spatial position x and time t with velocities between u and $u + \delta u$, can therefore characterize the plasma as a fluid and its collective behavior.

When dealing with a carbon plasma, a two-fluid model, one for the electrons and one for the carbon ions, is usually considered adequate. By coupling the two-fluid model equations with the Maxwell's equations, a complete description of the carbon plasma evolution can be obtained, for given initial conditions.

The Maxwell's equations relate the electric and magnetic fields to the charge and current density of the plasma, in cgs units:

$$\nabla \cdot E = 4\pi\rho \tag{2-2}$$

$$\nabla \cdot B = 0 \tag{2-3}$$

$$\nabla \times E = -\frac{1}{c}\frac{\partial B}{\partial t} \tag{2-4}$$

$$\nabla \times B = \frac{4\pi}{c}J + \frac{1}{c}\frac{\partial E}{\partial t} \tag{2-5}$$

where E and B are the electric and magnetic fields, respectively, $\rho = \sum nq$ (n is the plasma density, q the particle charge) is the plasma charge density, $J = \sum nqu$ (u is the mean fluid velocity) is the plasma current density, and c is the light velocity.

The logarithm defining the plasma as a fluid includes three basic equations. They are derived by taking moments with respect to velocity of the Vlasov equation. These include the Euler's equation of motion (conservation of momentum), the equation of continuity (conservation of mass), and the equation of state (isothermal or adiabatic compressibility) [70]:

$$n(\frac{\partial u}{\partial t} + u\frac{\partial u}{\partial x}) = \frac{nq}{m}(E + \frac{u \times B}{c}) - \frac{1}{m}\frac{\partial p}{\partial x} \tag{2-6}$$

$$\frac{\partial n}{\partial t} + \frac{\partial}{\partial x} \cdot (nu) = 0 \tag{2-7}$$

$$p = n\theta \qquad \text{[isothermal]} \tag{2-8}$$

$$\frac{p}{n^\gamma} = cons\tan t \qquad \text{[adiabatic]} \tag{2-9}$$

here m is the particle mass, p is the plasma thermal pressure and u is the fluid velocity. The plasma pressure p is related to its density by equation of state (2-8) or (2-9), depending on the condition of the charged fluid under consideration. The isothermal

equation (2-8) applies when $\omega/k \ll v$, where ω and k are the characteristic frequency and wavenumber (cm^{-1}) of the process being considered, and v is the particle thermal velocity. In this case, $p = n\theta$, where temperature θ is a constant. This condition is generally assumed during the laser pulse span, when heat flow is so fast that the temperature of the charged fluid remains constant. On the other hand, when $\omega/k \gg v$, the adiabatic equation (2-9) applies. An adiabatic process occurs when the fluid has no exchange of heat or energy with other medium outside. The plasma expansion after the laser pulse termination is usually considered to satisfy the adiabatic condition. The plasma pressure is then related to its density through equation (2-9), where $\upsilon_i = 1/\tau$ is the effective electron-ion collision frequency (τ is the mean collision time), $\gamma = c_p/c_v = (F + 2)/F$, with c_p/c_v being the ratio of specific heat, and F being the number of degrees of freedom. For a fully ionized plasma F = 3, which corresponds to a γ vaule of 5/3.

The simulation of a spherical laser plasma expanding into a vacuum typically relies on self-similarity solutions to the hydrodynamic equations considered above. Self-similarity flow is defined as one for which the expansion scale-lengths, therefore the density profiles, are considered to be independent of time. The expansion velocity profile is regarded as linear, increasing with distance from laser focus to the plasma front edge. Also, the plasma is treated in both the spatial and time domains as if it were originated from a point source. Fader [71] has carried out a complete hydrodynamic calculation of a spherical plasma expanding into vacuum. He demonstrated that some time after the plasma ignition, its radial velocity profile v (r, t > 0) always becomes linear, the ion density n (r, t > 0) invariably assumes a Gaussian profile, and its temperature drops adiabatically. This was found to be true regardless of their respective initial conditions. The fact that the plasma density and velocity remain similar in the time limit $\tau \ll t < \infty$ (τ being the laser pulse duration) is the reason for using self-similar solutions to describe the plasma expansion.

When solving the hydrodynamic equations of the proceeding sections, the laser energy transfer to the plasma is usually assumed to be fully symmetric. The energy transfer and equilibration time is considered to be instantaneous when compared to the laser pulse duration. These assumptions are justified when the laser intensity is not exceedingly high or the pulse extremely short. Potential modeling inadequacies associated with the use of ultrashort femtosecond laser beams will be addressed later in this chapter.

Nanosecond Laser Plasma

For nanosecond laser-solid interactions, Singh [72] has developed a model to describe the thermo-physical phenomena associated with the plasma expansion. This model treated the laser instigated plasma as a high-temperature, high-pressure gaseous phase that is initially confined to small dimensions and then allowed to expand freely in vacuum. Gas dynamic equations were set up to simulate expansion velocity of the plasma.

With intensity level in the 10^9 - 10^{11} W/cm^2 range considered for a nanosecond Nd:YAG laser pulse, initiation of the beam-solid interactions is believed to be largely a thermionic emission process. Removal of the target material by laser irradiation depends on beam-solid coupling, which leads to melting and/or vaporization of the surface layers. Energy dissipation is carried out exclusively through conduction in the solid. Radial transport can be neglected as long as the laser beam is relatively well focused. Properties of the target material, such as its optical reflectivity, absorption coefficient, thermal conductivity and specific heat are the principal parameters defining this process. The evaporation attributes as a function of laser and material parameters can be modeled with the solution of a one-dimensional heat flow equation, constrained with appropriate boundary conditions. The energy deposited onto the target, by simple heat balance consideration, should be equal to the energy needed to vaporize the surface layers plus the conduction loss by the substrate and the absorption by the plasma. This yields:

$$\Delta d = (1 - R)(E - E_{th})/(\Delta H - C_v\Delta T) \qquad (2\text{-}10)$$

where Δd, R, ΔH, C_v, ΔT, and E are the evaporated surface thickness, reflectivity, latent heat, volume heat capacity, temperature rise, and laser energy density (J/cm^2), respectively. E_{th} represents the energy density threshold above which evaporation is observed. Nonlinear changes in Δd may be observed due to self-induced variations of the coupling parameters used in the above equation.

After the surface layers reach the melting point or sublimation temperature, a transient plasma is generated above the target, while the liquid-solid interface penetrates into the bulk. The plasma absorption coefficient α (cm^{-1}) can be expressed as [73]:

$$\alpha = (3.69 \times 10^8)(Z^3N^2/T^{0.5}\nu^3)[1 - \exp(-h\nu/kT)] \qquad (2\text{-}11)$$

where Z, N, T, ν, h, and k are the average ion charge, plasma density, plasma temperature, laser frequency, Planck constant and Boltzmann constant, respectively. This equation predicts stronger plasma absorption at longer laser wavelength. Numerically, it would require a relatively high plasma density on the order of 10^{19}/cm^3 or higher for a significant absorption to occur. At laser intensities considered in our experiment, this density level should be easily achieved. The $1 - \exp(-h\nu/kT)$ term represents the loss due to stimulated emission.

Based on the above discussion, a schematic of the laser-solid-plasma interactions can be shown in Figure 2-3 (dimensions not drawn to scale). When considered in the spatial domain, three separate regimes can be distinguished:

I. Unaffected bulk material;

II. Melting/evaporating target surface;

III. Laser induced plasma, which is highly absorbing at near the target surface and becomes transparent at the fast expanding edge.
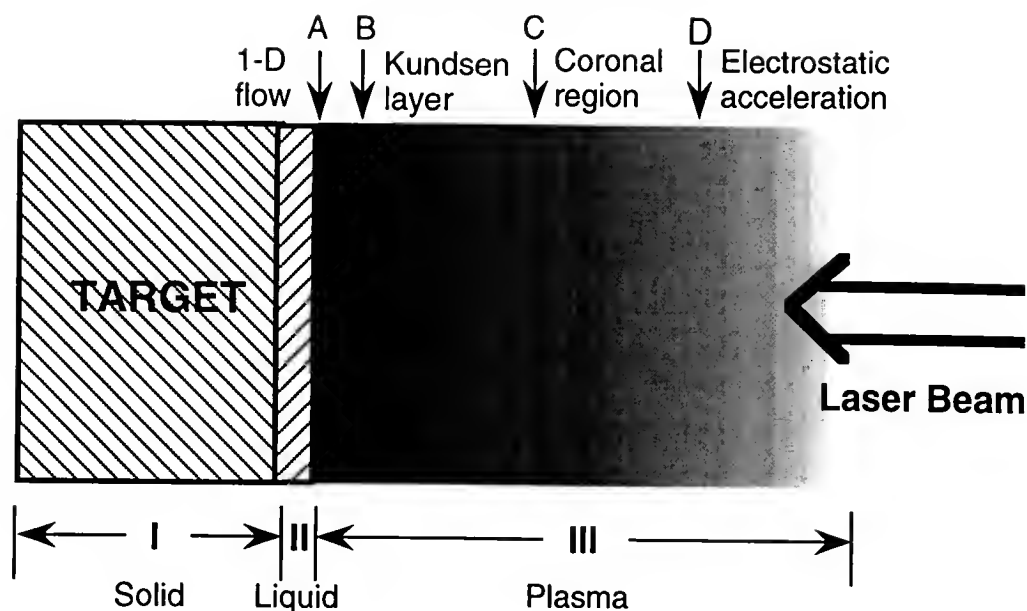
Fig. 2-3 Schematic of laser-solid-plasma interactions.

The laser plasma region III itself consists of several overlapping sub-regions marked as A, B, C, and D in Figure 2-3. Region A, whose dimension is much smaller than the laser focal spot, is generally treated as a highly absorbing, one-dimensional steady state fluid. Depending on laser intensity and wavelength, this layer could become reflective to the incident beam if its electron density exceeds that of the critical density. Region B is the so-called Knudsen layer resulting from the three-dimensional expansion of layer A. It is a highly collisional regime with an explicit center-of-mass velocity, leading to a beam-like plasma expansion [74]. This regime also sees a reduced plasma temperature and density. Further plasma expansion into Region C yields the coronal region where collisions among electrons and ions become less frequent. The hot electrons created in the previous regions could then decouple from the Boltzman-Maxwellian distribution and deviate from local thermal equilibrium (LTE). A small number of these electrons may actually escape from the main plasma, due to the lack of energy-exchanging collisions. In Region D, these escaped electrons can create a high electrical field which is much higher

than that represented by the plasma temperature kT_e. This electrostatic field in turn accelerates ions in the plume to high kinetic energies. In fact, due to even lower electron-ion collision frequencies in this region, the electrons and ions may form an oscillating cloud while they continue to expand in vacuum, during which process the ions can acquire successively higher energies. These ions will reach an asymptotic energy distribution when all the electron energies have been captured. Keep in mind that when a nanosecond laser pulse is considered, only Regions A and B may have sufficient time to form during the span of the laser pulse, while Regions C and D are not likely to develope well after the pulse has terminated.

During the laser pulse span, it is often assumed that the energy absorbed by the plasma is distributed uniformly over its entire mass. This assumption is validated by the fact that the plasma thermalization time (on the order of one picosecond) is much less than the time it takes the plasma to expand to any significant dimensions. Consequently, a uniform temperature in the plasma can be established. The plasma in this regime is therefore at an isothermal state. It will continuously absorb laser radiation and expand outward.

Rapid expansion of the plasma in vacuum results from large thermal pressure gradients. This isothermally expanding plasma can be treated as a high-temperature, high-pressure ideal gas. By applying gas dynamics, the expansion can be simulated by its density, pressure, and velocity profiles as shown in Figure 2-4 [72].

The plasma density can be expressed as a Gaussian function for $t \leq \tau$, τ being the laser pulse duration:

$$n(x,y,z,t) = \frac{N_t t}{\sqrt{2}\pi^{1.5}\tau X(t)Y(t)Z(t)} \exp(-\frac{x^2}{2X(t)^2} - \frac{y^2}{2Y(t)^2} - \frac{z^2}{2Z(t)^2}) \qquad [t \leq \tau]$$

$$(2-12)$$

here $n(x,y,z,t)$ is the plasma density at any point and time, N_t is the total number of plasma particles at the end of the laser pulse ($t = \tau$), and $X(t)$, $Y(t)$, $Z(t)$ are dimensions of the

plasma in three orthogonal directions and correspond to distance at which point the plasma density is 60 - 65% of its maximum value. Since the plasma is being treated as an ideal gas, the plasma temperature at any point is then related to its density by:

$$P = n(x,y,z,t)kT_0 \qquad [t \leq \tau] \tag{2-13}$$

where T_0 is the isothermal temperature of the plasma.

Dawson [75] has argued that in order to maintain a Gaussian density profile, the plasma expanding velocity needs to be proportional to the distance from the target surface. A self-similarity expression for the spatial and temporal dependence of the velocity can be expressed as:

$$v(x,y,z,t) = \frac{x}{X(t)}\frac{dX}{dt}i + \frac{y}{Y(t)}\frac{dY}{dt}j + \frac{z}{Z(t)}\frac{dZ}{dt}k \qquad [t \leq \tau] \tag{2-14}$$
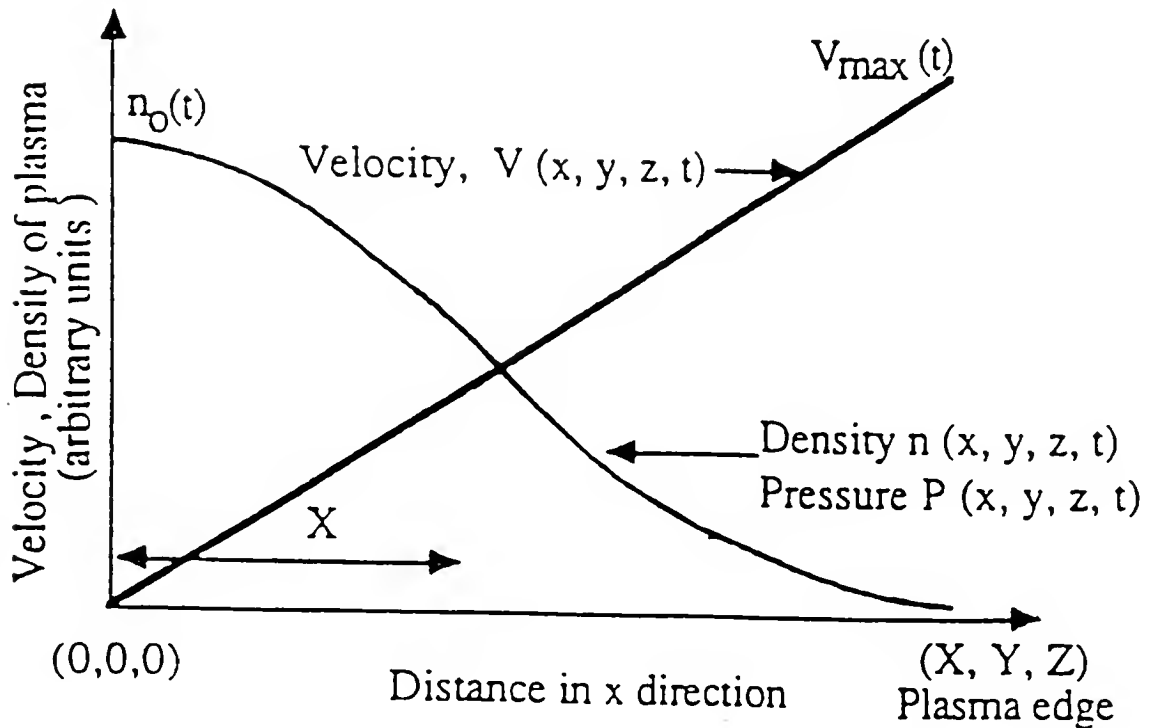

Fig. 2-4 Schematic profile of plasma density, pressure, and velocity gradients perpendicular to the target surface [72].

where dX/dt, dY/dt, and dZ/dt are plasma expansion velocities at positions X, Y and Z, respectively. This equation manifests that the inner edge of the plasma contains a maximum of density and a minimum of velocity.

Since the equation of gas dynamics governing the expansion of plasma is essentially the equation of continuity and motion, a solution for the plasma expansion can be computed by substituting the expression for density, velocity and pressure into the continuity and momentum equations discussed in the earlier sections. This yields:

$$X(t)[\frac{1}{t}\frac{dX}{dt}+\frac{d^2X}{dt^2}]=Y(t)[\frac{1}{t}\frac{dY}{dt}+\frac{d^2Y}{dt^2}]=Z(t)[\frac{1}{t}\frac{dZ}{dt}+\frac{d^2Z}{dt^2}]=\frac{kT_0}{M} \qquad [t \leq \tau]$$

(2-15)

The above equation determines the expansion of the three orthogonal plasma edges, with the initial plasma dimensions on the order of tens to hundreds of microns in the transverse direction and less than one micron in the direction normal to the target surface. It also suggests that the plasma has a low velocity and high acceleration at the initial expansion stages. But as velocity increases, acceleration will start to diminish and eventually drop to zero, giving rise to an elongated plasma shape.

Since no laser-plasma interaction exists after the laser pulse terminates, an adiabatic plasma expansion will take place, where the plasma temperature is related to its dimension by the adiabatic thermodynamic equation:

$$T[X(t), Y(t), Z(t)]^{\gamma-1} = Constant \qquad [t > \tau] \qquad (2\text{-}16)$$

where $\gamma = c_p/c_v$ is the ratio of specific heat capacities at constant pressure and volume. The thermal energy is then rapidly converted into ion kinetic energy with the fast expanding plasma. Depending on the value of γ, the maximum attainable expansion velocity is usually several times that of sound. In the adiabatic regime, the plasma density, pressure, and velocity can be expressed similarly as those in the previous isothermal regime by neglecting the t/τ term which takes into account the injection of particles into

the plasma. In addition, a solution that controls the plasma expansion can be obtained by substitution of density, pressure, and velocity into the differential equations of energy and temperature in the adiabatic regime. This yields:

$$X(t)[\frac{d^2 X}{dt^2}] = Y(t)[\frac{d^2 Y}{dt^2}] = Z(t)[\frac{d^2 Z}{dt^2}] = \frac{kT_0}{M}[\frac{X_0 Y_0 Z_0}{X(t)Y(t)Z(t)}]^{\gamma-1} \qquad [t > \tau]$$

(2-17)

where X_0, Y_0, and Z_0 denote the initial orthogonal dimensions of the plasma after pulse termination. This equation indicates that acceleration of the plasma depends on its temperature and dimension, as well as the mass of the ablated species.

The initial transverse Y and Z dimensions are much larger than the perpendicular X dimension, which represents the expansion length in the isothermal regime. Therefore the highest velocity is expected in the X direction as the velocity is dictated by these lengths shown in the above equation. This leads to the characteristic plasma shape elongated outward from the target surface. The above equation also implies that if the plasma is initially longer in Y than in Z direction, the plasma will be accelerated more in the latter direction. As the plasma expands, most of the thermal energy is converted into the kinetic energy, thereby no more energy is left for further expansion. The plasma becomes elongated in the shorter X direction and retains its profile until it is intercepted by the substrate.

The same approach can be applied to all species, including ions, atoms, and small molecular clusters. Since the above model is based on the equations of fluid flow, and the expansion velocity is controlled by pressure gradients in the plasma.

In addition to a theoretical model of the hydrodynamic plasma expansion as discussed above, the following sections explain by example some of the numerical descriptions of this process. The parameters used in these examples are more closely matched with those used in our investigation.

Puell [76] has developed a hydrodynamic model for the plasma generated by an intense laser beam focused on a plane, solid target. The laser light used in his modeling was a nanosecond (7 ns FWHM) ruby pulse at 694 nm wavelength. The plasma production was treated as a steady state process. Taking into account the finite focal spot size, he also divided the plasma into three separate regions:

1. Undisturbed solid target;

2. A zone extending from the target surface out to a distance of the focal spot radius R. In this so-called heating zone, a one-dimensional plasma flow was assumed;

3. A zone beyond R where a three-dimensional plasma was allowed to show a lateral spread.

By considering an energy balance between the incident laser beam and the thermal and kinetic energy transported by the plasma flow, Puell was able to quantitatively establish a relationship between the highest plasma (electron) temperature kT, the total number of particles N generated during the laser-solid interactions, and the ion kinetic energy E as a function of the incident laser intensity I. They are summarized as follows (in cgs units):

$$kT = \alpha^{-2/3}(3MCR/50)^{2/9}I^{4/9} \tag{2-18}$$

$$N = \pi R2\alpha^{-1/3}(2MCR/3)^{2/9}\int_{-\infty}^{\infty}(I/5)^{5/9}dt \tag{2-19}$$

$$E = 5Z\alpha kT = 5Z\alpha^{1/3}(3MCR/50)^{2/9}I^{4/9} \tag{2-20}$$

where M is the ion mass, k is the Boltzmann constant, R is the focal spot radius, Z is the average ion charge, $\alpha = (Z + 1)/Z$, and $C = 2.55 \times 10^{-55}$ is a constant associated with the absorption coefficient for inverse bremsstrahlung. When laser pulse other than that of Ruby is considered, $C = 2.55 \times 10^{-55} (\omega_R/\omega)^2$, where ω is the frequency of light under consideration, and $\omega_R = 2.7 \times 10^{15}$ s^{-1} is the frequency of the Ruby laser. These equations apply to the layer within a distance of R from the target surface.

Heat conduction and radiation losses in the plasma are neglected in this model. Also, there exist two pre-conditions under which the above equations are derived from. The first one being the plasma stays largely transparent to the laser beam throughout its pulse duration, i.e., the validity of the above equations holds only if the electron density stays below the critical value of $2.3 \times 10^{21}/cm^3$ for Ruby laser. The critical laser intensity associated with this electron density is calculated to be 8×10^{13} W/cm^2. The second condition is that the plasma can be treated as a stationary flow. This assumption is satisfied by the fact that the time an electron-ion pair spends within the heating zone is much smaller than the nanosecond laser pulse duration. Under this steady state model, the ion kinetic energy is postulated to be equal to the laser intensity divided by the ion flux leaving the target surface. This assumption is based on the argument that during the heating of the plasma, the absorbed energy is partitioned between thermal and kinetic energy of the particles. At distances far away from the heating zone, however, all of the energy is transformed into ion kinetic energy due to the plasma expansion.

In a subsequent experiment, Puell et al. [77] used the same ruby laser to ablate lithium deuteride (LiD) and carbon (C) targets in vacuum. The laser intensities used were between 2×10^{11} and 5×10^{12} W/cm^2. Both the electron temperature and the ion kinetic energies of these two target materials were found to increase almost linearly as a function of increasing laser intensity. The electron temperature T_e of the carbon plasma was measured to be in the 80 - 330 eV range at an angle of 7° off the target normal, and the average ion kinetic energy E varied from 2 to 13 keV.

Both T_e and E in Puell's experiment are somewhat higher than those observed by some other researchers working in the same area. These include the results from Ambartsumyan [78], Haught [79], and Demtröder [80], where the plasma temperatures were found to be not higher than a few tens of electronvolts, and ions attained asymptotic $(t \rightarrow \infty)$ velocities on the order of 10^6 - 10^7 cm/s. These velocities correspond to kinetic energies ranging from several hundred to a few thousand electronvolts.

One possible explanation to the discrepancies among these results is that in Puell's case, a higher maximum laser intensity level was used on target materials with lower atomic weights. This could lead to higher initial electron temperatures and ion kinetic energies. Another possibility lies in the adoption of a one-dimensional heating zone geometry in Puell's model, where calculations are based on the assumption that the plasma in this heating zone absorbs all the laser energy and then adiabatically expands. In reality, this plasma layer would have expanded in a three-dimensional fashion before the laser pulse terminates. For example, with an ion velocity of 1.5×10^7 cm/s, it travels in 7 ns through a distance of ~1 mm, much larger than $R \approx 50$ µm used in Puell's model. Thereby only a fraction of the total energy carried by one laser pulse is actually consumed in the heating of this plasma zone, and a lower plasma temperature should be expected. In addition, since the inverse bremsstrahlung plasma heating is proportional to the square of the electron density, a rapid plasma expansion would effectively lower the plasma density and hence its temperature. Finally, recombination and cooling effects may be responsible for the lower electron temperatures observed in these other experiments [78-80], since their data were taken at distances further away from the ablation source.

In the experiments carried out by Demtröder and Jantz [80], a ruby giant laser pulse (30 ns FWHM), similar to the one used by Puell [76] was focused onto aluminum and copper targets in vacuum to generate plasmas. By combining the time-of-flight (TOF) and retarding potential measurements, the authors were able to detect the Cu and Al ion charge state as well as their kinetic energies, as a function of laser intensities in the 10^{10} - 10^{11} W/cm^2 range. They found that the kinetic energy of the ions was proportional to their charge and about 100 times larger than their thermal energy. At a laser intensity of 3.3×10^{11} W/cm^2 and 1.7 meters away from the target, Cu^{2+} ions were determined be the predominant species in the laser induced plume. Copper ions with up to 6-fold charge state were detected in the plasma. The median kinetic energy corresponding to the peak of the TOF spectrum was calculated for Cu^+ ions to be ~ 200 eV, and close to 2000 eV

for Cu^{5+} ions. An upper limit of 11 eV was detected for the electron temperature at this intensity level. The maximum Al ion kinetic energy, defined by the onset of the TOF signal, was found to increase from 500 to 2000 eV for laser intensities ranging from 2 x 10^{10} to 2.5 x 10^{11} W/cm^2. The disparity between the large ion kinetic energy and the low thermal energy was explained with a simple model proposed by these researchers: an oscillating electric space charge field transferred electron thermal energy to radial kinetic ion energy. In their hypothesis, a fast electron leaving the plasma cloud is electrostatically attracted back and forth, each oscillation sees a fraction of its energy being transferred to the ions. At a laser intensity of 3.3 x 10^{11} W/cm^2, up to keV ion kinetic energy is achievable if the electrons oscillate at a frequency of 2 x 10^{14} s^{-1}. The final ion kinetic energy E can be expressed as:

$$E = (nZ + 1)kT \qquad (2\text{-}21)$$

where Z is the average ion charge, T is the plasma temperature (same as ion or electron temperature), and n is a constant that describes the average number of times an electron loses and regains its thermal energy.

Based on Puell's theory [76], Stevefelt and Collins [81] carried out a computer simulation of the expansion of a carbon plasma generated by a focused Nd:YAG laser beam. Their model considered the hydrodynamic plasma expansion in vacuum after the initial ignition by the intense laser beam. Ion charge states and corresponding kinetic energies at a distance up to several centimeters away from the target surface were computed. These parameters are of more interest than the initial conditions predicted by Puell's model, since they more closely resemble the conditions under which laser depositions of DLC films are actually carried out.
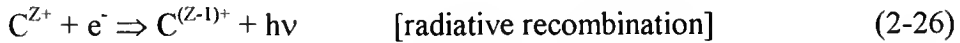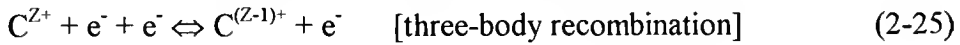
The processes included in their modeling were adiabatic cooling of the plasma, electron-ion three-body and radiative recombinations. Three hydrodynamic equations were used to describe the plasma flow:

$$\frac{d}{dr}(Nvr^2) = 0 \qquad\qquad\text{[mass density conservation]} \qquad (2\text{-}22)$$

$$\frac{d}{dr}[\frac{5}{2}(1+Z)kT + \frac{Mv^2}{2}] = \frac{Q}{v} \qquad\qquad\text{[laser energy conservation]} \qquad (2\text{-}23)$$

$$\frac{dT}{dr} - \frac{2T}{3N}\frac{dN}{dr} = \frac{2Q}{3v} \qquad\qquad\text{[first law of thermodynamics]} \qquad (2\text{-}24)$$

where r is the distance from the target surface, N the ion density, v the ion velocity, T the plasma temperature, M the ion mass, and Q the laser energy delivered to the electrons per ion per unit time. The above equations were then coupled to the recombination kinetic equations to obtain the evolution of the carbon ions with various charge states, as a function of distance from the target and laser intensity:

$$C^{Z+} + e^- + e^- \Leftrightarrow C^{(Z-1)+} + e^- \qquad\text{[three-body recombination]} \qquad (2\text{-}25)$$

$$C^{Z+} + e^- \Rightarrow C^{(Z-1)+} + h\nu \qquad\text{[radiative recombination]} \qquad (2\text{-}26)$$

Shown in Figure 2-5 and Figure 2-6, respectively, are plots adopted from the authors' paper [81]. These two figures illustrate the simulated ion concentration as a function of distance from the surface at a laser intensity of 5×10^{10} W/cm^2, and the ion fractional concentration as a function of laser intensity.

It is demonstrated in Figure 2-5 that, for a distance r larger than about 0.1 cm from the target, the relative carbon ion concentration largely remains the same. This so-called "ion freezing" phenomenon was also observed earlier by several other research groups [82,83]. In this region, three-body recombination is the dominant process, and the recombination rate β approximately scales as $\beta \propto r^{-1.5}$. The electron density decreases as a function of r^{-2}, while the ion velocity and charge assume asymptotic values. The authors also argued that because of the recombination processes, the plasma cooling should be substantially slower than a simple adiabatic expansion. Figure 2-6 shows that even at a distance of a few centimeters away from the target, multiple charged C^{4+} and C^{3+} are still the most predominant species in the plume. Using the kinetic energy equation developed
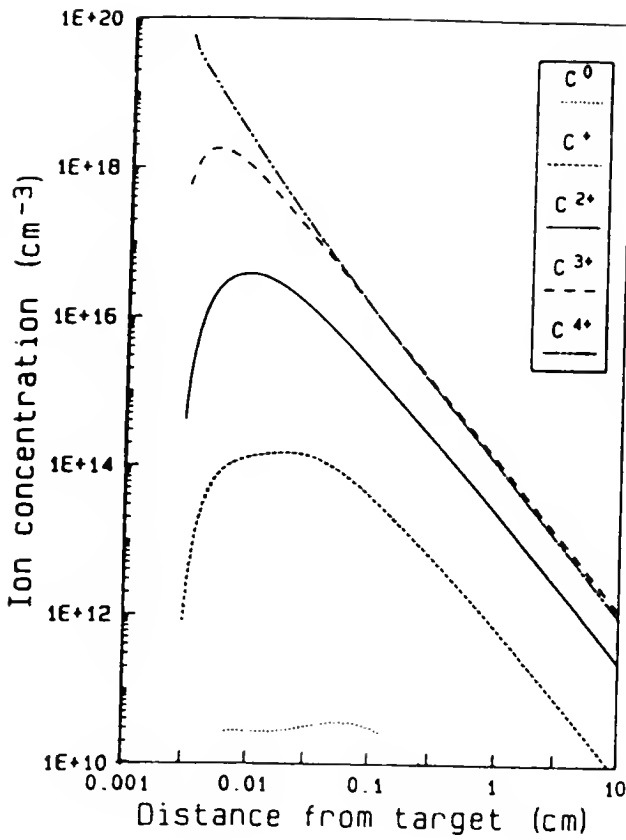
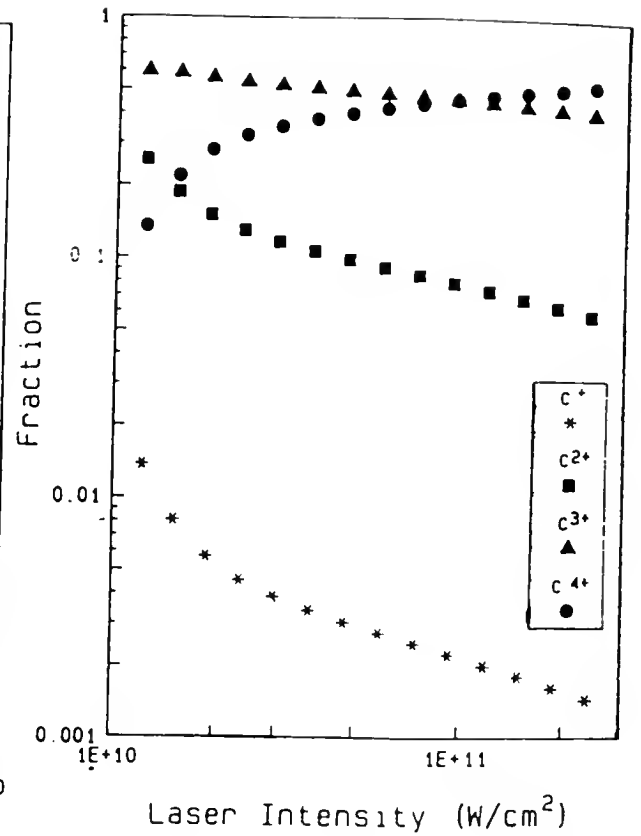Fig. 2-5 Ion concentration as a function of distance from the graphite target, at 5 x 10^10 W/cm² [81].

Fig. 2-6 Fraction of various carbon ions characterized by 'frozen ionization' as a function of laser intensity [81].

by Puell [76], with Z = 4, R = 15 μm, and a laser intensity of 1.2 x 10^{11} W/cm^2, an ion kinetic energy of 1000 eV can be estimated. Even higher ion energies are expected at greater laser intensities. The authors used these results to suggest that diamond-like carbon films are the product of multiple charged plasma ions with high kinetic energies.

Femtosecond Laser Plasma

One apparent difference between the laser-solid interactions induced with nanosecond and femtosecond lasers is that much higher intensity levels can be obtained with the short femtosecond pulses. With near-UV excimer and Q-switched Nd:YAG lasers most commonly used in PLD of thin film materials, the highest attainable laser intensity is usually in the 10^{11} W/cm^2 range. On the other hand, a laser pulse with a 50 fs pulsewidth and 100 mJ energy can produce a laser intensity up to 10^{18} W/cm^2 when focused. Laser intensities in the 10^{14} - 10^{16} W/cm^2 range can be easily achieved with a CPA Ti:Sapphire system, such as the one used in our study.

At laser intensities greater than about 10^{11} W/cm^2, atoms and molecules become unstable. The oscillating electric field E (V/m) is inherently related to the laser intensity I (W/m^2) by [84]:

$$I = 2n(\frac{\varepsilon_0}{\mu_0})^{0.5}|E|^2 = \frac{2n}{Z_0}|E|^2 \qquad (2\text{-}27)$$

where n is the refractive index, ε_0 = 8.85 x 10^{-12} F/m, μ_0 = 4π x 10^{-7} H/m, and Z_0 = 377 Ω. With a laser intensity of 10^{14} - 10^{16} W/cm^2, an electric field on the order of 10^8 - 10^9 V/cm can be induced on the target surface. This value is comparable to the Coulomb field binding the carbon electrons to their atomic cores. As a result, an intense femtosecond laser pulse can ionize a carbon atom through non-thermal processes, even when the photon energy is much less than the atom's ionization potential. Multiphoton ionization (MPI) and tunneling ionization (TI) are two of the possible mechanisms. These two

ionization mechanisms are closely related to each other.

MPI is a nonlinear material response to a strong laser field, where an atom with an ionization potential φ ($\varphi > h\nu$, $h\nu$ is the laser energy) simultaneously absorbs n photons and releases an electron. In this process, n equals the integer part of $\varphi/(h\nu + 1)$. When n >> 1, the TI mechanism better describes the nonlinear ionization process: the ac laser field greatly distorts the atomic Coulomb field so that a bound electron has a high possibility of escaping by quantum tunneling through the Coulomb potential well during half an optical cycle, near the maximum of the optical field. The transition from MPI to TI can be characterized by the so-called Keldysh or adiabatic parameter υ:

$$\upsilon = (\frac{8\pi^2 m \nu^2 \varphi}{e^2 E^2})^{0.5} \tag{2-28}$$

When $\upsilon > 1$, multiphoton ionization process applies, otherwise tunneling ionization is more appropriate in describing the ionization process.

Further ignition of the plasma by an intense laser field is believed to be an electron avalanche process. It is initiated by a small number of free electrons floating in space close to the target surface. These electrons, which may originate from laser induced multiphoton ionization, can gain enough energy from the laser light to impact ionize an atom in collision. Repetition of this process leads to a rapid multiplication of electron, i.e., an electron avalanche process is said to have started. These electron-ions (atom) collisions, generally termed as inverse bremsstrahlung, may be accompanied by cascade ionization to further increase the plasma ionization ratio. Free-free transitions between the plasma electron and incident light cause intense heating of the plasma, followed by a rapid hydrodynamic expansion of the plasma in the form of a shock wave.

The above sequence of events play out differently for a short Ti:Sapphire laser pulse ($\sim 10^{-13}$ s), when compared with a relatively long Nd:YAG pulse ($\sim 10^{-9}$ s).

For a nanosecond laser pulse, when the peak of the pulse reaches the plasma, its density gradient at the solid-vacuum interface would have already relaxed to a density scale-length defined as:

$$d = n_e(\frac{\partial n_e}{\partial x})^{-1} = v_s(\tau/2) \tag{2-29}$$

where n_e is the electron density, τ is the laser pulse duration, and $v_s = (ZkT_e/M)^{0.5}$ is the plasma acoustic velocity. For a 7 ns Nd:YAG pulse with a laser intensity of $10^{10} - 10^{11}$ W/cm^2, assuming $Z = 4$ and $kT_e = 10$ eV, v_s is calculated to be on the order of 10^6 cm/s. Its density scale-length d thereby is at least 10000 nm, which is much longer than the laser wavelength of 532 nm. Under this situation, the laser light will propagate in a long underdense plasma up to the critical density surface, where electron density equals 3.9 x 10 ^{21}/cm^3, and be reflected. Beyond this critical density layer the laser field can only tunnel (decay exponentially) through a distance up to the skin depth defined as:

$$\delta = c/\omega_p \tag{2-30}$$

where c is light speed, ω_p is the plasma frequency. For a Nd:YAG laser with a ω_p of 3.54 x 10^{15} s^{-1}, δ is estimated to be ~135 Å. This skin depth is much less than the laser wavelength of 532 nm and the density scale-length, therefore no energy carried by the trailing laser pulse is directly deposited into the solid surface. Rather, this energy is absorbed by the plasma to further elevate its temperature.

On the other hand, when an ultrashort Ti:Sapphire laser pulse hits the target, a distinctively different plasma will be created. This plasma would have an electron temperature up to at least a few hundred electronvolts and a plasma density on the order of several 10^{23}/cm^3, both of which are much higher than those induced with longer nanosecond pulses at lower intensities. This plasma density is now comparable to the solid density of graphite ($n_g = 1.13$ x 10^{23}/cm^3), i.e., a solid density plasma is created. The target lattice, or more precisely the target ions, however, will remain relatively cold during

the span of the femtosecond pulse. This is because the electron-ion equilibrium time is on the order of about one picosecond. As a result, a two-temperature plasma with "hot" electrons and "cold" ions is formed. Thermal equilibrium among themselves is only achieved after the pulse has terminated. In the meantime, this solid density plasma undergoes little expansion because of the extremely short pulse duration. The plasma-vacuum interface remains relatively sharp when the pulse peak arrives. For instance, when a 100 fs pulse strikes a carbon target at laser intensities of 10^{14} - 10^{16} W/cm^2, assuming Z = 6 and T_e = 200 eV, v_s is calculated to be on the order of 10^7 cm/s. The density scale-length d is thus on the order of several tens of angstroms, similar to the laser skin depth and much less than the laser wavelength of 780 nm. This would allow a significant amount of laser energy to be deposited at densities much higher than the critical density, which is calculated to be 1.8 x 10^{21}/cm^3 for the 780 nm Ti:Sapphire laser light.

Figure 2-7 illustrates the differences between the plasmas induced with a 100 fs and a 7 ns laser pulse.

It would be interesting to compare the plasma ion kinetic energy and charge state induced by these two types of laser pulses, on a time scale relevant to laser deposition of thin film materials. However, little information is available at the present time on femtosecond laser induced plasma expansion. Most research efforts have so far been concentrated on the high field physics associated with this short scale-length, high-density plasma. Time scales of interest for these topics are usually within a few picoseconds after the laser onset, and ion kinetics seems to be of less importance.

As mentioned earlier, within the first picosecond or so after the laser incident, the femtosecond laser generated plasma has two distinctive temperatures: one for the "hot" electrons and one for the "cold" ions. Temperature, meanwhile, is a representation of the average kinetic energy of a plasma constituent in thermal equilibrium. A two temperature plasma is hence nonthermal, and thermal equilibrium is only achieved after the pulse termination. During this non-thermal span, no existing model can sufficiently describe the

100 Femtosecond Laser Pulse   7 Nanosecond Laser Pulse

Ne $>10^{23}/cm^3$ Ne $\sim 10^{20}-10^{21}/cm^3$

Laser   Laser

~ 100 Å ~ 1 mm
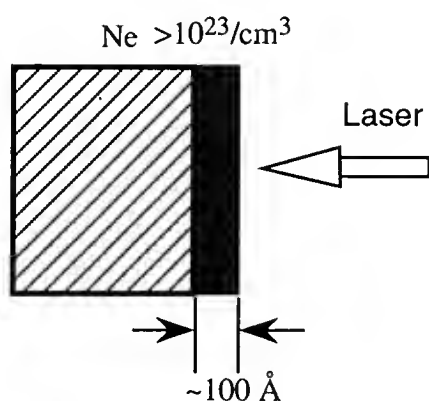
• Solid Density Plasma   • Long Density Scale-length Plasma
• High Electron Temperature   • Strong Plasma Absorption
• High Ion Charge   • Medium Electron Temperature and Ion Charge
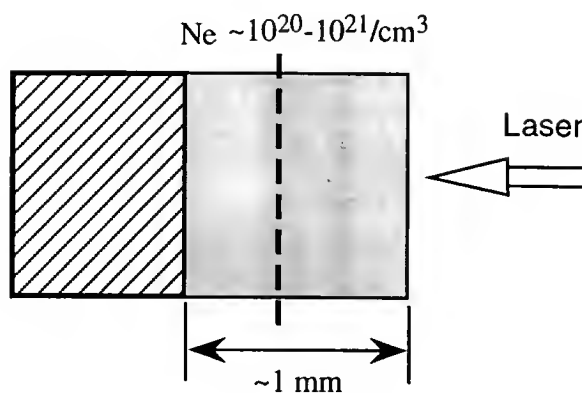
Fig. 2-7 Differences between femtosecond and nanosecond laser induced plasmas.

plasma kinetics, such as the electron temperature or ion state evolution inside the plasma. On a longer time scale, however, both the nanosecond and femtosecond plasmas can be treated similarly as in local thermodynamic equilibrium, or LTE.   LTE refers to the situation where the average plasma thermal energy is a function of space, and yet the ions kinetic energy has a Boltzmann-Maxwellian like distribution.   LTE is a valid assumption only if the collisional process dominates the radiative process, and if the electrontemperature does not change rapidly on time scale of the inverse ionization or recombination rates.   It has been demonstrated that regardless of the laser pulsewidth, LTE can adequately estimate the plasma ion charge states as long as the electron densities are higher than 10^{17} - 10^{18} /cm^3, and electron temperature does not exceed a few hundred electronvolts [85].   Saha equation can then be equally applied to both nanosecond and femtosecond plasmas considered in our study, to predict the ion density with different charge states:

$$\frac{N_{j+1}}{N_j} = \frac{2Z_{j+1}(T)}{Z_j(T)N_e h^3} (2\pi \, m_e kT_e)^{1.5} \exp(\frac{-U_j}{kT_e})$$ (2-31)

here $Z_j(T)$, $Z_{j+1}(T)$ are the partition functions of ion state j and $j + 1$, respectively. U_j is the ionization potential of ion state i, N_e is the electron density, and T_e is the electron temperature. The partition function $Z_j(T)$ is defined as:

$$Z_j(T) = \sum_i g_{i,j} \exp(-U_{i,j} / kT)$$ (2-32)

where $g_{i,j}$ is the statistical weight of quantum number i in the ion state j, and $U_{i,j}$ is the excitation energy of that state.

Liu [86] has studied the laser-plasma interactions induced by a 400 fs (FWHM) pulse on an aluminum target, at laser intensities in the 10^{15} - 10^{17} W/cm^2 range. A Ti:Sapphire laser at 527 nm wavelength was used in his investigation.

For these femtosecond laser pulses, where the gradients in the transverse directions (determined by the laser focal spot) are much less than that in the direction normal to the target surface (defined by the density scale-length), one-dimensional hydrodynamic equations were developed to describe the evolution of the plasma:

$$\frac{D\rho}{Dt} + \rho \frac{\partial u}{\partial x} = 0 \qquad \text{[mass conservation]}$$ (2-33)

$$\frac{Du}{Dt} + \frac{1}{\rho} \frac{\partial p_{th}}{\partial x} = \frac{f}{\rho} \qquad \text{[momentum conservation]}$$ (2-34)

$$\frac{DE}{Dt} + \frac{p_{th}}{\rho} \frac{\partial u}{\partial x} = \frac{Q}{\rho} \qquad \text{[energy conservation]}$$ (2-35)

The above equations are written in the Lagrangean coordinates. The notations are defined as: ρ is the mass density, u is the mean fluid velocity, p_{th} is the thermal pressure, f is the pressure force density, E is the internal energy per unit mass, and Q is the total heat absorbed by the plasma.

These equations were then coupled to a LTE model to estimate the initial ionization degree and electron temperature. For the aluminum target, an initial electron temperature of 100 - 200 eV with an average ion charge Z = 11 (Al^{11+}) was estimated at a laser intensity of 1 x 10^{16} W/cm^2. The ionization potential for the last L shell electron in Al is 442 eV, similar to that of the last K shell electron of carbon (490 eV for C^{6+}). We thereby have adopted kT_e = 200 eV and Z = 6 for the carbon plasma in our study, considering C has a lower atomic weight than Al yet the laser intensities used in our study are also somewhat lower.

Often treated as an ideal gas, the thermal pressure of a laser plasma is related to the plasma temperature by $p_{th} = n_e kT_e + n_i kT_i = (1 + Z)n_i kT_e$, assuming $T_e = T_i$. As elucidated earlier, a femtosecond laser plasma would have much higher density than that of a nanosecond plasma, in addition to the expected higher kT_e and Z. This should lead to a much higher initial thermal pressure and correspondingly higher pressure gradients. With laser intensities up to 10^{16} W/cm^2, a thermal pressure up to several megabars can be expected. It then seems logical to conclude that a femtosecond plasma will have a higher expansion energy, i.e., the ions would have higher kinetic energies. This seemingly plausible assumption, however, does not necessarily have a bearing upon closer examinations. The reason is that at lower laser intensities such as those induced by the nanosecond Nd:YAG pulses, the plasma expansion is determined solely by the thermal pressure force. In this free expansion situation the plasma velocity is related to the sound speed of the plasma, which is in turn given by the electron temperature. However, at the intensity levels associated with ultrashort femtosecond pulses, the pressure induced by the laser field itself can no longer be neglected. This laser force acting upon the plasma, which is commonly termed as the ponderomotive force F_p, is related to the gradients of the laser electric field E by [70]:

$$F_p = -\frac{e^2}{4m\omega^2}\nabla E^2 \qquad (2\text{-}36)$$

where ω is the laser frequency.

The ponderomotive force F_p is a nonlinear force induced by the gradients in the electric field, resulting from plasma wavebeating with the laser light wave. Since the laser field has a positive slope at the critical surface, the net effect of this ponderomotive force is thereby to counteract the thermal pressure force. F_p acts on the plasma and forces it to pick up an inward momentum opposing the outward momentum induced by the thermal pressure gradients. Though the laser ponderomotive force is a very transient phenomenon and it no longer exists after the laser pulse terminates, it will nonetheless alter the initial plasma kinetics. As a result, the plasma expansion may be temporarily impeded, and the local electron density profile further steepened. Equation (2-36) also implies that independent of its wavelength, a high intensity laser light will penetrate to a specific density in the plasma until its ponderomotive pressure is balanced by the thermal pressure.

It was shown that the ponderomotive force became important at laser intensities higher than about 10^{14} W/cm^2 [87]. Liu's work [86] reaffirmed this observation. He measured the expansion velocity of the plasma critical surface through Doppler shift experiments. By increasing the laser intensity from 1×10^{14} W/cm^2 to 4×10^{15} W/cm^2 on an Al target, he noticed that instead of a large increase of the critical layer velocity, the Doppler shift remained largely unchanged within the experimental uncertainties. This observation clearly demonstrated the repulsive effects of the ponderomotive force to the plasma kinetics. It is expected that a linear increase in laser intensity would have resulted in a roughly linear increase in the plasma temperature. Thus if the ponderomotive pressure played no role, the resulting linear increase in thermal pressure should have led to an increase in the Doppler shift by at least the square root of this change. An even greater increase of the Doppler shift should be expected because of the increased Z at higher plasma temperatures. In Liu's work, if no ponderomotive force was considered, a simulated Doppler shift of the critical layer showed an overestimation of the expansion velocity by a factor of three.

CHAPTER 3
EXPERIMENTAL CONDITION AND CONFIGURATION

The experiments in our study can be divided into two parts. The first part includes the synthesis as well as characterization of the diamond-like carbon thin films, while the second part deals with the understanding of the laser plasma dynamics.

DLC films were made with 100 femtosecond (FWHM) Ti:Sapphire pulses at laser intensities in the 3×10^{14} - 6×10^{15} W/cm^2 range. The film properties were analyzed with various techniques and correlated with the laser intensity. Carbon ion kinetic energy as a function of laser intensity was measured through time-of-flight (TOF) experiments.

Using a Q-switched 7 nanosecond (FWHM) Nd:YAG laser beam, we also deposited DLC films at laser intensities in the 3×10^{10} - 6×10^{11} W/cm^2 range. The deposition parameters used in these experiments are more representative of the conventional PLD techniques. The DLC films made with these nanosecond pulses, along with the carbon ion kinetic energy measured as a function of laser intensity, were studied and served as a reference to the femtosecond experiments.

Chapter 3 summarizes the experimental set-ups in our study. These include a discussion of the laser systems employed, an outline of the vacuum system configuration and DLC film deposition conditions, followed by a description of the TOF experiments.

Laser System

Femtosecond laser deposition of DLC films and plasma analyses were carried out with a solid state Ti: Sapphire laser system, which has been developed as a high field research laser at the Center for Ultrafast Optical Science, University of Michigan. It is based on the principle of chirped pulse amplification (CPA) technique, which enables the

generation of high peak intensity laser pulses with moderate beam energy and extremely short pulsewidth [88].

Figure 3-1 is a schematic of the CPA process. The pulses generated by a broadband laser oscillator are coupled to a passive medium, producing a train of low energy (~10^{-12} - 10^{-9} J) laser pulses with short pulse duration (< 10^{-12} s). One of these pulses is selected to pass through a pulse stretcher, after which the pulse duration is increased by a factor of 10^3 to 10^4 while maintaining its beam coherence. This laser pulse then undergoes a chain of amplifiers that have a combined gain on the order of 10^{10} - 10^{12}, thus increasing the laser energy to several hundred millijoules. This high energy pulse is eventually sent through a compressor which reverses the function of the stretcher. Ideally, the final compressed laser pulse can be as short as the original pulse with a Fourier-transform limited bandwidth. The CPA process thus enables the generation of laser pulses with peak power up to the terawatt (10^{12} W) range.

The use of CPA technique is necessitated by dielectric breakdown of the gain media and optical components induced by the high intensity laser beam. By stretching an intense, ultrashort laser pulse, more energy can be extracted without imposing permanent damage to these elements. For a laser pulse traveling in a normally dispersive medium, its pulse duration will become longer as a result of the group velocity dispersion (GVD) effects. That is, the light group velocity decreases with increasing frequency. As a result, in the original short pulse envelope, the "red" component (light at longer wavelength) travels ahead of the "blue" component (light at shorter wavelength). One will first observe the "red" light and then the "blue" light if he stands facing the direction of pulse propagation. The pulse is in this case dispersed, or stretched. This carrier wavelength variation with time is called a chirp, and thence the origin of chirped-pulse amplification. Because a grating is a highly dispersive optical element, it is often used in pairs as the stretcher in a CPA laser system.
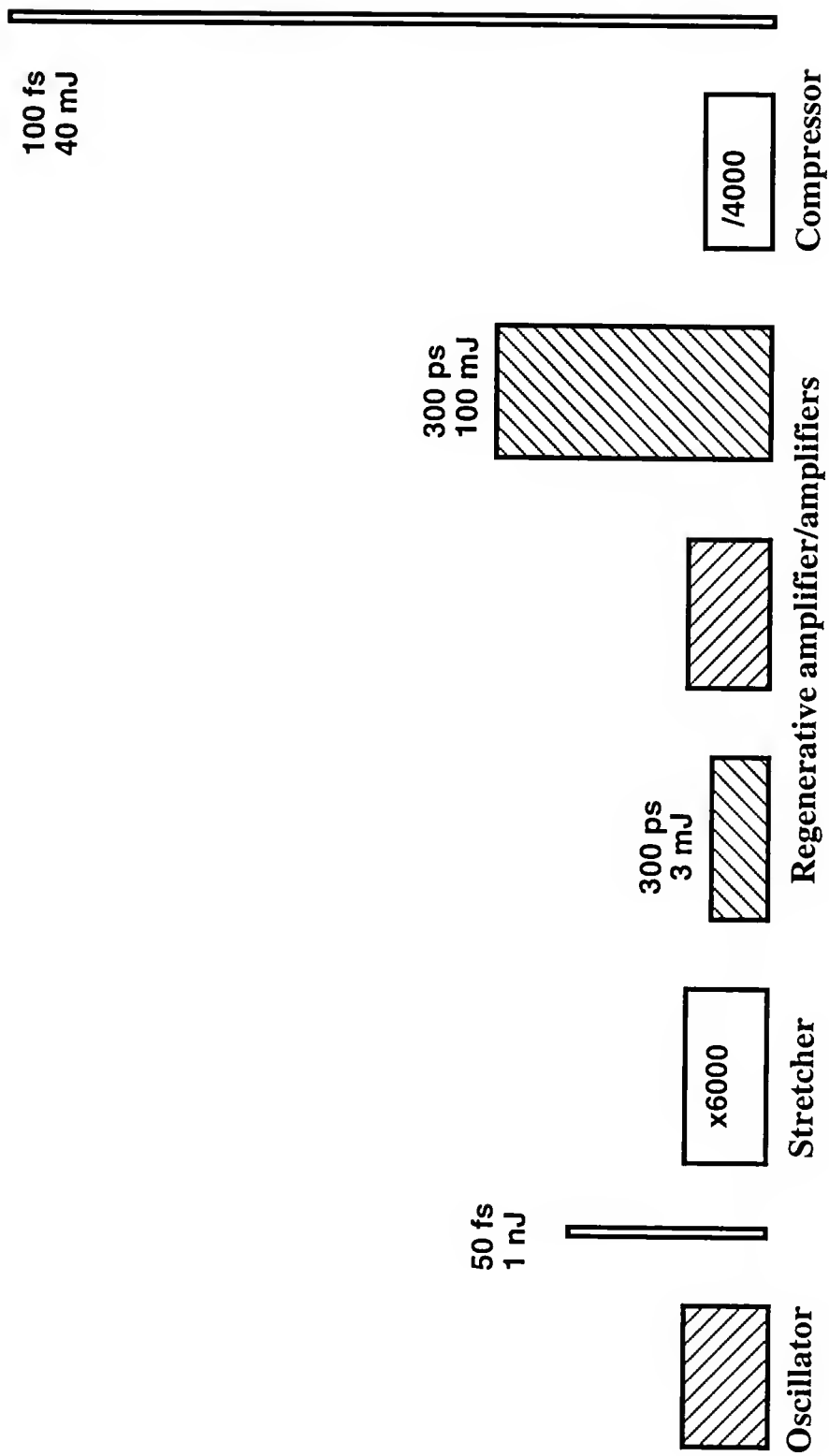
Fig. 3-1 Schematic of the CPA process.

Amplification of the laser pulse is often carried out by several amplifiers working in a stepwise fashion. A Q-switched, cavity-dumped regenerative amplifier, injection-seeded with the stretched pulse, is often used when the laser energy is low. By convention, this amplification stage is termed as the "regen". After the "regen" are a series of single or multiple-pass amplifiers operating in the saturated gain mode, further boosting the laser pulse energy to higher levels.

A second pair of gratings, arranged in a configuration to generate opposite group velocity dispersion to the stretcher grating pair, serve as the pulse compressor. The red component of the laser light, which travels faster than the blue component in the stretcher, is made to travel a longer optical path in the compressor so that the blue component can catch up and eventually overlap with the red component. By doing so, a Fourier-transform limited pulse can be conceived. A Fourier-transform limited pulse, however, is in practice unattainable. As this requires that all the higher order dispersions experienced by the laser pulse, while traveling through various stretching and amplifying stages, are completely compensated by the compressor.

An oscillator material with a broad gain bandwidth is essential in the CPA process. This is because the Fourier transform relation between the laser pulsewidth $\Delta\tau$ and its spectral width $\Delta\nu$ has the form $\Delta\tau\Delta\nu \approx 0.5$. The gain medium thereby must have broad bandwidth to support short pulses. Titanium-doped sapphire crystal (Ti:Sapphire) has a bandwidth over 400 nm, which can in theory generate laser pulses as short as a few femtoseconds.

Figure 3-2 is a schematic of the Ti:Sapphire laser system used in our study.

A self-mode-locked Ti:Sapphire oscillator generates ~1 nJ of output energy, when pumped by an argon ion laser at ~ 4 W of power. These 50 fs, 780 nm pulses are then stretched (temporally chirped) to ~300 ps by double passing them through a stretcher, which consists of two spherical mirrors and two 1200 line/mm, gold-plated holographic gratings. Next, they are injected into a regenerative amplifier pumped by a Q-switched,
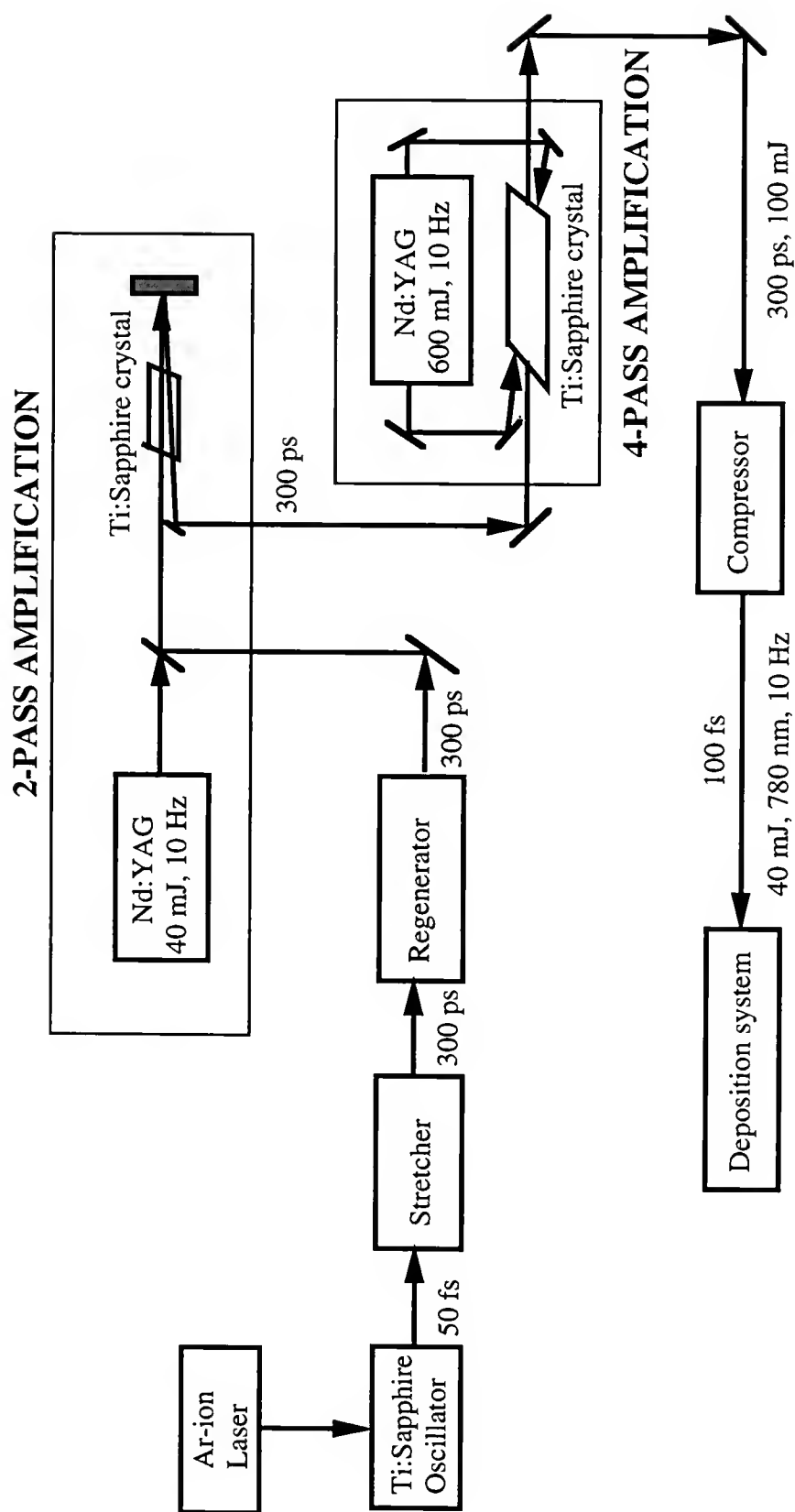
Fig. 3-2 Schematic of the CPA Ti:Sapphire laser system.

internally frequency doubled Nd:YAG laser operated at 10 Hz repetition rate. Typical pumping energy is approximately 40 mJ. This amplifier is made up of an optical resonator that contains the gain media Ti:Sapphire crystal, a Pockels cell, and a thin film polarizer (TFP). The Pockels cell is oriented to give a static quarter-wave birefringence that allows the pulse to enter the cavity. Once the pulse enters the cavity, a quarter-wave voltage is applied to the Pockels cell. The net birefringence is now half-wave, trapping the pulse inside. The pulse is allowed to make approximately 20 round trips in the cavity, allowing most of the energy to be extracted from the gain media and then forced to exit by a half-wave voltage applied to the Pockels cell [89]. Before entering the final compressing stage, these 300 ps pulses are sent through two more stages of amplification, after which they obtain energy up to about 100 mJ. The first amplification stage is made of a two-pass amplifier pumped by the same 40 mJ Nd:YAG laser used in the "regen", and the second one consists of a four-pass amplifier pumped by a second Nd:YAG laser with a maximum output energy of 600 mJ. The final compressor grating pair is comprised of two 2400 line/mm, gold-plated holographic gratings. The compressed pulse is now near Gaussian-shaped, centered at around 780 nm wavelength, with a full-width-half-maximum (FWHM) of 100 femtoseconds. Over half of the laser energy is lost due to compressor gratings absorption, leaving the maximum laser energy out of the compressor at about 40 mJ.

We used a Quanta-Ray® GCR-4 pulsed Nd:YAG system, which also serves as the second amplification pump laser for the Ti:Sapphire system as our nanosecond beam source. A Q-switched solid state laser, this Nd:YAG laser is operated at frequency-doubled 532 nm wavelength and 10 Hz repetition rate. The output beam has a pulsewidth of 7 ns (FWHM) and delivers a maximum energy of 600 mJ. The spatial beam profile is quasi-Gaussian with a near diffraction limited nominal beam diameter of ~ 8 mm. Beam divergence was determined to be ~ 0.5 mrd.
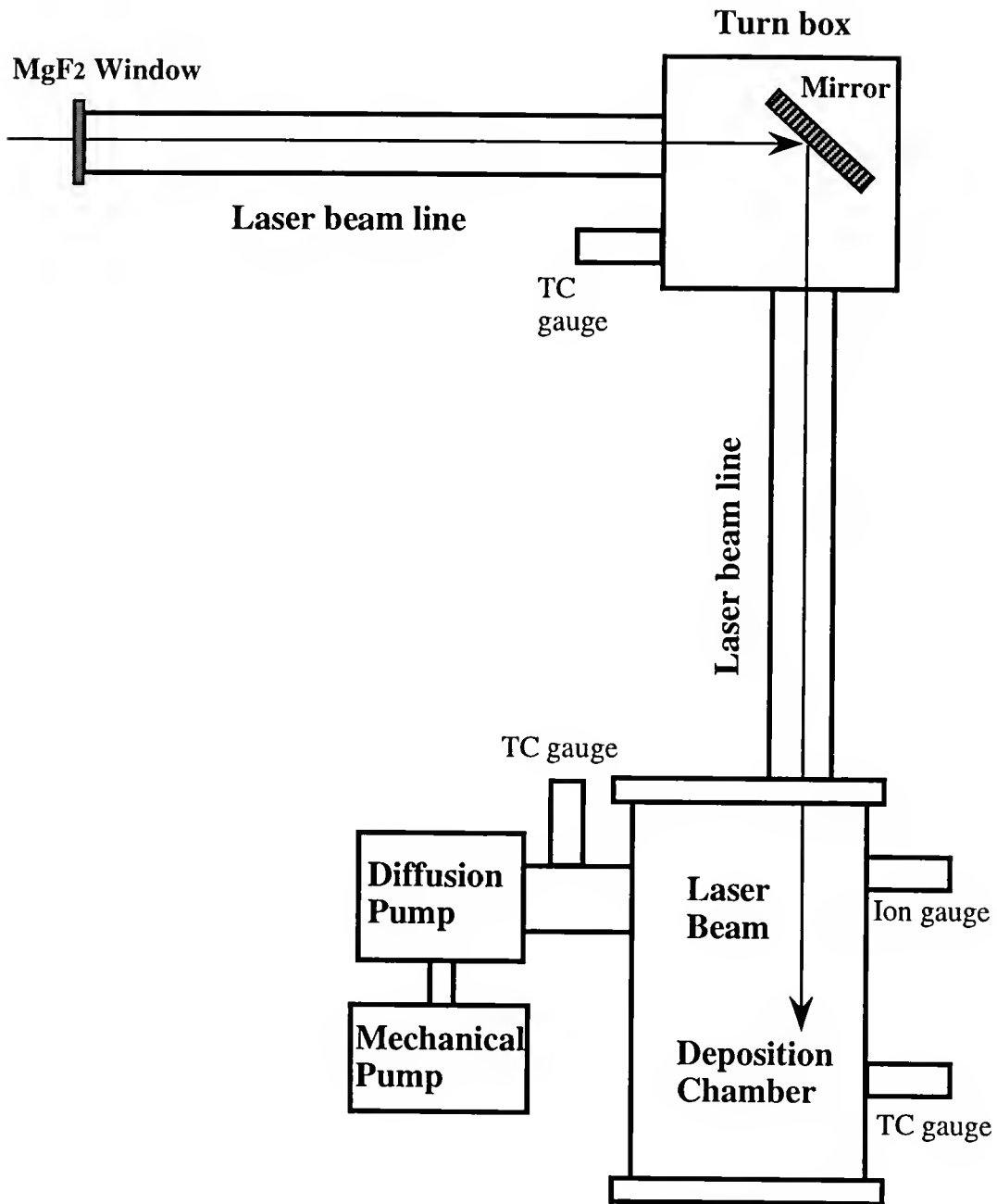
Turn box

MgF2 Window

Mirror

Laser beam line

TC
gauge

Laser beam line

TC gauge

Diffusion Pump

Laser Beam

Ion gauge

Mechanical Pump

Deposition Chamber

TC gauge

Fig. 3-3 Schematic of the high vacuum thin film deposition system.

Thin Film Deposition System

The deposition system consists of a high vacuum deposition chamber coupled with vacuum laser beam delivery tubes. Vacuum pumping was provided by an oil diffusion pump backed by a single stage rotary mechanical pump. A freon cold trap was mounted on top of the diffusion pump to prevent backstreaming of pump oil into the vacuum system. A standard Bayard-Alpert ion gauge and several thermocouple gauges were affixed to the system for pressure measurement. The base pressure of this system was maintained at 2×10^{-6} Torr. Figure 3-3 shows the schematic of the deposition system.

A high purity (> 99.999%) graphite disk, with dimensions of 0.25" x 1.00" from K.J. Lesker Company, was used as the ablation target. It was attached to a target holder rotating at ~ 5 rpm to expose fresh surface for each laser pulse, thereby attenuating the cratering effects caused by the intense laser irradiation. Separation between the target and the substrate was kept at 4 cm during each deposition. Substrates were mechanically secured onto a rotating substrate holder. The design of this triangular-shaped substrate holder allows three samples to be deposited in one operation, yet preventing the laser plume from reaching the substrate not directly facing the target. Alternatively, when high temperature is desired, a self-heating ceramic substrate holder can be used. Inside this hollow block, a high temperature (up to 2100 K) quartz lamp serves as the substrate heating source. Substrate temperature during deposition was monitored by a Chromel/Alumel thermocouple attached to the substrate. It has a measurement range of 0 - 1200 °F.

A plano-convex silica lens with a 12.5 cm focal length was used to direct the nanosecond Nd:YAG laser beam onto the graphite target. The target was placed at a 30° angle with respect to the incident laser beam. Figure 3-4 demonstrates this experimental arrangement.
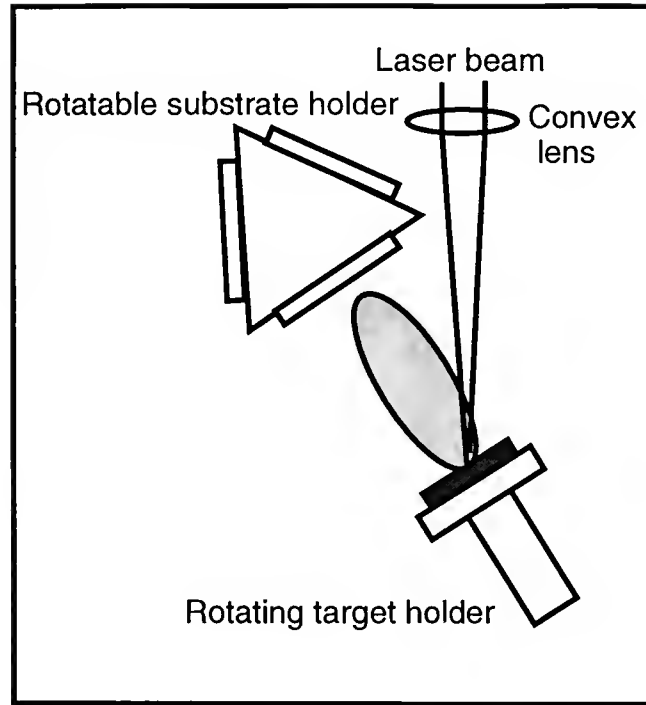
Fig. 3-4 Deposition arrangement for the Nd:YAG laser beam.

The diffraction limited focal spot D_{diff} (at $1/e^2$ intensity), assuming a Gaussian spatial distribution of the laser beam, can be calculated as:

$$D_{diff} = (f\lambda/\pi r) \approx 5 \ \mu m \tag{3-1}$$

where f is the focal length of the plano-convex lens, λ is the laser wavelength and r is the nominal radius of the beam.

The diffraction limited depth of focus L_{diff}, defined by the points along the beam axis on each side of the focal plane where the beam area doubles, is estimated as:

$$L_{diff} = (f^2\lambda/\pi r^2) \approx 165 \ \mu m \tag{3-2}$$

Both D_{diff} and L_{diff} are believed to be much smaller than the actual focal spot and depth of focus on the target. A more realistic estimate of the actual focal beam diameter D and depth of focus L can be obtained as [90]:

$$D = f\psi = 62.5 \ \mu m \qquad\qquad (3\text{-}3)$$

$$L = Df/r \approx 2 \ mm \qquad\qquad (3\text{-}4)$$

where ψ is the Nd:YAG laser beam divergence. Considering that the target is placed at an angle of 30° to the incident beam, a minimum beam diameter of 73 μm should be expected on the target. This compares with a 110 μm damage spot measured on the target surface under an optical microscope. Damage induced by the laser beam is a nonlinear thermo-optical effect influenced by various parameters. These include laser intensity, beam spatial profile, target material thermal conductivity and surface topography, etc. The damage spot therefore is not a true representation of the focal beam size. It, however, has been found to serve well as an upper limit for the beam spot estimation. The Nd:YAG laser intensity cited in this paper was calculated with a focal beam diameter of 73 μm.

The delivery of the femtosecond Ti:Sapphire pulses from the compressor gratings onto the graphite target, on the other hand, is very different from the conventional laser systems. This is due to some of the nonlinear optical phenomena induced by these short, high intensity laser pulses: when the laser induced electric field is higher than 10^4 V/cm, nonlinear response in a medium can no longer be neglected.

As high intensity laser pulses pass through a medium, the dielectric properties of the medium will be altered and they become a function of the local laser field strength. The propagation of the laser beam will in turn depend on the newly modified dielectric properties of the medium. The light-medium interactions are now coupled and nonlinear. Two of the nonlinear effects, self-focusing in the spatial domain and spectral broadening in the temporal domain, are the primary concerns in our experiment. These two effects result from an increase in the refractive index with laser intensity expressed as $\Delta n = n_2|E|^2$, where n_2 is the nonlinear refractive index coefficient, and E is the magnitude of the electric field induced by the laser pulse. For a near Gaussian-shaped Ti:Sapphire pulse, the highest laser intensity and thereby the largest increase of refractive index is at the center of the

beam. Both the laser intensity and refractive index become less toward the edge of the beam profile. In air or other nonlinear media such as a glass vacuum window, this self-induced effect will lead to the curvature of a flat laser wavefront, much like the effect of a positive focusing lens. This self-focusing effect can cause catastrophic damage to optical components in the beam path and totally distort the beam profile. Further more, a broadening or stretching of the short femtosecond pulse in time will lead to miscalculated laser intensity on the target. Distortion and self-focusing of the laser wave-front were in fact experimentally observed on this laser system [91]. Inversely, the plasma generated by an intense laser pulse will generally act as a negative lens, defocusing the light beam. The intensity dependent ionization of the plasma is also non-uniform in the transverse plane of the laser beam, with higher plasma density near the center of the beam than toward the edge. However, the refractive index of the plasma generally decreases with increasing laser intensity, thereby effectively "diluting" the laser beam. The laser light in this scenario is said to have self-defocused.

The combined effects of these nonlinear phenomena, including self-focusing, self-defocusing, beam bandwidth broadening, as well as beam diffraction on the final beam profile constitute a complicated dynamic process and thus beyond the scope of this paper. Our main objective was to minimize some of the potential problems associated with these nonlinear effects.

The nonlinear effects on the laser beam can be quantitatively described by the so-called B-integral, defined as [92]:

$$B = \frac{2\pi}{\lambda} \int_0^L n_2 I(z) dz \qquad (3\text{-}5)$$

where L is the propagating distance of the laser beam in a nonlinear medium, n_2 is the nonlinear index coefficient, and I is the laser intensity. When B exceeds a value of 4 - 5, the beam will break up and can not be well focused. It is therefore imperative to keep the

B-integral to a minimum in our study.

In consideration of the brief discussion above, we implemented vacuum beam lines and all reflective optical components in our femtosecond experiments. Strictly speaking, even in the case of a vacuum, laser light can still interact through vacuum polarization. However, at the intensity level employed in our investigation, nonlinearity caused by photon-photon scattering and other nonlinear effects is too small to warrant any real concern.

In our experiment, the Ti:Sapphire laser pulses out of the compressor gratings were aligned and immediately transferred into the vacuum beam line. A thin 3 mm MgF_2 laser window serves as the front vacuum window. MgF_2 was chosen due to its lower nonlinear index of refraction when compared to a conventional fused silica vacuum window. A p-polarized, high damage threshold reflective mirror positioned inside the turning box redirects the beam into the deposition chamber.

A gold plated aluminum off-axis parabolic mirror was used to focus the incoming Ti:Sapphire laser beam onto the graphite target. The parabolic mirror has a 10 cm reflected effective focal length and a 60° off-axis angle. The parabolic mirror was chosen over conventional glass focusing lenses to eliminate the same nonlinear effects induced by these lenses, which could lead to spreading and distortion of the ultrashort laser pulses. A micron-thick plastic wrap was placed between the substrate holder and the parabolic mirror to protect the mirror surface from laser plume during deposition. Figure 3-5 illustrates this experimental configuration. The final laser energy measured on the target surface was about 60% of its original value out of the compressor.

With the parabolic mirror, a diffraction limited focal spot was calculated to be roughly 1 μm. The actual spot size, however, was measured to be 11 μm. This is due to the combined effects of mirror surface roughness of 80 - 100 Å, as a result of diamond milling of the Al surface, and a slightly divergent beam profile. The beam focal size of 11 μm was measured using an image relay technique: at low laser intensity, a microscope lens

was positioned near the mirror focal and it projected the image of the focal spot onto a charge-coupled device (CCD) camera.

The femtosecond laser beam was capable of breaking down air even at relatively low energy levels. The target was visually placed at the air breakdown spot. Positioning the target precisely at the focal spot, however, proved to be difficult due to lack of a precision motion controller available for the experiments. During actual film deposition, the target was placed at an off-focal position to maintain a larger spot size. This was found to be necessary to keep the otherwise tightly focused beam from cutting a deep trench on the target surface. A minimum beam diameter of 50 μm was used in calculating the Ti:Sapphire laser intensity in our study. This compares with a damage spot of ~ 80 μm found on the target surface under an optical microscope.
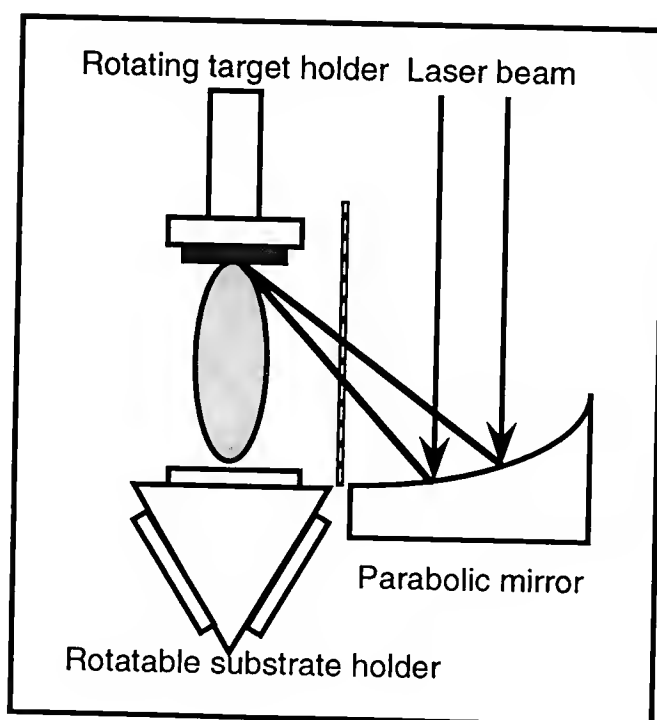

Fig. 3-5 Deposition arrangement for the Ti:Sapphire laser beam.

DLC Film Deposition Conditions

The diamond-like carbon films were deposited onto fused silica and silicon substrates at base vacuum pressure. The SiO_2 (> 99.99% purity) substrates from Kamis Inc. have dimensions of 1 cm x 1 cm x 3 mm. They were optically polished on both sides with roughness < 20 Å. Silicon substrates are n-type, phosphorus doped (100) single crystal wafers cut into 1 cm x 1 cm squares. These substrates were ultrasonically cleaned in acetone and methanol before been loaded into the deposition chamber. Since DLC films are amorphous at room temperature, no special treatment was given to remove the native oxide layer from the silicon wafer.

During the deposition processes, different intensity levels were achieved by varying the incident laser energy and the beam spot size, while keeping the laser pulsewidth constant.

The deposition conditions for DLC films with both the femtosecond and nanosecond laser pulses are summarized in Table 4 and Table 5, respectively.

Table 4. Experimental conditions for Ti:Sapphire laser deposition of DLC films.

Laser Source	Ti: Sapphire (780 nm)
Repetition Rate	10 Hz
Pulsewidth	100 fs (FWHM)
Target-Substrate Distance	4 cm
Minimum Spot Size	50 μm
Peak Intensity	3×10^{14} - 6×10^{15} W/cm^2
Substrate	Si, SiO_2
Substrate Temperature	Room Temperature

Table 5. Experimental conditions for Nd:YAG laser deposition of DLC films.

Laser Source	Nd:YAG (532nm)
Repetition Rate	10 Hz
Pulsewidth	7 ns (FWHM)
Target-Substrate Distance	4 cm
Minimum Spot Size	73 μm
Peak Intensity	2×10^{10} - 6×10^{11} W/cm^2
Substrate	Si, SiO$_2$
Substrate Temperature	Room Temperature

Time-of-Flight (TOF) Measurement Set-up

Time-of-flight (TOF) experiments were conducted to measure the kinetic energy of carbon ions generated by the laser beam. A field-free drift tube coupled with a Faraday ion collector was used for this purpose. The experimental arrangement was similar to that of Demtröder and Jantz [80].

Ion transit time between the target surface and the Faraday cup was measured as a function of laser intensity. The carbon ion velocities were determined with the time lapse between the laser onset and the peak of the TOF distribution curve. This peak corresponds to the most probable carbon ion velocity V_m with a Boltzmann-Maxwellian like distribution. Their kinetic energies can then readily be calculated from KE = $0.5MV_m^2$, where M is the carbon ion mass. Figure 3-6 illustrates the experimental lay out.

Shown in Figure 3-7 is the configuration of the ion drift tube. An outer tube with a diameter of 10 cm is constructed of aluminum. At one end of the tube is an entrance aperture with 2 cm in diameter. At the other end inside this tube is a Faraday ion collector, which is electrically isolated from the tube wall and linked through a BNC
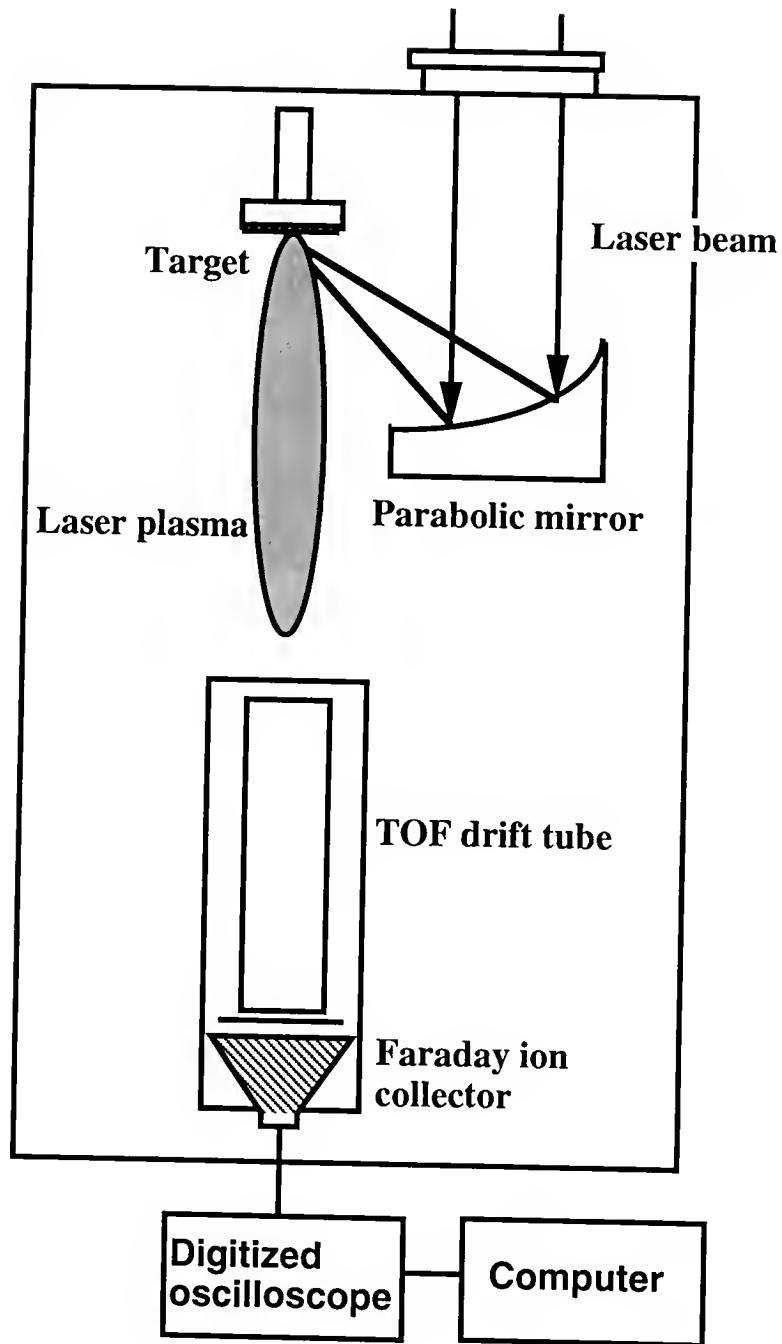
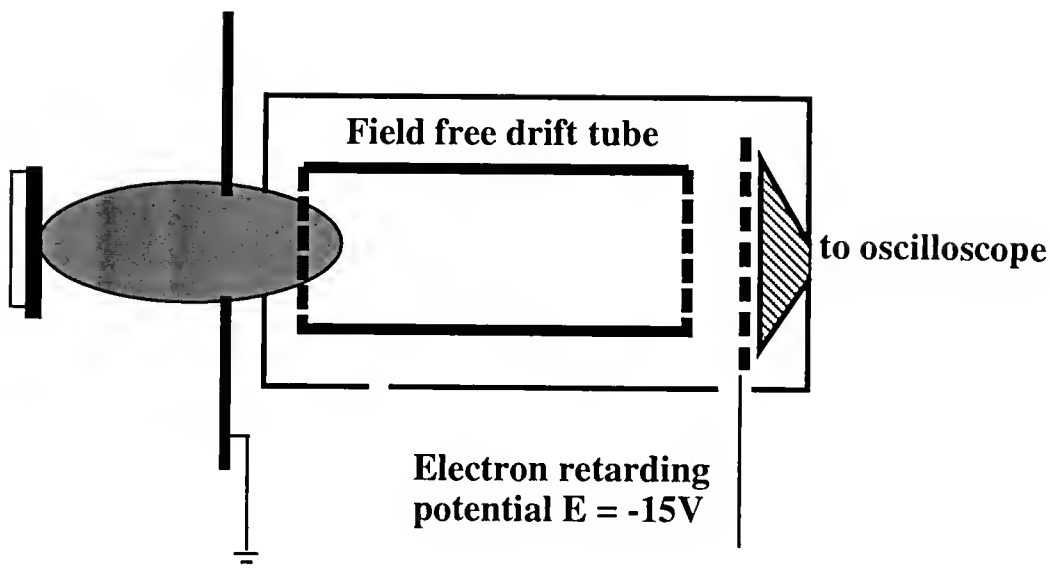Fig. 3-6 Schematic of the TOF experiment.

Fig. 3-7 Layout of the field-free TOF drift tube.

connector to a feedthrough flange on the vacuum chamber. A cylindrical inner tube with a 3 cm diameter and 12 cm in length is positioned coaxially between the aperture and the Faraday cup. It is mounted by four retaining screws to the outer tube. Isolation between the inner and outer tube is achieved by Teflon spacers. On both ends of the tube are finely meshed copper grids, a voltage can be supplied to these grids. This enclosed tube design creates a field-free drift region for the laser plasma and shields the Faraday cup from electromagnetic noises and strayed charged particles. Small holes were drilled on the outer tube wall to allow sufficient evacuation. The outer tube was grounded through the chamber wall and the inner tube was kept floating during the TOF experiments. Between the inner drift tube and the Faraday cup is a fine meshed copper screen. A negative voltage of -15 V was applied to this grid during the plasma ion collection process. This voltage served two purposes. First, it was intended to retard the primary electrons in the

plasma entering the drift tube. The electrons have the same expansion velocity as the ions in order to keep the plasma in quasi-neutrality. However, these electrons have much lower kinetic energies due to their smaller masses, therefore a relatively low negative bias should be sufficient to separate them from the ions. The second function of this negative voltage was to repel the secondary electrons from the Faraday cup generated by the high energy plasma ions.

Ion signals collected by the Faraday cup were monitored by a Tektronix 2440 digital oscilloscope (500 MHz) and relayed through a GPIB card to a computer. The oscilloscope was operated in the external triggering mode with a 50 ohm impedance match. When studying the Ti:Sapphire femtosecond laser plasma, the triggering signal was provided by the Pockels cell wave voltage, which coincides with the onset of each laser pulse. Conversely, the Pockels cell voltage in the resonant cavity generates the triggering signal when working with the nanosecond Nd:YAG laser.

The distance L from the target surface to the entrance aperture of the drift tube was kept at 15 cm for each TOF data acquisition. An additional 16 cm from the entrance to the surface of Faraday cup leads to a total ion travel distance of 31 cm. With an entrance aperture d of 2 cm, the Faraday cup has a collection solid angle of $\Omega = 0.25\pi d^2/L^2 = 1.4 \times 10^{-2}$ sr. The Faraday cup surface was kept perpendicular to the target normal for all the TOF measurements.

CHAPTER 4
RESULTS AND DISCUSSION

This chapter details the experimental results of our investigation. First, results from the time-of-flight (TOF) experiments, which measured the carbon ion kinetic energy as a function of laser intensity, are presented. This is followed by a description of the DLC film properties analyzed by various techniques. The DLC films made by the femtosecond Ti:Sapphire pulses are compared with those deposited with the conventional nanosecond Nd:YAG pulses. A correlation between the carbon ion kinetic energy and the DLC film characteristics is established.

Time-of-Flight (TOF) Measurements

Laser plasma analysis was carried out by the time-of-flight (TOF) experiments described in Chapter 3. Data were taken at a background pressure of 2×10^{-5} Torr with a Tektronix 2440 digital oscilloscope, which has a rising time of 10 ns. The Faraday ion collector surface was kept perpendicular to the target normal during the measurements. Due to rather severe pulse to pulse energy fluctuation (up to ±15%) observed for the Ti:Sapphire laser beam, all TOF data were averaged over eight pulses on the oscilloscope. For the nanosecond Nd:YAG and the femtosecond Ti:Sapphire pulse induced plasmas, their TOF spectra were taken at laser intensities in the 2×10^9 - 6×10^{11} W/cm^2 and 1×10^{14} - 6×10^{15} W/cm^2 range, respectively. For each laser system, the upper intensity limit is typical of the maximum laser intensity used in making DLC films, while the lowest intensity value is determined by the oscilloscope signal/noise ratio.

Figure 4-1a shows a typical TOF spectrum collected on the Faraday cup, from the Nd:YAG beam induced plasma at a laser intensity of 2×10^9 W/cm^2. The "zero time"
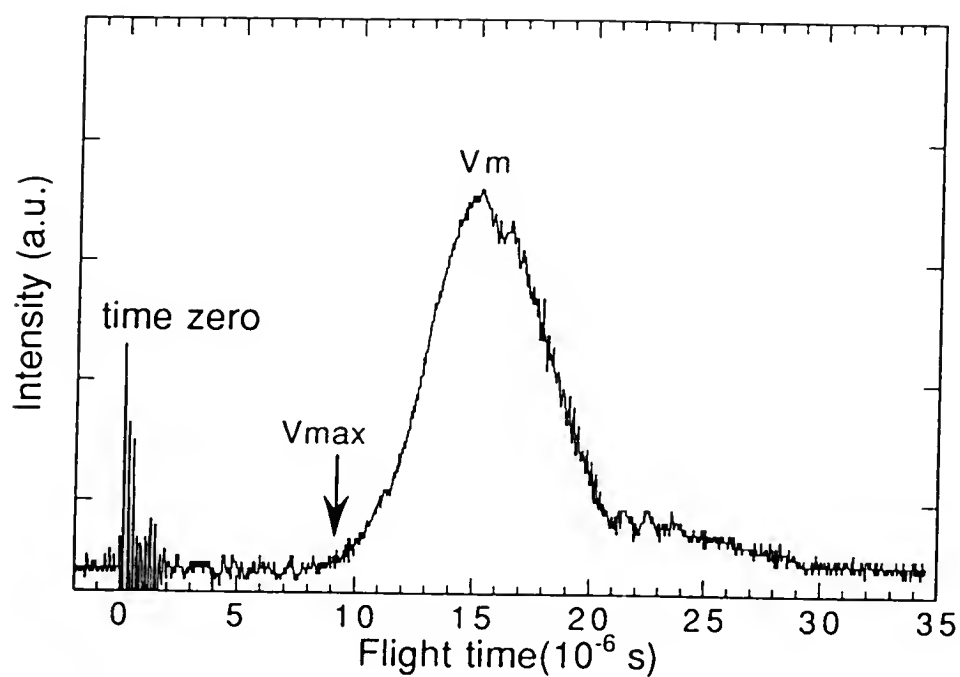
Fig. 4-1a TOF spectrum plotted on the time scale at laser intensity of 2 x 10^9 W/cm².
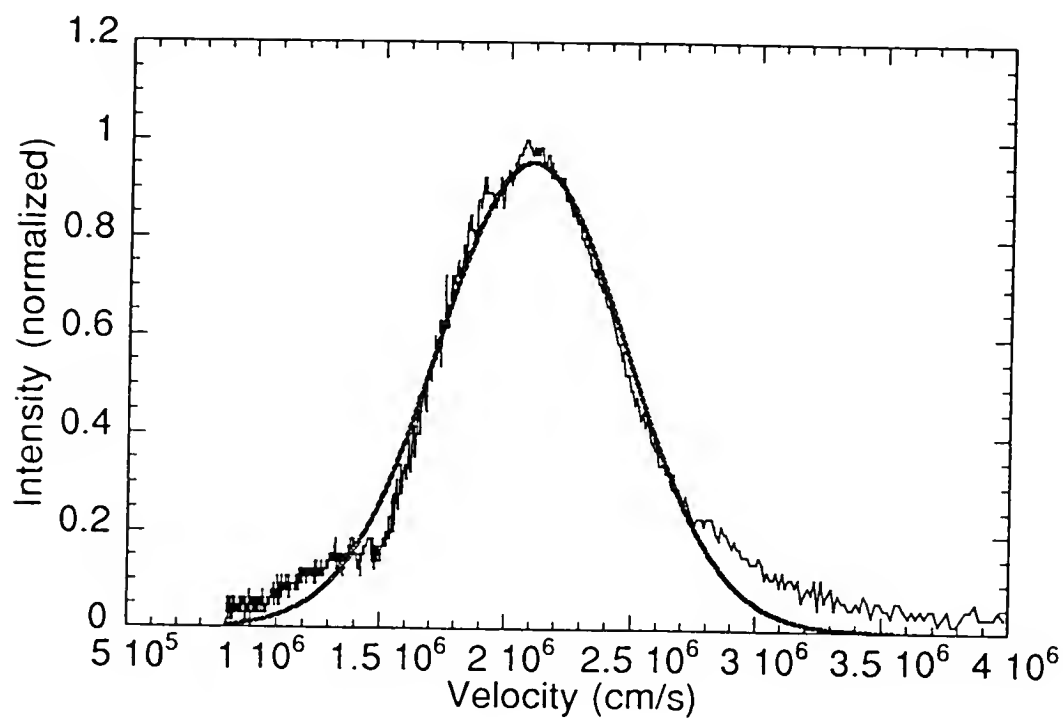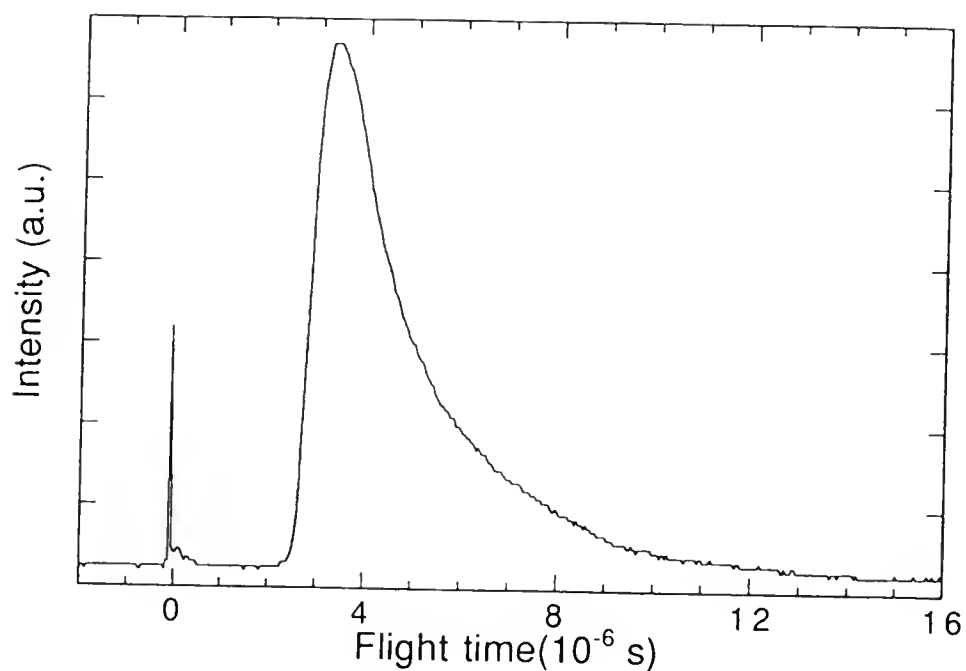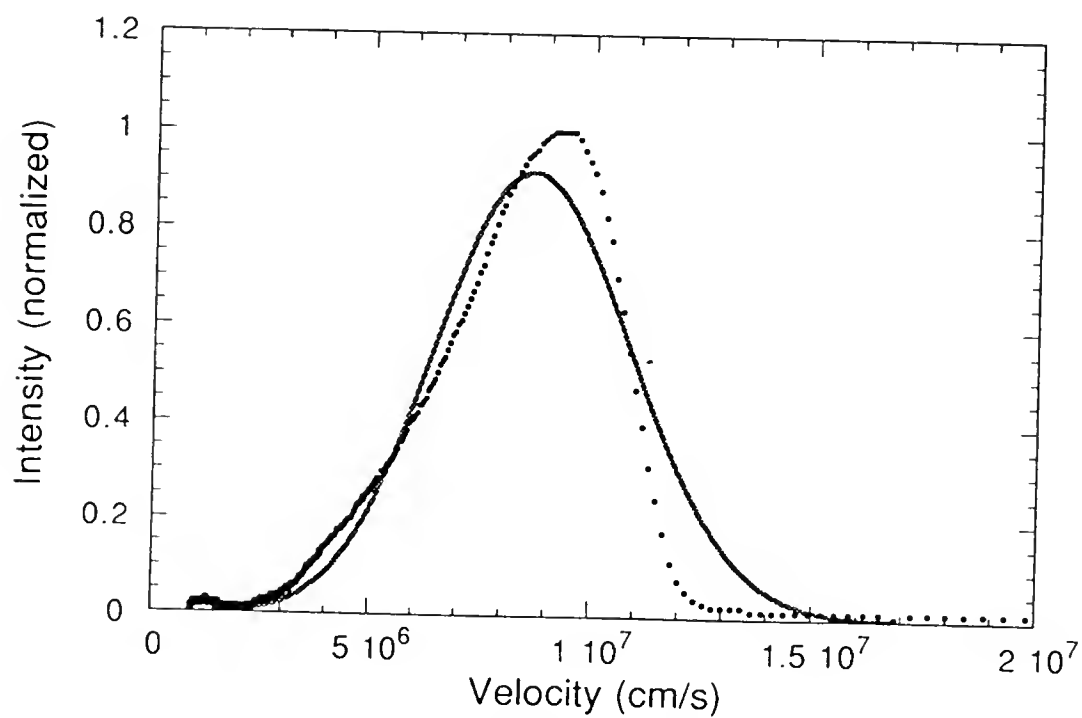

Fig. 4-1b TOF spectrum plotted on the velocity scale at laser intensity of 2 x 10^9 W/cm².

Fig. 4-2a TOF spectrum plotted on the time scale at laser intensity of 2×10^{10} W/cm^2.

Fig. 4-2b TOF spectrum plotted on the velocity scale at laser intensity of 2×10^{10} W/cm^2.
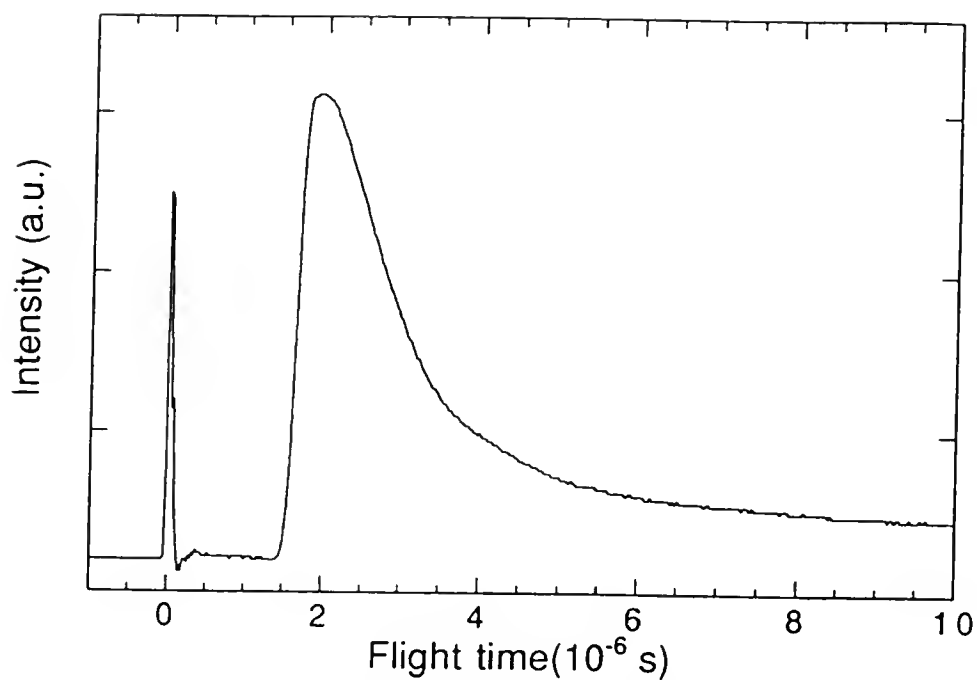
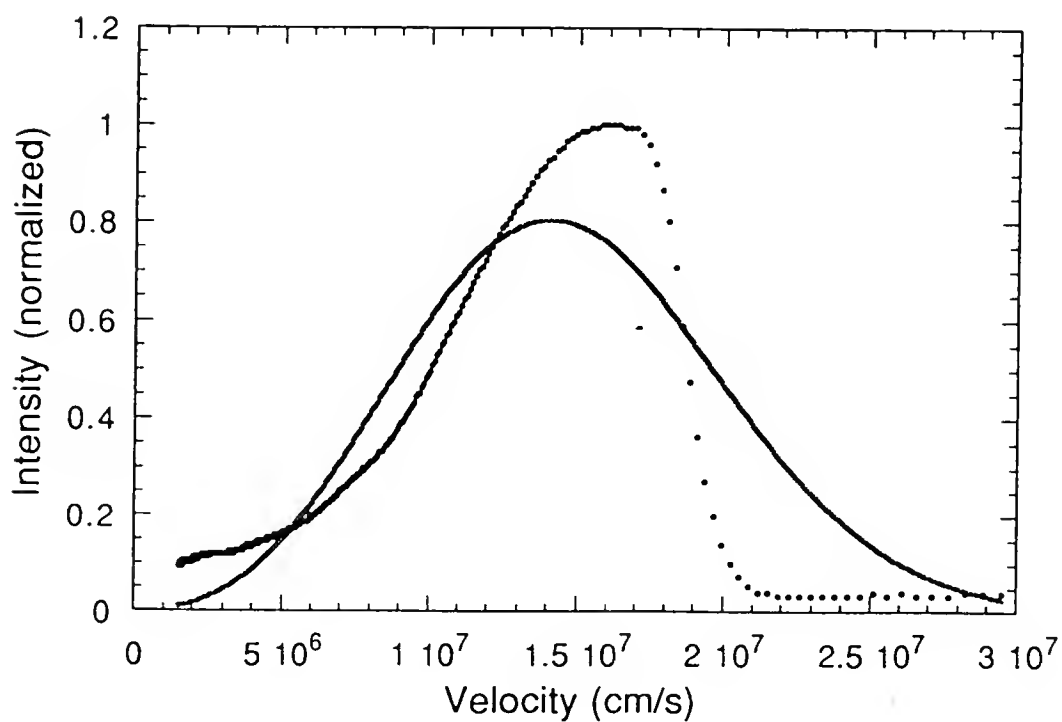Fig. 4-3a TOF spectrum plotted on the time scale at laser intensity of 7 x 10^{11} W/cm^2.

Fig. 4-3b TOF spectrum plotted on the velocity scale at laser intensity of 7 x 10^{11} W/cm^2.
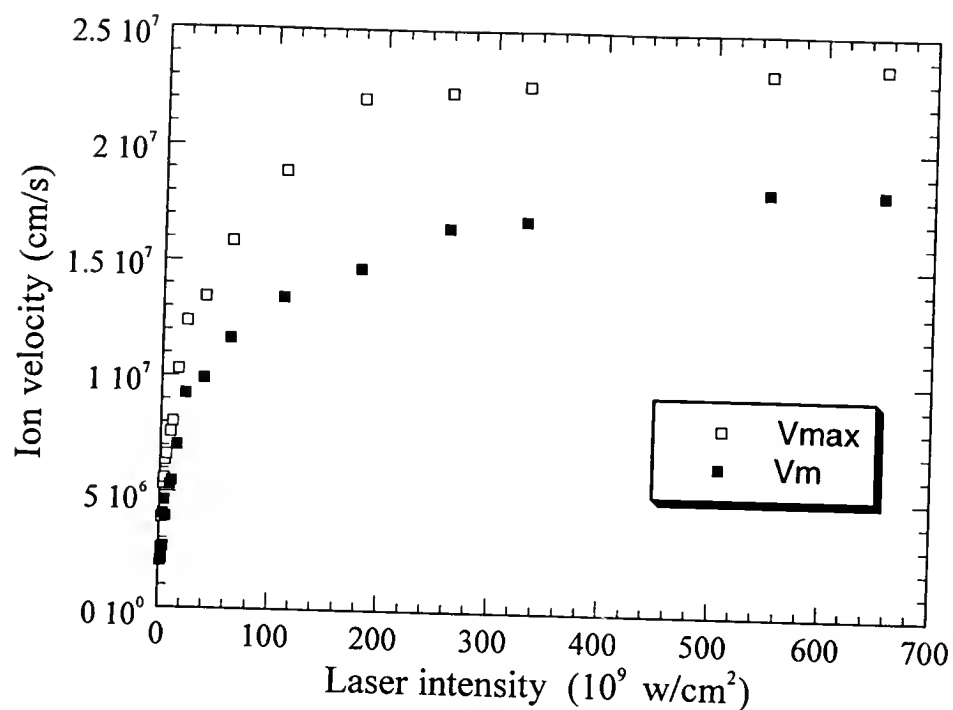
Fig. 4-4 Most probable and maximum carbon ion velocity as a function of laser intensity.
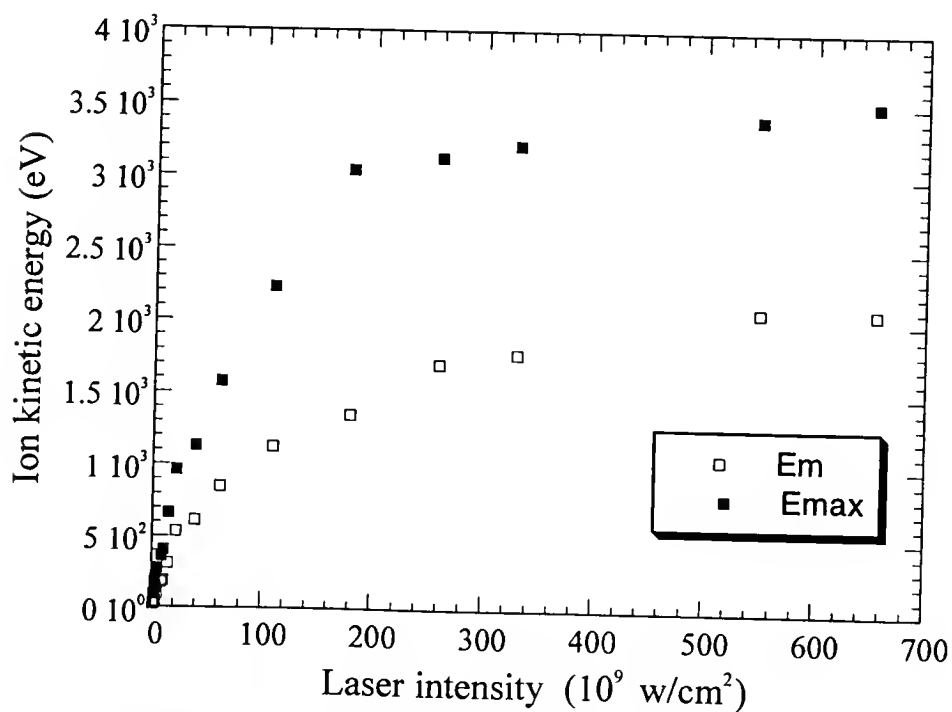

Fig. 4-5 Most probable and maximum carbon ion kinetic energy as a function of laser intensity.

corresponding to the moment the laser pulse strikes the target surface, is referenced by the early spike on the spectrum preceding the main plasma peak. It is generated by the soft X-rays from the plasma. The collected TOF spectrum, with a fast rising front edge and a trailing tail, is characteristic of those produced by a nanosecond laser pulse [94-96]. The main spectral peak yields the most probable carbon ion velocity V_m, and the maximum ion velocity V_{max} is represented by the rising edge of the spectrum. Figure 4-1b is the same TOF spectrum plotted on the velocity scale. It was fitted with a shifted center-of-mass, Boltzmann-Maxwellian like distribution of the form $f(v) \sim v^n \exp[-m(v-v_{cm})^2/2kT]$. The best fit, shown as the solid curve in Figure 4-1b, was obtained with the power law factor n = 2 and a center-of-mass velocity $v_{cm} = 2.1 \times 10^6$ cm/s. The fact that their TOF spectrum can be fit with a Boltzmann-Maxwellian function implies that the plasma ions, upon reaching the Faraday cup, are in local thermal equilibrium. At higher laser intensities, the TOF spectra exhibited similar features, except that the main ion peak as well as its rising edge have shifted toward shorter time scales, indicating an increase in both the median and maximum carbon ion velocities. Shown in Figure 4-2a and Figure 4-3a are the TOF spectra taken at laser intensities of 2×10^{10} W/cm^2 and 6×10^{11} W/cm^2, respectively. Their velocity distributions, however, appear to have deviated from Boltzmann-Maxwellian function. This is because at higher intensity levels, the shape of the TOF curve is determined by ions which have experienced acceleration based effects and therefore can no longer be described by a thermal equilibrium state. The fits to data curves are also plotted as solid lines in Figures 4-2b and 4-3b.

Figure 4-4 illustrates the most probable (V_m) and maximum (V_{max}) carbon ion velocity calculated as a function of laser intensity. Their values increase rapidly at lower intensities and then start to level off in the 10^{11} W/cm^2 range. Because the Faraday ion collection design does not yield the carbon ion mass/charge information, its kinetic energy was calculated based on the assumption that all collected ions are in the atomic form. Figure 4-5 shows the corresponding most probable (E_m) and maximum (E_{max}) carbon ion

kinetic energy as a function of laser intensity. At the highest laser intensity of 6×10^{11} W/cm^2, up to 1.9 keV and 3.5 keV were estimated for E_m and E_{max}, respectively. Data fitting yielded $E_m \propto I^{0.40}$ and $E_{max} \propto I^{0.33}$, with I being the laser intensity. These measured kinetic energy values are in agreement with the simulations presented by Stevefelt and Collins [81], they also compare well with the experimental results of Demtröder [80] and Gregg [93].

It should be noted that even at the lowest laser intensity of 2×10^{10} W/cm^2 used to deposit DLC films, the plasma has a most probable ion kinetic energy E_m on the order of 300 eV. This is higher than those observed with UV excimer lasers running in the 10^8 W/cm^2 range, where E_m was found to be several tens of electronvolts [63,66]. It would be interesting to compare the quality of DLC films deposited by Nd:YAG laser at similar kinetic energies. However, this relatively low kinetic energy level could only be achieved at just above the Faraday cup detection limit of 2×10^9 W/cm^2 ($E_m \approx 25$ eV), where the film deposition rate was extremely low.

As expected, the area under each TOF spectrum, which represents the total ion charge collected by the Faraday cup, increases as a function of increasing laser intensity. This indicates a larger number of generated carbon ions and/or an increase in average ion charge at higher intensities. By measuring the total ion charge, in combination with the knowledge of the film thickness and the ion collector solid angle, we were able to obtain an estimated plasma ion fraction of 0.1 - 1%. This number was calculated based on the assumption that the DLC films deposited at 4 cm away from the target have a density of 3 g/cm^3, and the average ion charge is 3 [29, 53, 54, 81].

In comparison, the TOF spectra taken from femtosecond Ti:Sapphire laser induced plasmas have some strikingly different features. Shown in Figure 4-6a is a typical TOF spectrum taken at a laser intensity of 3×10^{14} W/cm^2. Notice in addition to the main ion peak marked as "V_m", there is a second peak marked as "V_s" in the spectrum preceding this main peak. When converted into ion velocity in Figure 4-6b, this early peak
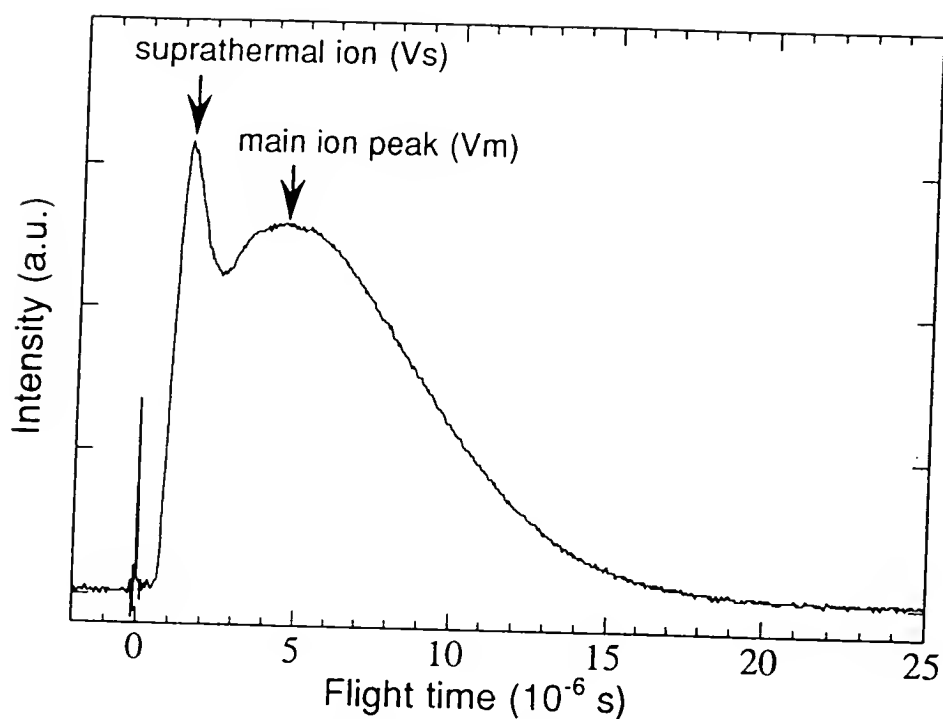
Fig. 4-6a TOF spectrum plotted on the time scale at laser intensity of 3 x 10^{14} W/cm^2.
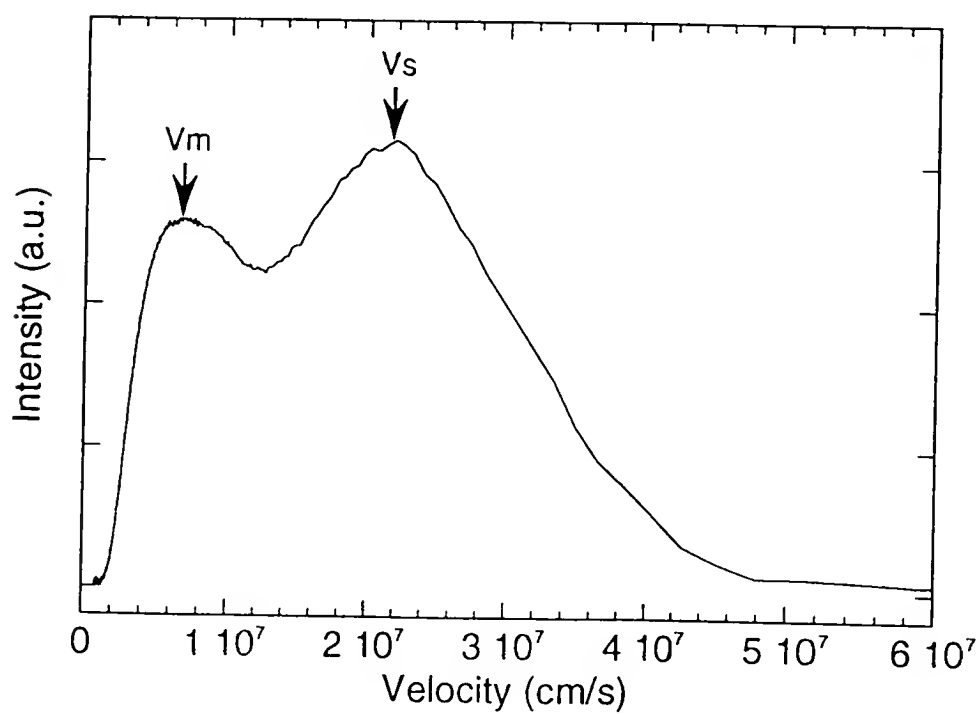

Fig. 4-6b TOF spectrum plotted on the velocity scale at laser intensity of 3 x 10^{14} W/cm^2.

Fig. 4-7a TOF spectrum plotted on the time scale at laser intensity of 1×10^{15} W/cm^2.
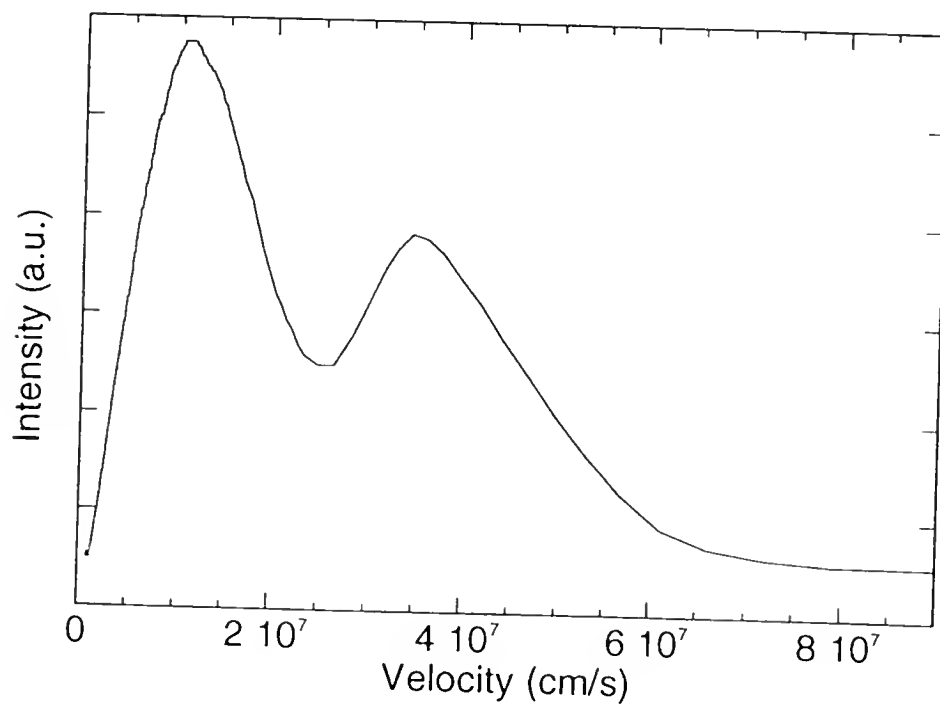
Fig. 4-7b TOF spectrum plotted on the velocity scale at laser intensity of 1×10^{15} W/cm^2.
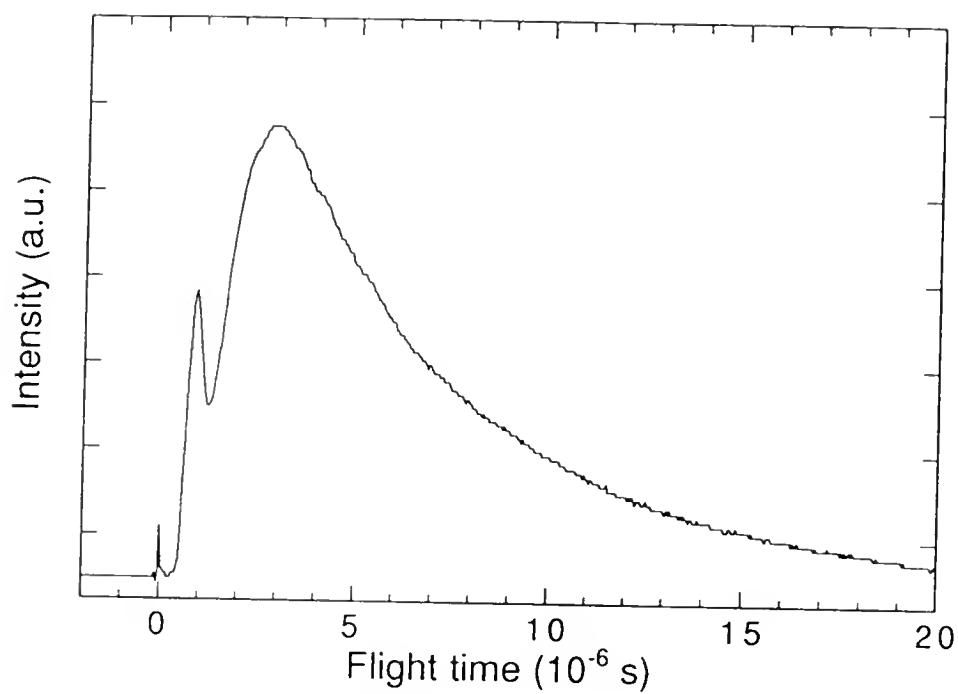
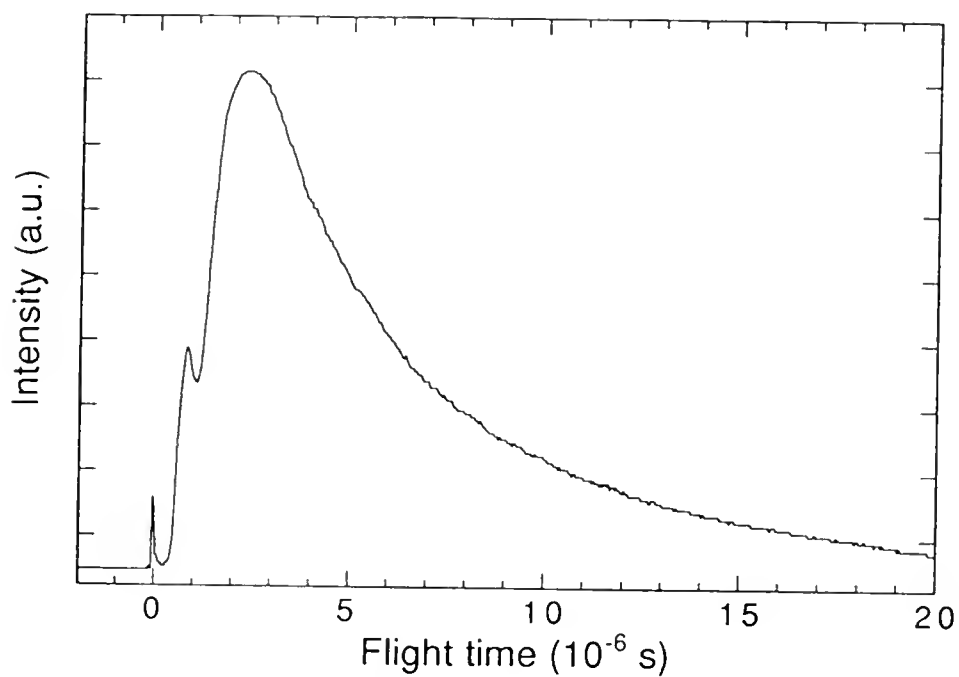Fig. 4-8a TOF spectrum plotted on the time scale at laser intensity of 6×10^{15} W/cm^2.
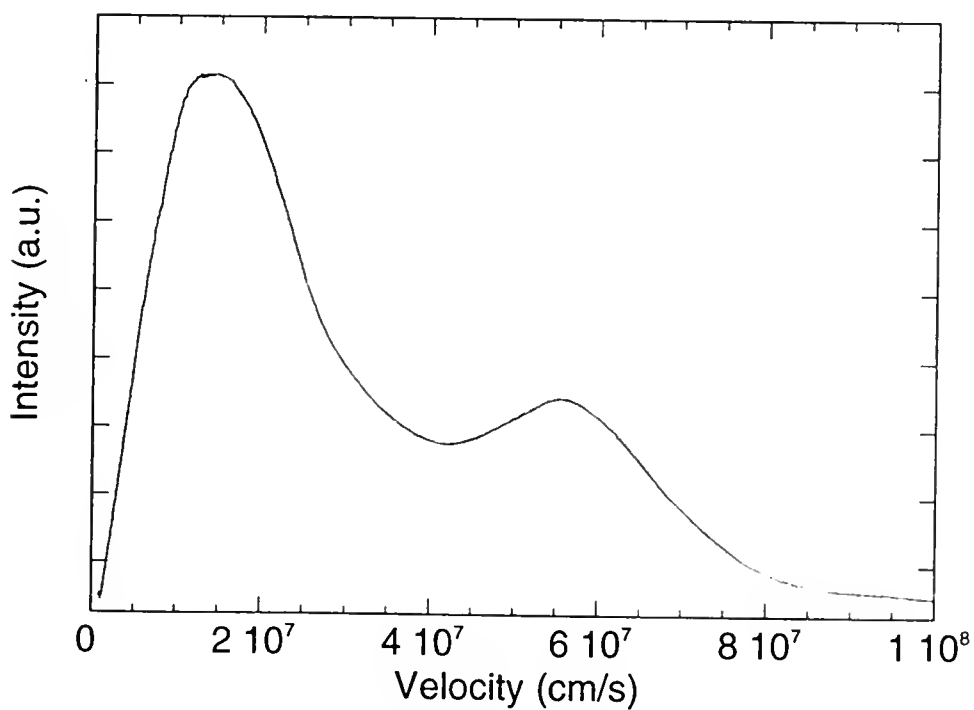

Fig. 4-8b TOF spectrum plotted on the velocity scale at laser intensity of 6×10^{15} W/cm^2.
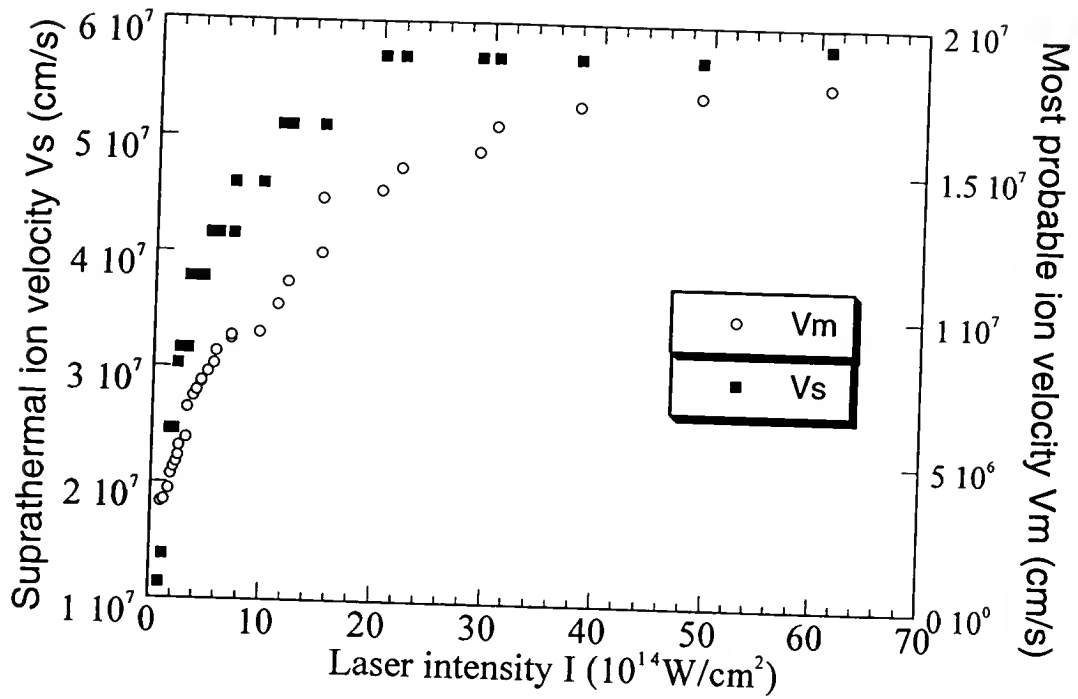
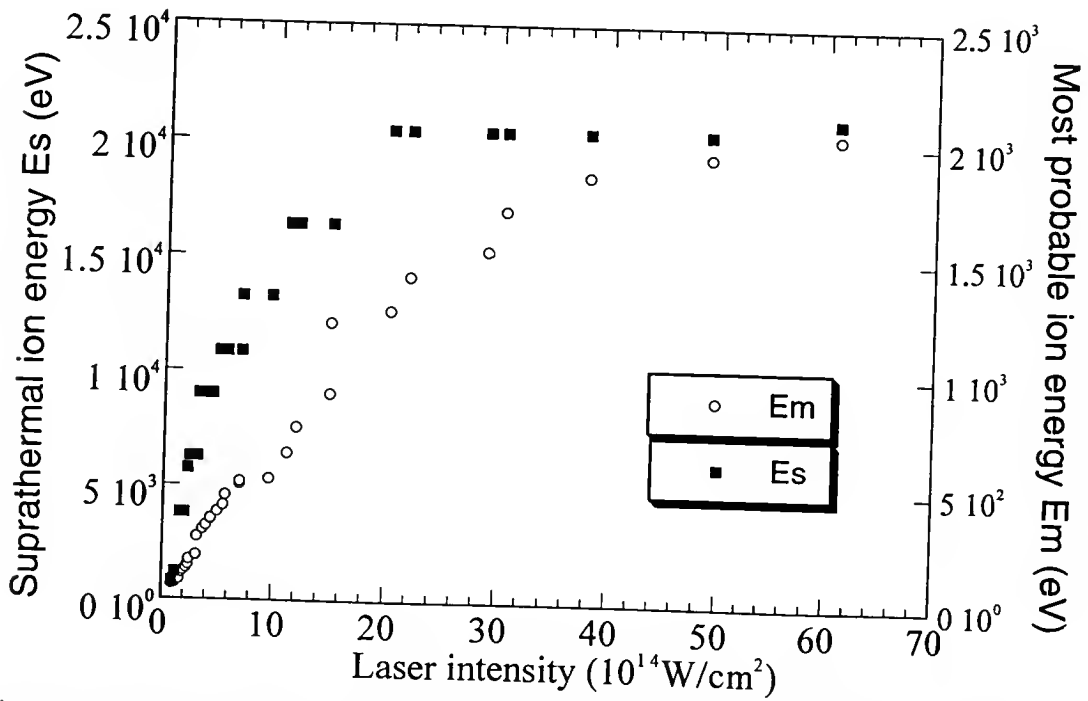Fig. 4-9 Most probable and suprathermal carbon ion velocity as a function of laser intensity.

Fig. 4-10 Most probable and suprathermal carbon ion kinetic energy as a function of laser intensity.

represents a component of the carbon plasma expanding at a much faster speed (V_s) than that of the most probable ion velocity (V_m). At this intensity level, V_m was calculated to be 6×10^6 cm/s, corresponding to a carbon ion kinetic energy E_m of approximately 250 eV. On the other hand, V_s was estimated to have a value of 2.4×10^7 cm/s, corresponding to an ion kinetic energy E_s on the order of 3.5 keV. We designate the carbon ions responsible for the early peak as "suprathermal ions". The presence of suprathermal ions is a unique feature found only in the femtosecond Ti:Sapphire laser induced plasmas. They were not observed in the TOF spectra taken from the less intense nanosecond Nd:YAG pulse generated plasmas. Here the term "suprathermal" is a relative term used with respect to the main ion peak, which itself may have a kinetic energy much higher than that represented by the plasma thermal energy (1eV = 1.16×10^4 K). The main and the "suprathermal" plasma peaks also shifted to shorter time scales at higher laser intensities, similar to those observed for the nanosecond plasmas. Shown in Figures 4-7 and 4-8 are the TOF spectra taken at laser intensities of 1×10^{15} and 6×10^{15} W/cm^2, respectively. The carbon ion velocities V_m and V_s were computed as a function of laser intensity and plotted in Figure 4-9. Assuming atomic carbon ions, their kinetic energies E_m and E_s were calculated and shown in Figure 4-10. The most probable carbon ion kinetic energy E_m assumes a maximum value of ~2.0 keV at a laser intensity of 6×10^{15} W/cm^2. This compares with 1.9 keV measured from the Nd:YAG pulse induced plasma at its highest intensity of 6×10^{11} W/cm^2. The suprathermal ion kinetic energy E_s, however, is at least one order of magnitude higher than E_m at each measured intensity level. E_s reaches a maximum value of ~ 25 keV at 6×10^{15} W/cm^2. Data fitting yielded $E_m \propto I^{0.55}$ and $E_s \propto I^{0.33}$.

To our best knowledge, the observation of suprathermal ions in a femtosecond laser induced plasma has not been reported. This study marks the first time a laser beam deposited DLC film has been condensed directly from such highly energetic ion particles. Though the suprathermal ions constitute only a small fraction of the total ionized particles

generated in the laser plume, they could nonetheless play a significant role in the metastable DLC film structures. In fact, if the optimal ion kinetic energy of laser induced plasma indeed falls between several tens to several hundreds of electronvolts as suggested by earlier experiments, the existence of these suprathermal ions alone could very well push the resultant films over the potential barrier back into the graphitic regime.

The existence of a double-peaked ion distribution, however, does not appear to be limited to femtosecond laser induced plasmas only. There have been similar observations by a number of research groups working in laser-compression studies with longer pulse lasers [97-100]. In their experiments, the suprathermal, or sometimes referred to as the fast ions were observed to travel ahead of a slower moving ion component similar to those found in our TOF spectra. It is interesting to notice that there appears to exist a critical laser intensity level, beyond which a two-component plasma is created, regardless of the type of laser beam used. The exact value of this threshold intensity varies with laser wavelength and pulse duration, but it generally initiates at an intensity level higher than 10^{12} W/cm^2.

Ehler [97] focused a high-powered CO_2 laser onto a polyethylene target. He noticed that at intensity levels higher than 5×10^{12} W/cm^2, the plasma contained fast expanding carbon ions in addition to a slower ion component. He also found that the suprathermal ions tended to be multiple charged, and fully stripped C^{6+} ions had the highest kinetic energies. Using a flux-limit model, he argued that at high laser intensities, the absorbed laser irradiance by the plasma would exceed the energy transfer rate through electron thermal conduction. As a result, suprathermal electrons are produced with energies proportional to the laser intensity as $I^{2/3}$. Because of their small masses when compared with that of the ions, these suprathermal electrons can quickly establish an electric field that accelerates ions to maintain local plasma neutrality. This process gives rise to the formation of the so-called suprathermal ions with energies also scale up with the laser intensity. The fact that carbon ions with higher charge states possess higher

kinetic energies further insinuates that there exists an accelerating electric field within the expanding plasma. Similar TOF features were reported by Pearlman et al. [98]. In their experiments, a Nd:YAG laser was focused onto a polystyrene thin film at intensities in the $10^{13} - 10^{14}$ W/cm^2 range. Faraday ion collectors placed at a distance of 66 cm from the surface registered double-peaked TOF spectra both in front of and to the rear of the target. The separation between the suprathermal and the main ion peak varied from a couple of microseconds to several tenths of one microsecond. The authors also attributed the existence of suprathermal ions to electrostatic acceleration by the plasma electrons. With a KrF laser beam, Gupta et al. [100] saw a two-peak ion distribution from an aluminum plasma at laser intensities between 0.6 and 7 x 10^{12} W/cm^2. The suprathermal ions were found to have an anisotropic distribution. They were only detected at a narrow cone region normal to the target surface. On the other hand, the slow or thermal ion component was nearly isotropic. The suprathermal and slow ions were observed to scale with laser intensity as $I^{0.26}$ and $I^{0.08}$, respectively. The authors proposed that a lateral energy transport mechanism to explain their findings: the suprathermal ion peak originated from the initial hot ablating plasma still undergoing one-dimensional flow, while the slower thermal ions came from the three-dimensional Kundsen layer.

We postulate that the suprathermal ion peak detected in our TOF spectrum arises also from highly charged carbon ions, based on the work of Ehler [97], as well as that of Stevefelt [81]. We were unable to derive the exact ion charge state with our present set up. An electrostatic spherical sector analyzer (ESA) is under construction at the time of this writing. It will be able to distinguish ions with different masses and charges.

Stevefelt has demonstrated that at laser intensities higher than 10^{11} W/cm^2, C^{3+} and C^{4+} ions could remain as the predominant species in the plasma at a distance up to several centimeters away from the target, because of an "ion freezing" effect. Notice in our study the main TOF peaks from both the Nd:YAG and Ti:Sapphire laser induced plasmas have similar energy distributions. This suggests that the suprathermal component are most

likely to have originated from carbon ions with a charge state equal to or higher than 3. The actual TOF signals detected on the Faraday cup, which is placed at 31 cm away from the target in our study, should be a "frozen image" of the plasma charge state near the substrate. Though the average ion charge could be lower than what one may observe at the substrate, due to plasma cooling and recombination. A model is proposed, in the following subsection, to qualitatively explain the suprathermal ion formation in high intensity, femtosecond laser induced plasma.

We believe that the suprathermal ions detected in our study resulted from the generation of suprathermal electrons and the electrostatic field established by these electrons. At laser intensities of 10^{14} W/cm^2 and above, a plasma absorption mechanism called resonant absorption may have played a more important role than the inverse bremsstralung absorption mechanism at lower intensities. At these high laser intensities, when a Ti:Sapphire laser beam is incident on the graphite target at an oblique angle of 60° off the parabolic mirror, the laser wave will be refracted by the density gradient with a turning point at $n = n_c\cos^2(60°) = 4.5 \times 10^{20}$/cm^3, before the critical density surface. For a p-polarized laser beam such as the one used in our experiment, where the laser electric field vector is parallel to the plane of incidence, solution of the Maxwell's equations shows a singularity in the magnitude of the oscillating electric field vector at the point of reflection. The oscillating field can resonantly drive an electron plasma wave to very large amplitude. This resonant singularity may be viewed as a tunneling of the evanescent wave from the turning point to the critical layer, where it resonantly excites a plasma [101]. As a result, oscillatory motion of the electrons due to this abnormally high electric field creates a charge separation, which at a finite electron temperature leads to the propagation of a plasma wave. At finite temperature there is a direct transfer of energy from photons to plasma wave which subsequently coverts its energy to electron thermal energy. This collisionless wavebreaking process in resonance absorption gives rise to the so-called suprathermal electrons.

Suprathermal electrons have been observed in laser fusion studies [102-105], where the laser intensities used are similar to those generated by the femtosecond Ti:Sapphire pulses in our experiment. These suprathermal or fast electrons are characterized by a temperature that is on the order of ten to twenty times higher than the background plasma temperature and scales as $(I\lambda^2)^a T^b$, where a and b generally have values between 0.25 and 0.50. Here I is the laser intensity, λ the laser wavelength and T the background plasma temperature. Particle simulations by Freidberg et al. also showed that a small number of suprathermal electrons could be created as an outward moving stream originating from the critical density region [106].

Due to their small inertia, the plasma electrons will start to move toward the vacuum side once the laser pulse terminates and the balancing ponderomotive pressure no longer acts as an impeding force against the thermal pressure. The much heavier carbon ions, however, will remain relatively "cold" and stationary during the pulse span. In this early stage of plasma expansion, with an electron density on the order of several $10^{23}/cm^3$, the plasma has a Debye length $\lambda_D = 740(T_e/n_e)^{0.5}$ (in cgs units) on the order of only several angstroms. The ions thereby will not be able to feel the effect of the electric field established by the electrons and no ion acceleration occurs until the plasma has expanded to a much lower density level, where the Debye length becomes comparable to the plasma dimensions. The requirement for the plasma as a whole to maintain quasi-neutrality then establishes a time dependent electrostatic potential in the lower density coronal region. Here the suprathermal electrons lead the expansion of the plasma, and through the radial electric field set up by charge separation a fraction of the plasma ions will be accelerated to high velocities according to their charge Z. We believe it is this process that has produced the suprathermal ions observed in our TOF experiments. In the meantime, a return electron current is established by this electric field to maintain both charge and momentum balances [107]. These ions will eventually move at the same velocity as the suprathermal electrons, and their kinetic energy saturates when all the electron energy has

been extracted. Similar argument can be found in the work of Morse [108] and Valeo [109].

A quantitative measurement of the suprathermal ion fraction can be difficult. This is because the TOF peak corresponding to the suprathermal and slow ions is a function of both the particle number and their charge state, which could not be differentiated with the current set up. However, if one assumes that they have the same charge and both assume Maxwellian-like distributions, it can be estimated that at a laser intensity of 3×10^{14} W/cm^2, this ratio is $\sim 10^{-2}$, and it decreases to $\sim 10^{-3}$ at 6×10^{15} W/cm^2. This finding is not well explained and we suspect that the contrast ratio of the Ti:Sapphire laser pulse may have played a role.

There are two factors affecting the contrast ratio in a CPA laser system. One is the so-called amplified spontaneous emission, or ASE, which originates from spontaneous emission from various amplifier stages. ASE is present as a low but rather broad background noise with a time scale up to tens of nanoseconds in the output spectrum. The second factor involves the stretching/compression scheme of the laser system. When there is compressor/stretcher mismatch and/or spectral distortion by the amplifier system, the compressed laser pulse may have pedestals, or "wings" in front of and after the main peak. These pedestals can extend over to hundreds of picoseconds. For a sub-picosecond Ti:Sapphire laser pulse with extremely high intensity, even a relatively small amount of prepulses could generate an underdense plasma on the target surface before the main laser peak arrives. Assuming a background ASE/pedestals with time scales on the order of 1 ns, a minimum contrast ratio of 10^6:1 would be required to eliminate the possibility of a preplasma on the graphite target, even at the lowest laser intensity of about 1×10^{14} W/cm^2 employed in our study. This is because the ablation threshold for graphite was estimated to be around 1×10^8 W/cm^2 [110]. We think that when the laser intensity is increased to higher values, a long density scale-length plasma may have been created before the peak of the femtosecond pulse. As a result, these less intense, long duration prepulses will

generate more "slow" ions in the plasma. They may obscure the TOF signal from the suprathermal, or fast ions induced by the main femtosecond pulse, thus making a quantitative estimation of the suprathermal ion fraction unreliable.

DLC Film Properties

The following sections summarize properties of the DLC films deposited by the nanosecond Nd:YAG and the high intensity femtosecond Ti:Sapphire laser beams. These films were analyzed with scanning probe microscopy (SPM), variable angle spectroscopic ellipsometry (VASE), Raman spectrometry, and electron energy loss spectroscopy (EELS). Topics relevant to the data presented in these sections are discussed.

Scanning Probe Microscopy (SPM)

The DLC films deposited on SiO_2 substrates are visually smooth and largely transparent with a light yellowish tint. Those deposited at higher laser intensities appear to be more absorbing with a dark brownish appearance. The DLC films deposited onto Si substrates have a black and sometimes bluish tint. Color interference fringes can be seen on thinner samples. The films are resistant to razor blade scratch test. They also remain intact after being submerged in a 1:3 $HCl:HNO_3$ solution for over twelve hours, suggesting good chemical inertness. Thicker films, however, tend to buckle and peel off from the substrates once they are removed from the vacuum environment. These observations hold for both Ti:Sapphire and Nd:YAG laser deposited films.

The presence of particulates on laser deposited films has been one of the main factors affecting the usefulness of the PLD technique. For DLC films, though its tribological function is not likely to be affected by the presence of small particles, their desirability in high-performance optical and microelectronic applications, however, will undoubtedly be lessened. A TopoMetrix® 2000 series scanning probe microscope (SPM)
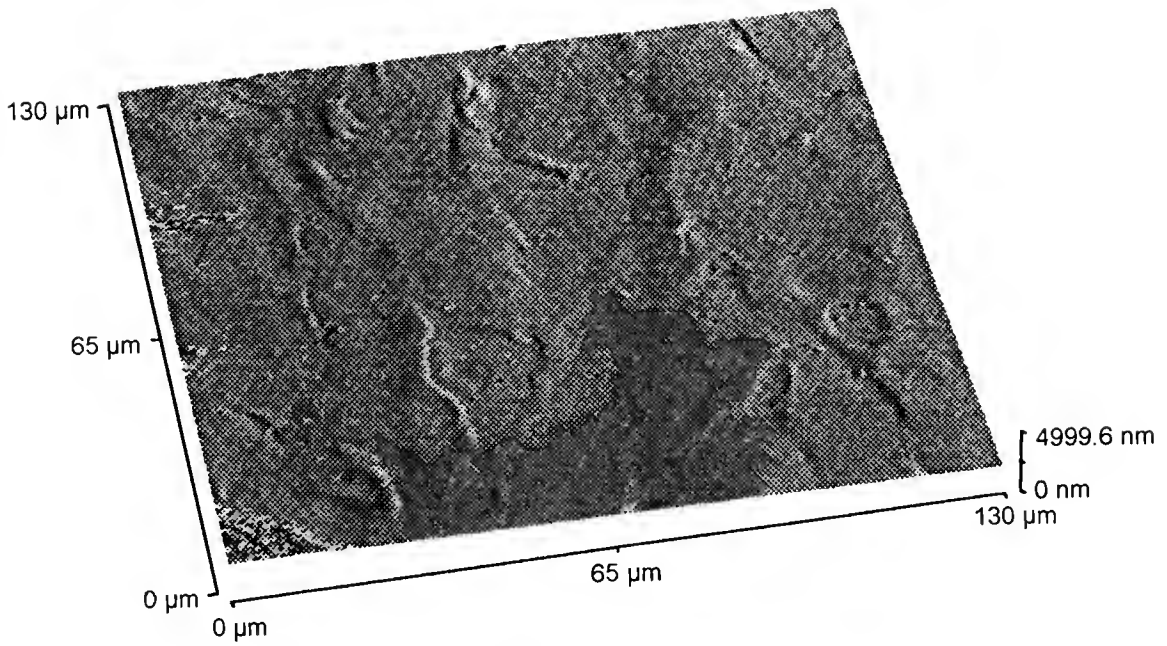
Fig. 4-11 AFM image of DLC film deposited by Nd:YAG laser at 3×10^{10} W/cm^2.

Fig. 4-12 AFM image of DLC film deposited by Nd:YAG laser at 1×10^{11} W/cm^2.
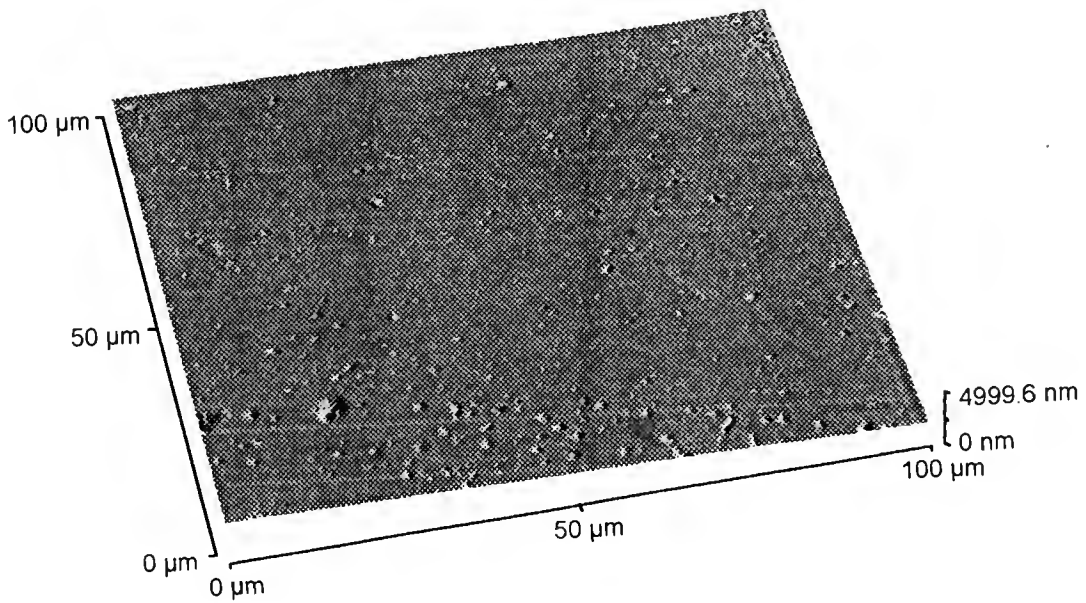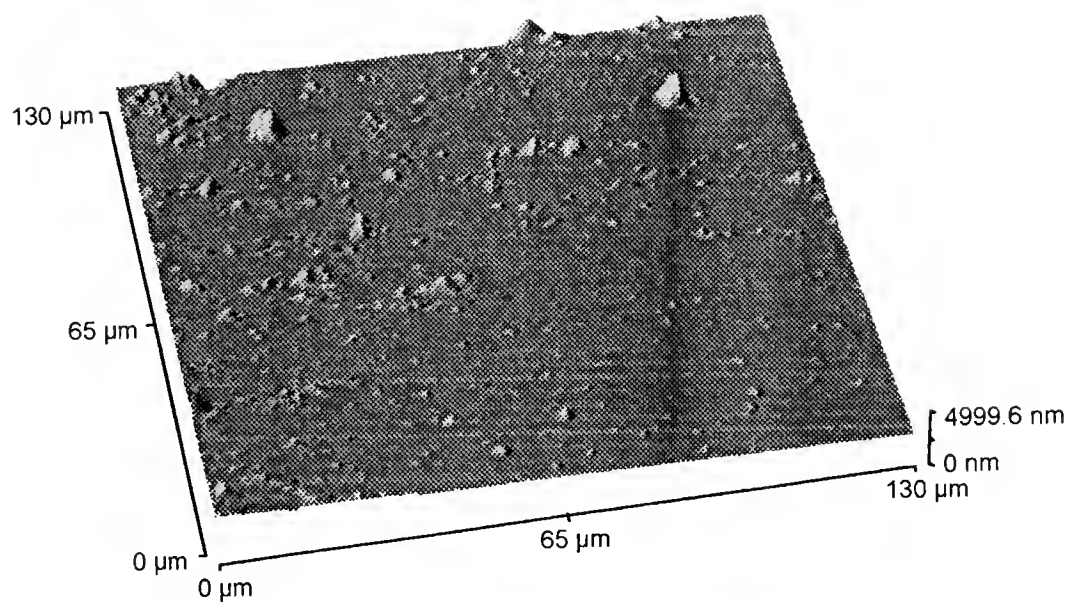
Fig. 4-13 AFM image of DLC film deposited by Nd:YAG laser at 6 x 10^{11} W/cm^2.

Fig. 4-14 AFM image of DLC film deposited by Ti:Sapphire laser at 3 x 10^{14} W/cm^2.
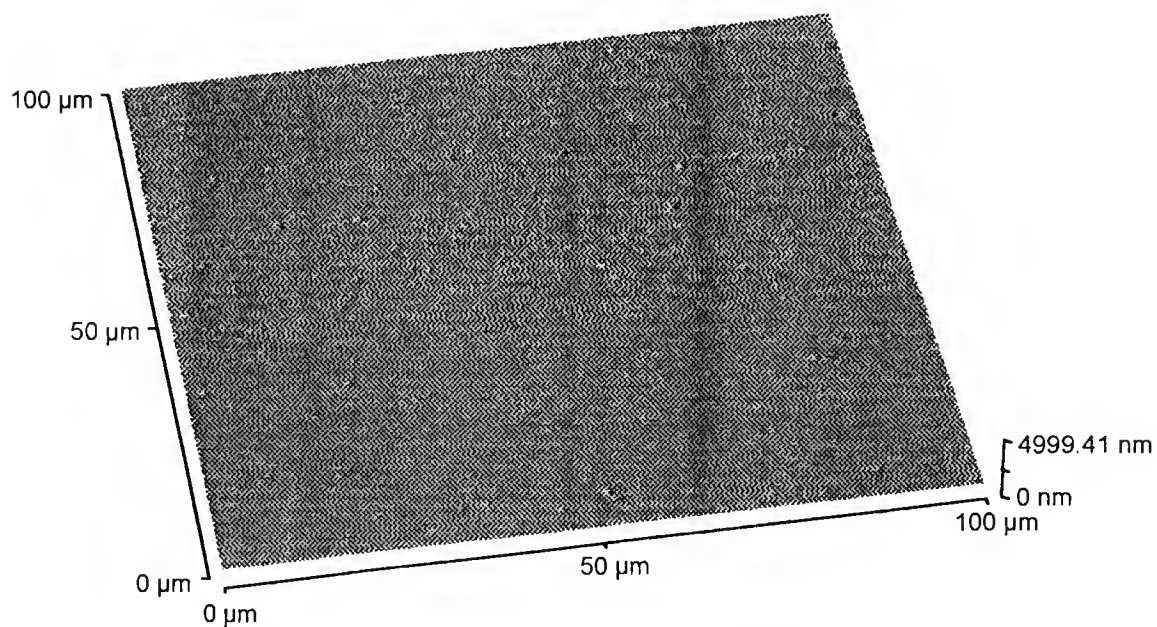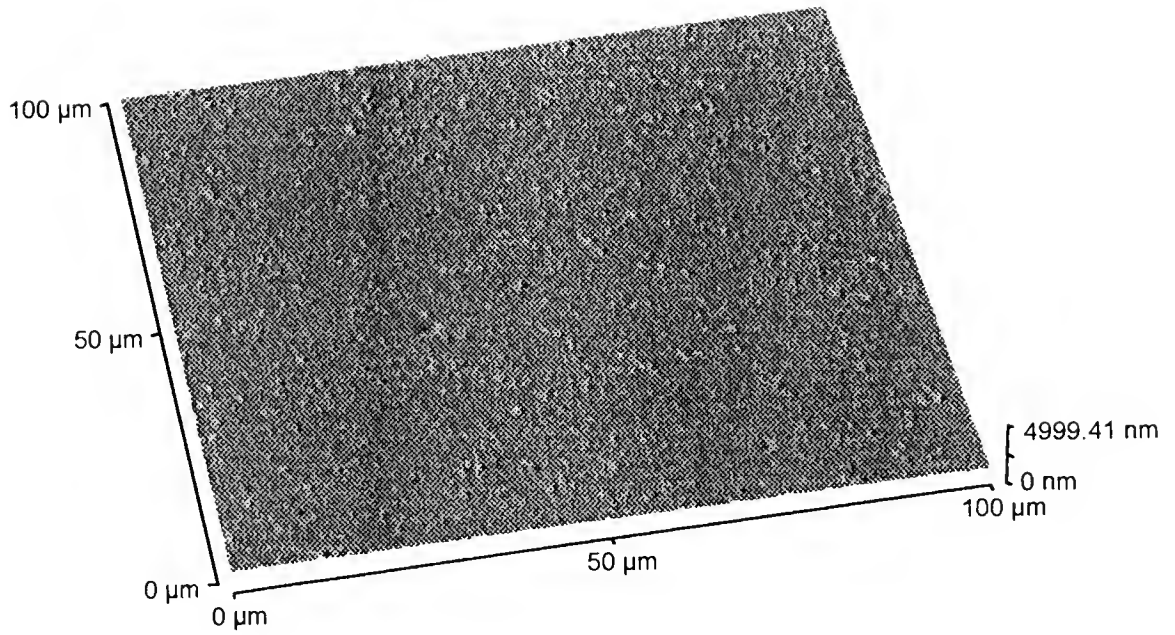
Fig. 4-15 AFM image of DLC film deposited by Ti:Sapphire laser at 1×10^{15} W/cm^2.
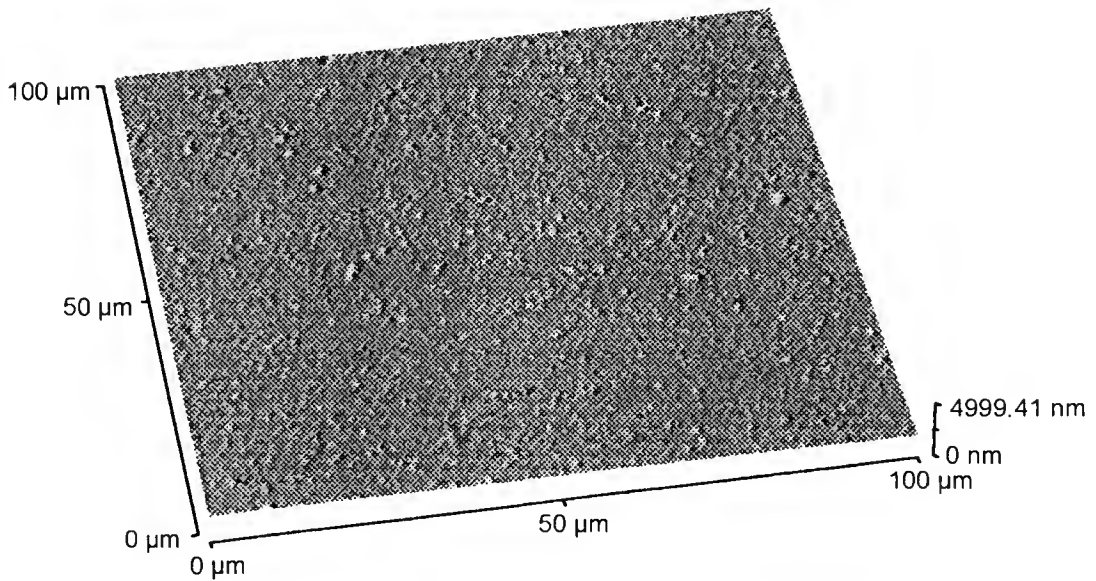

Fig. 4-16 AFM image of DLC film deposited by Ti:Sapphire laser at 6×10^{15} W/cm^2.

was used to study the film topography. When operated in the force sensor mode by applying a constant force on the sensor probe, the SPM is by convention called an atomic force microscope (AFM).

For Nd:YAG laser beam deposited DLC films, Figures 4-11, 4-12, and 4-13 show the AFM images taken at intensities of 3 x 10^{10}, 1 x 10^{11}, and 6 x 10^{11} W/cm^2, respectively. An increase in both the particle size and density as a function of increasing laser intensity is quite obvious on these samples. The as-deposited DLC films went from virtually particle free at 3 x 10^{10} W/cm^2, to a situation where microclusters with diameter up to 5 microns were abundant on the film surface at 6 x 10^{11} W/cm^2. In fact, at high laser energy levels with a tightly focused beam spot, splashing of the microparticles was visually discernible in the laser plasma during deposition. Similar findings were reported by Misra [111], and Chen [112]. Figures 4-14, 4-15, and 4-16 are the AFM images of DLC films deposited on SiO$_2$ substrates by the Ti:Sapphire laser beam, at laser intensities of 3 x 10^{14}, 1 x 10^{15}, and 6 x 10^{15} W/cm^2, respectively. When compared with those deposited by the Nd:YAG beams, these films appeared to have higher particle densities, especially at higher laser intensities, when the entire surface area was covered with micron-sized particles. On the other hand, the average particle size stayed largely unchanged, no large chunks of clustered particles were observed even on samples deposited at the highest intensity of 6 x 10^{15} W/cm^2. Splashing of microparticles was also observed for femtosecond pulse induced plume, when tight focal spots were used. It was also noticed that for both femtosecond and nanosecond laser deposited DLC films, even at constant intensity levels, the surface particle density increased with increasing deposition time.

Variable Angle Spectroscopic Ellipsometry (VASE)

The optical properties of the DLC films deposited on SiO$_2$ substrates were analyzed by a J.A. Woollam Company ellipsometer. Data were collected between 300 and

1000 nm in the variable angle spectroscopic ellipsometry (VASE®) and intensity transmittance modes. The purpose of this experiment was to determine both the film optical properties and its thickness as a function of laser intensity.

The optical properties measured are n and k, the real and imaginary part of the film complex index of refraction. They are alternatively termed as the refractive index and the extinction coefficient, respectively. The complex refractive index describes the optical properties of the DLC film, in terms of how a propagating electromagnetic wave changes its amplitude and phase in it. N and k are related to the complex dielectric constant $\varepsilon = \varepsilon_1 + i\varepsilon_2$ through $\varepsilon_1 = n^2 - k^2$ and $\varepsilon_2 = 2nk$, where the real and imaginary part of the dielectric constant ε_1 and ε_2 can be viewed as how a DLC film will react to an applied electric field.

Ellipsometry measures the polarization state change of a light beam reflected from a sample surface. The measured values are expressed as the ellipsometric parameters psi (ψ) and delta (Δ), which are in turn related to the film property through:

$$\rho = R_p/R_s = \tan(\psi)\exp(i\Delta) \tag{4-1}$$

where R_p and R_s are the complex Fresnel reflection coefficients for the p- and s-polarized light, respectively. Tan(ψ) therefore is the magnitude of the ratio of the p- to s-direction reflection coefficients of the film, and Δ represents the phase difference between these two reflection coefficients.

In the VASE® experiment, a linearly polarized light beam strikes the DLC film surface at an incident angle ϕ and is reflected. The specularly reflected light then passes through a rotating polarizer (called an analyzer) and reaches a silicon photodiode detector. The normalized detector signal can be expressed as a harmonic Fourier series:

$$I_D \propto 1 + \alpha\cos(2A) + \beta\sin(2A) \tag{4-2}$$

here A is the analyzer azimuthal angle with respect to the plane of incidence, α and β are the Fourier coefficients. The ellipsometric parameters ψ and Δ, as well as the Fourier coefficients α and β are related through the equations:

$$\tan(\psi) = \sqrt{\frac{1+\alpha}{1-\alpha}} |\tan P| \tag{4-3}$$

$$\cos(\Delta) = \frac{\beta}{\sqrt{1-\alpha^2}} \frac{\tan P}{|\tan P|} \tag{4-4}$$

where P is the polarizer azimuthal angle. By Fourier transform the detector signal, which is measured as a function of time, the coefficients α and β can be obtained. One can then calculate ψ, Δ, and consequently the optical properties of the film by applying equations (4-3) and (4-4).

The ψ and Δ were measured in our experiment as a function of the incident beam wavelength λ (300 - 1000 nm) as well as the angle of incidence ϕ (65° and 75°). The reason for using a variable angle of incidence is to acquire data at incident angles near the pseudo-Brewster angle, where the measured Δ values are close to 90°, thus providing a more sensitive measurement of the sample. For DLC film and glass substrate, the pseudo-Brewster angle generally falls between 60° and 75°. To prevent the probe light reflected by the substrate backside from reaching the detector and interfering with the signal, we used fused silica substrates with a thickness of 3 mm. They are thick enough to effectively separate the light reflected by the film and that by the backside of the SiO_2 substrate. These SiO_2 substrates are transparent and have well known refractive indices n and extinction coefficients k through out the spectrum range. Knowing the optical constants of the substrate greatly simplified modeling of the acquired ellipsometric data.

The film thickness and its optical constants are inherently related. The correlation is particularly strong between the extinction coefficient k and the film thickness, when semi-absorbing materials such as diamond-like carbon are examined. The VASE® technique by itself is thereby often unable to yield unique solutions for both the film thickness and its optical constants. This problem can be lessened by coupling the VASE® data with the transmission data from the same sample [113].
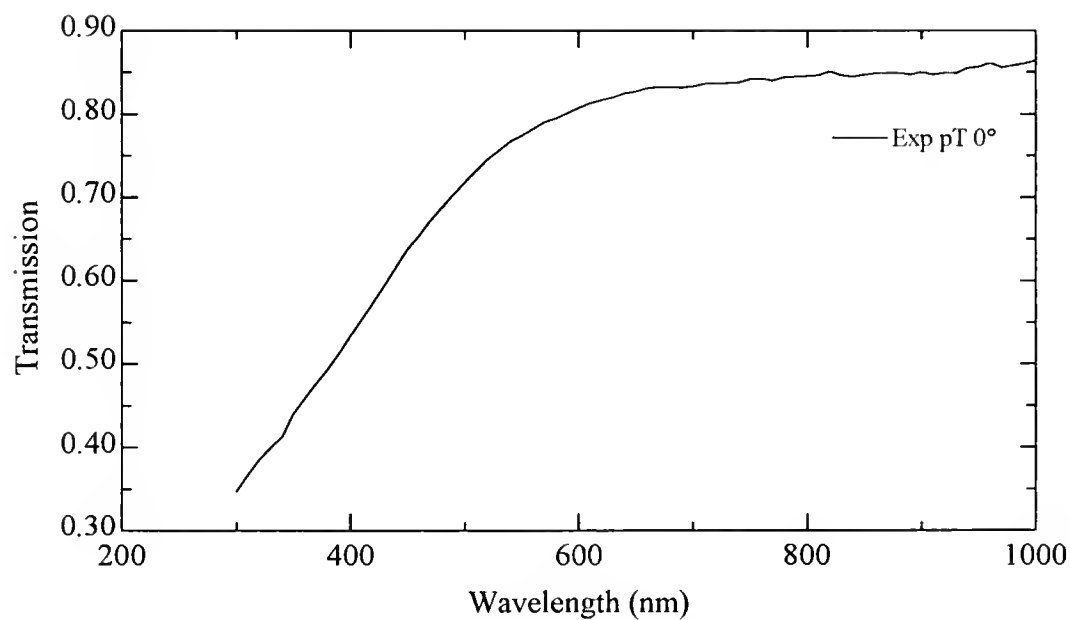
Fig. 4-17 Transmittance of DLC film deposited by Ti:Sapphire laser at 3 x 10^{14} W/cm^2.
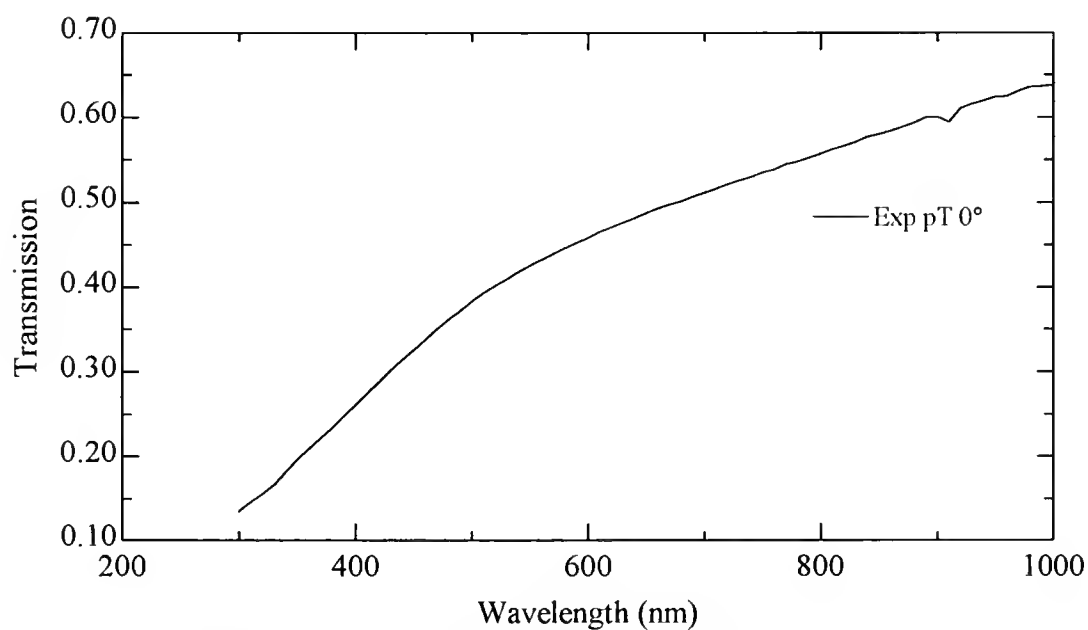

Fig. 4-18 Transmittance of DLC film deposited by Ti:Sapphire laser at 6 x 10^{15} W/cm^2.
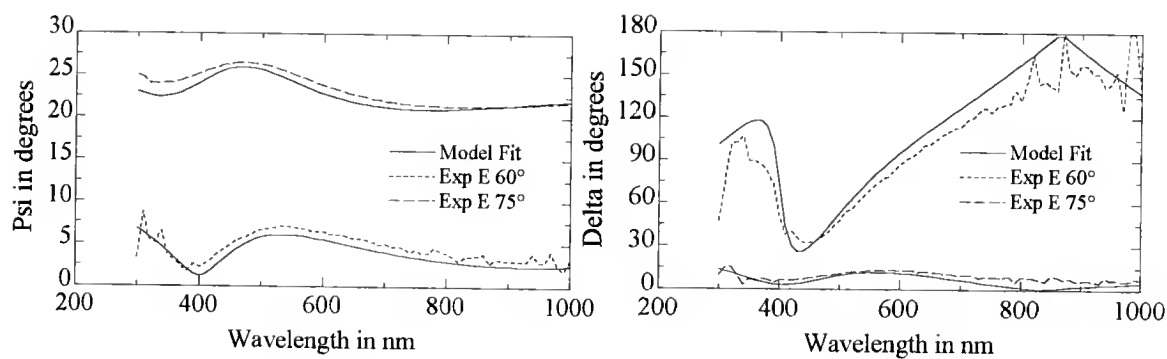
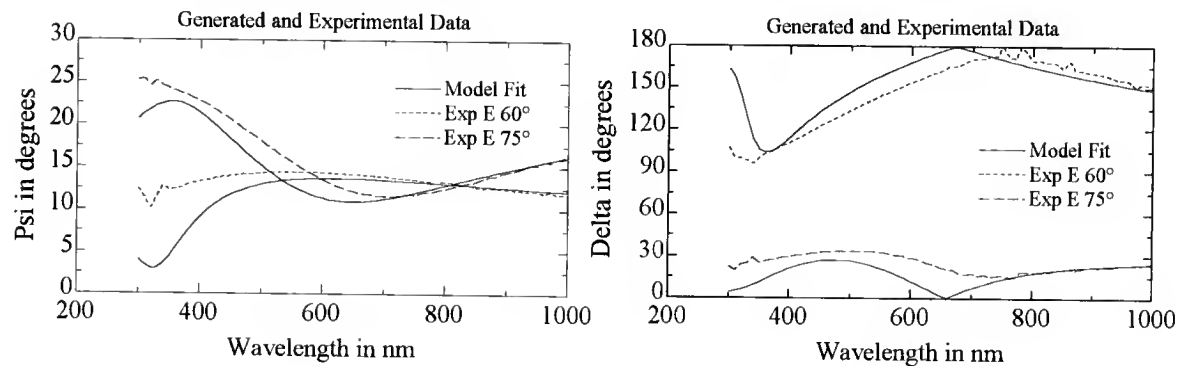Fig. 4-19 Experimental and fitted ψ and Δ for DLC film deposited at 3 x 10^{14} W/cm^2.

Fig. 4-20 Experimental and fitted ψ and Δ for DLC film deposited at 6 x 10^{15} W/cm^2.

Intensity transmittance measurements were carried out by setting the VASE®
ellipsometer in the straight through configuration (ϕ = 90°). A baseline intensity of the
incident beam was first measured without the sample in place. The DLC film
transmittance was then obtained by measuring the beam intensity with the sample in place
and dividing the transmitted intensity by the baseline intensity. The transmittance data
were acquired with a minimum ambient lighting and averaged over 5 cycles of the
analyzer.

Plotted in Figures 4-17 and 4-18 as a function of wavelength, are the transmittance
of DLC samples deposited by the Ti:Sapphire beams, at laser intensities of 3 x 10^{14} and 6 x
10^{15} W/cm^2, respectively.

The DLC film deposited at 3 x 10^{14} W/cm^2 has an optical transparency up to 85%
in the IR region. It is also largely transparent in the visible spectrum down to about 600
nm and becomes more absorbing in the UV range. The film deposited at 6 x 10^{15} W/cm^2,
on the other hand, is much more absorbing with a 65% transparency at 1000 nm
wavelength. At 600 nm, its transmittance is only about half that of the film deposited at 3
x 10^{14} W/cm^2.

Data fitting as well as modeling for the determination of n, k, and film thickness
were carried out with the WVASE32™ software supplied by the J.A. Woollam Company.
This program employs the Levenberg-Matquart regression algorithm, which is a
combination of inverse Hessian and steepest descent algorithms method, to best fit the
measured ellipsometric and transmission data. Data simulation was based on an optical
system consisting of a single DLC layer on a transparent SiO$_2$ substrate. Several function
based models were tried out to fit the ellipsometric and transmittance data, including
Cauchy dispersion, Lorentz oscillator, as well as Parametric semiconductor models. The
best fits were achieved with the Parametric semiconductor model. The addition of film/air
or film/substrate roughness had little effects on improving the fitting results. Shown in
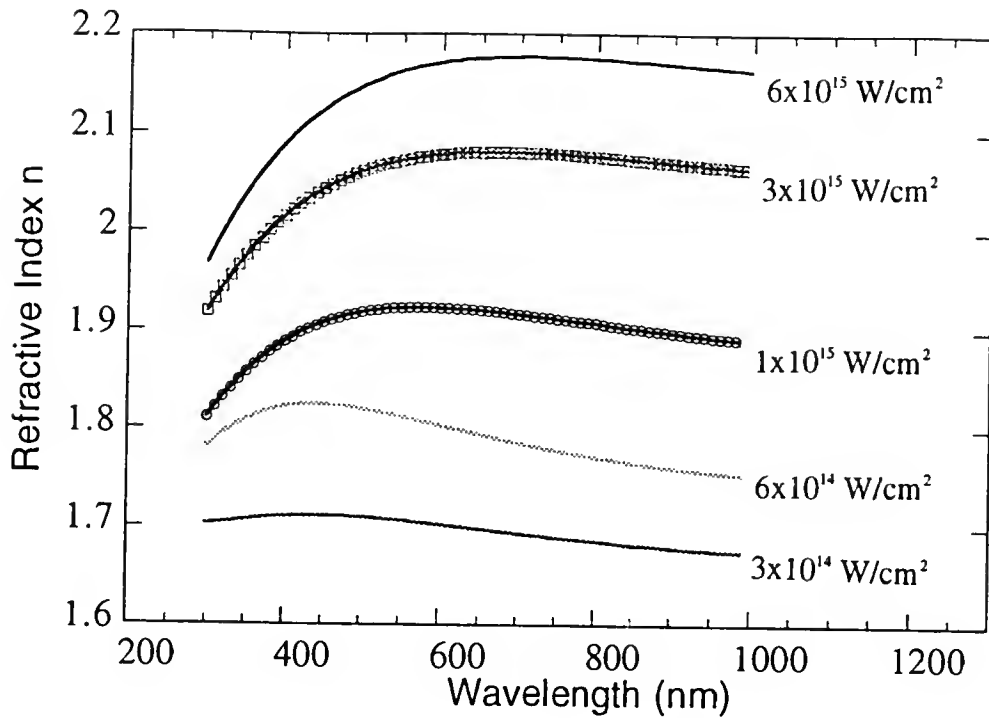Figures 4-19 and 4-20 are the experimental and fitted ψ and Δ data for the DLC films,

Fig. 4-21 Refractive indices n of DLC films deposited by Ti:Sapphire laser, as a function of wavelength.
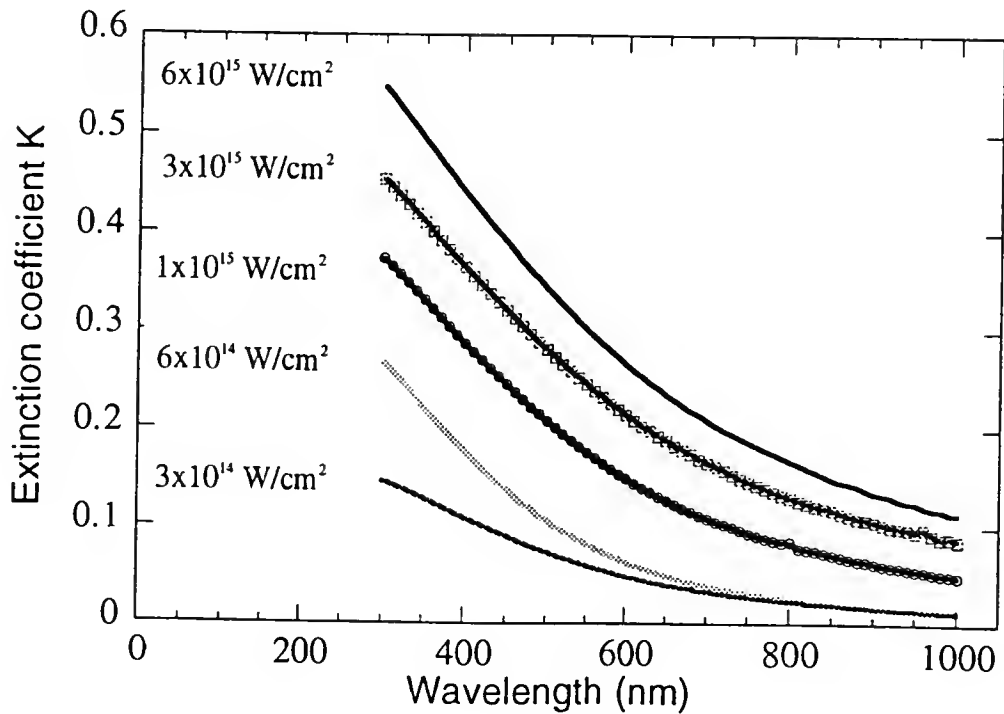

Fig. 4-22 Extinction coefficients k of DLC films deposited by Ti:Sapphire laser, as a function of wavelength.
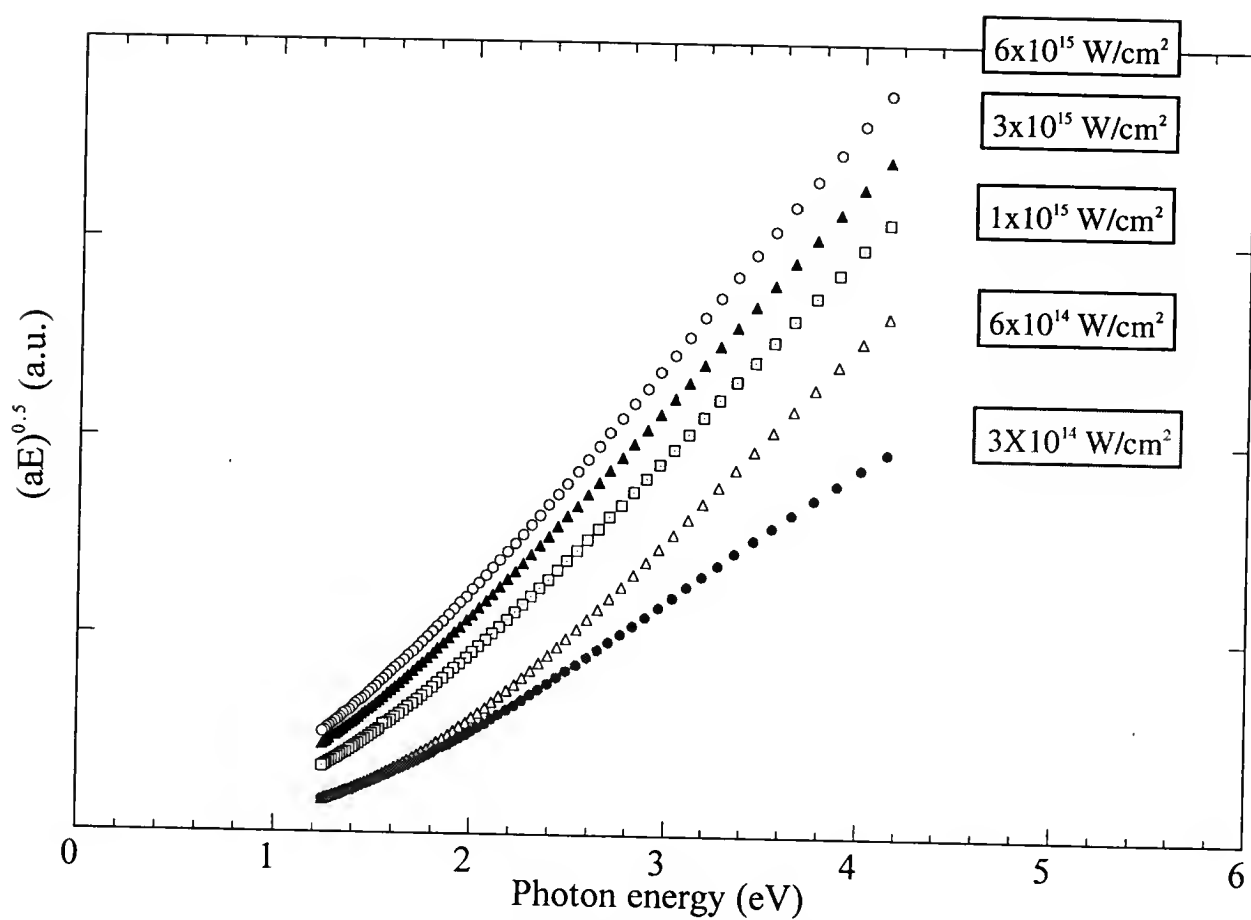
Fig. 4-23 Tauc plot of DLC films deposited by Ti:Sapphire laser.

deposited at laser intensities of 3 x 10^{14} W/cm^2 and 6 x 10^{15} W/cm^2, respectively.

Note that ψ and Δ are better fitted for the DLC film deposited at 3 x 10^{14} W/cm^2, when compared to the one made at 6 x 10^{15} W/cm^2. This is due to the fact that the film is more absorbent at 6 x 10^{15} W/cm^2, as demonstrated by the transmittance measurement in Figure 4-18. This makes model simulations less sensitive to the fitting parameter changes. Deterioration of the fits is especially noticeable at shorter wavelengths in the UV region, where optical absorption is the strongest.

The refractive indices n, and the extinction coefficients k of the DLC films are plotted in Figures 4-21 and 4-22, respectively, as a function of laser intensity.

A rather consistent trend is seen amongst these DLC samples. As the laser intensity increases, the films become more absorbing (higher k) and less refractive (lower n), consistent with the transmittance measurement. For each sample, the film is more transparent in the IR and visible range than in the UV region. Demichelis et al. [114] have demonstrated that it is possible to directly deduce the sp^3/sp^2 ratio of the DLC films from the experimental values of the complex dielectric constants ε_1 and ε_2. Knowing the fact that for DLC films, each sp^2 site gives rise to three σ states and one π state while each sp^3 site has four σ states, they were able to deconvolute the dielectric constants into $\pi \rightarrow \pi^*$ and $\sigma \rightarrow \sigma^*$ contributions in the photon energy range of 1 - 6 eV. This yielded the number of π and σ electrons and hence the sp^3 fraction in the sample. However, the same approach could not be carried out in our ellipsometry study since the maximum photon energy attainable was only about 4 eV.

Depending on film thickness and laser intensity, these DLC films were measured to have electrical resistance ranging from several hundred thousand to several mega-ohms. This put their electrical resistivity between that of the graphite target, which is electrically conducting, and that of the insulating diamond. For amorphous semiconducting materials such as DLC films, the Tauc model [115] is often used to describe their optical bandgaps, where the energy dependency of the absorption coefficient α is expressed as:

$$\alpha\ (E) = \frac{B(E - E_T)^2}{E} \qquad (4\text{-}4)$$

here E is the photon energy, B is a constant, and E_T is the Tauc bandgap. The absorption coefficient α is calculated from $\alpha = 4\pi k/\lambda$, where k is the extinction coefficient and λ the photon wavelength. At photon energies greater than the Tauc bandgap, a plot of the square root of the α times E yields a straight line over a limited range of the spectrum. Tauc bandgap is then obtained by interpolating this line to the photon energy axis. Figure 4-23 is the Tauc plot of DLC films deposited by the Ti:Sapphire pulses, at laser intensities between 3×10^{14} and 6×10^{15} W/cm^2.

Table 6. Thickness and Tauc bandgap of Ti:Sapphire laser deposited DLC films.

Sample	Laser Intensity (W/cm^2)	Thickness (Å)	Tauc Bandgap (eV)
Femto-A	3×10^{14}	1506 ± 10	1.5
Femto-B	6×10^{14}	1242 ± 10	1.3
Femto-C	1×10^{15}	1350 ± 10	1.1
Femto-D	3×10^{15}	811 ± 10	1.0
Femto-E	6×10^{15}	853 ± 10	0.8

Table 7. Thickness and Tauc bandgap of Nd:YAG laser deposited DLC films.

Sample	Laser Intensity (W/cm^2)	Thickness (Å)	Tauc Bandgap (eV)
Nano-A	2×10^{10}	1130 ± 10	2.4
Nano-B	3×10^{11}	936 ± 10	1.4
Nano-C	6×10^{11}	825 ± 10	0.9

As shown in Figure 4-23, the DLC films have Tauc bandgaps ranging from about 1.5 to 0.8 eV, decreasing as a function of increasing laser intensity. Larger optical
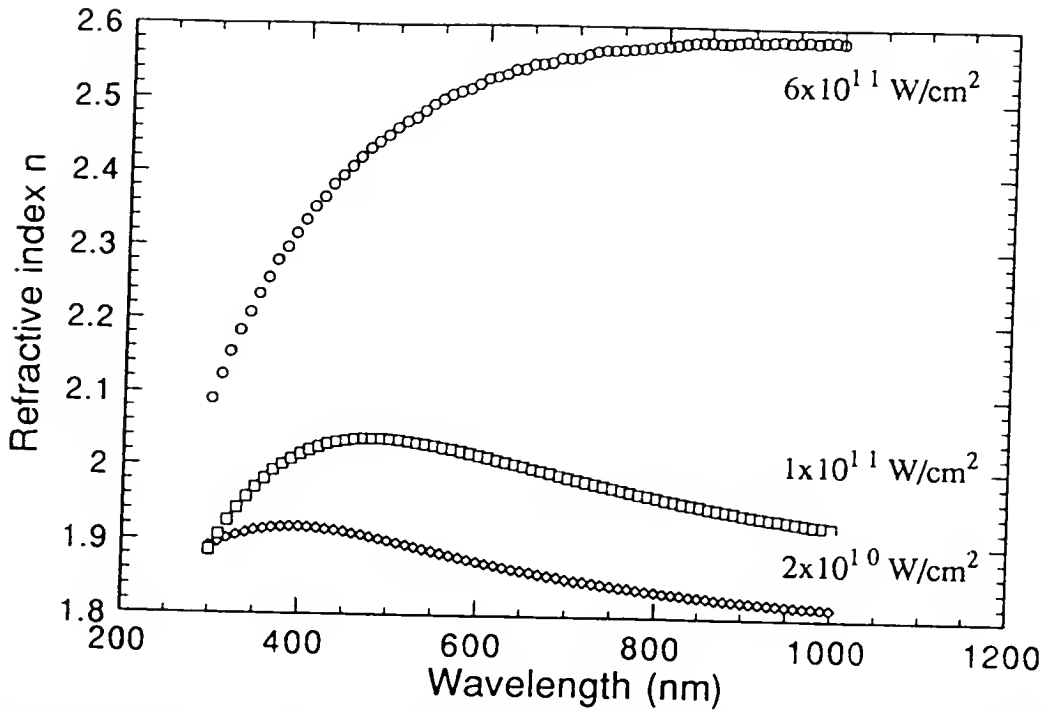
Fig. 4-24 Refractive indices n of DLC films deposited by Nd:YAG laser, as a function of wavelength.
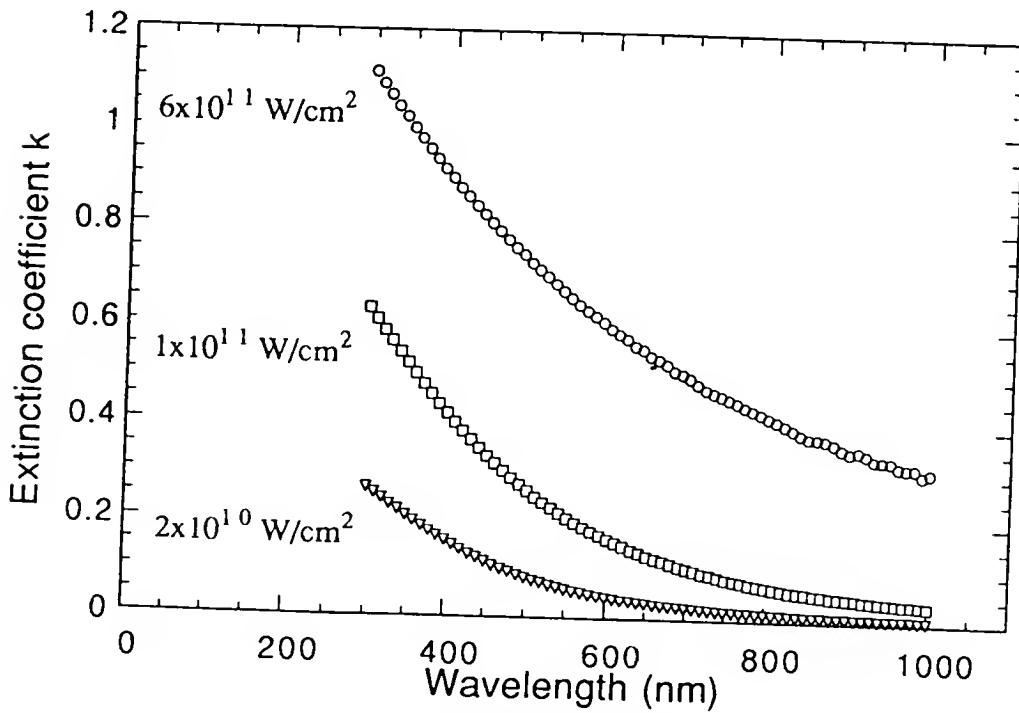

Fig. 4-25 Extinction coefficients k of DLC films deposited by Nd:YAG laser, as a function of wavelength.
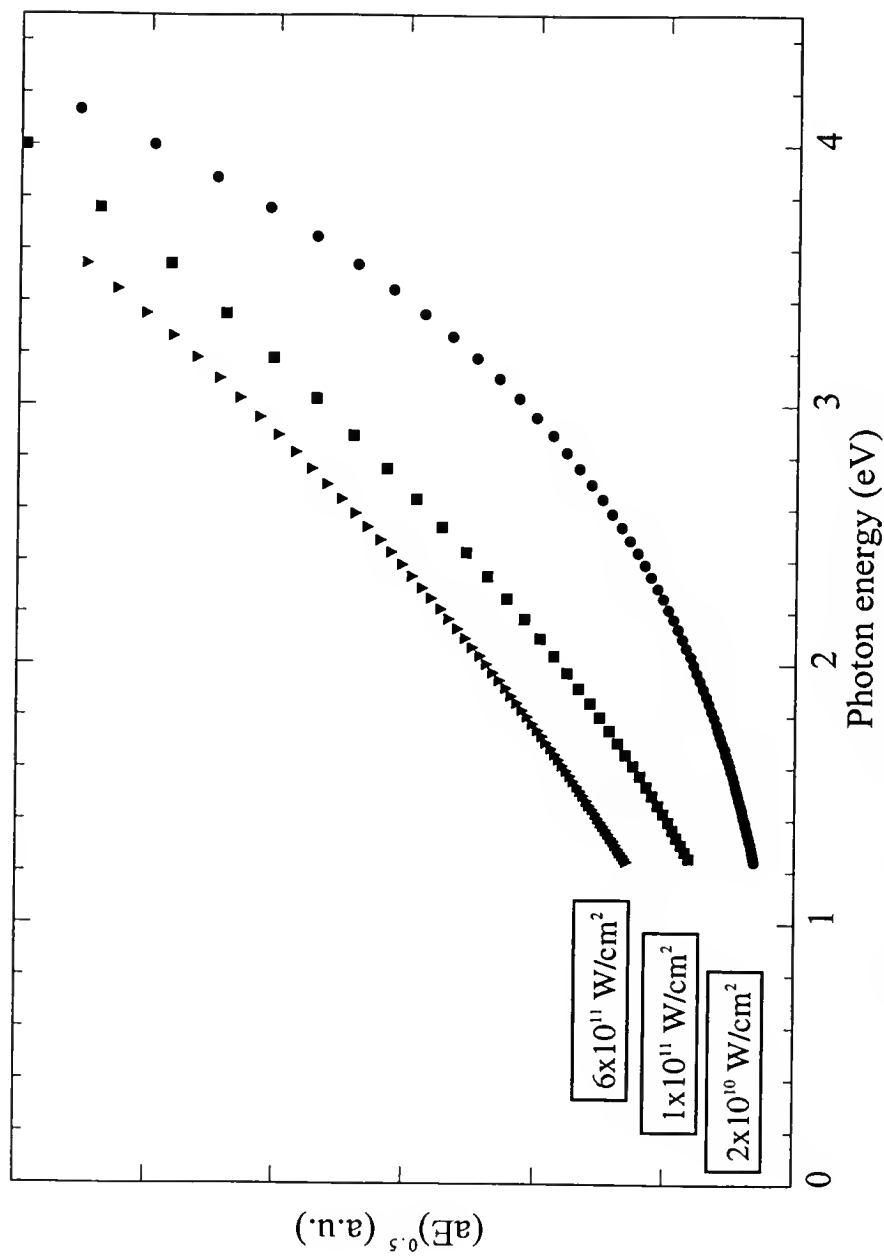
Fig. 4-26 Tauc plot of DLC films deposited by Nd:YAG laser.

bandgaps at lower laser intensities indicate the films are more transparent, consistent with the transmittance measurement. Film thickness and Tauc bandgap of the DLC films are summarized in Table 6. In comparison, the refractive index n, the extinction coefficient k, and Tauc plot of the DLC films deposited by Nd:YAG laser pulses are plotted in Figures 4-24, 4-25, and 4-26, respectively. Their Tauc bandgap and thickness are summarized in Table 7. Similar trends are observed for these samples: lower laser intensities resulted in films that are more transparent and with higher Tauc bandgaps.

The presence of an optical bandgap in amorphous DLC films is significant. The graphite target, with 100% sp^2 bonds is in effect a zero bandgap semiconductor. On the other hand, a single crystal diamond with 100% sp^3 bonds has an optical bandgap of 5.4 eV. It seems that diamond-like carbon, with its mixed sp^3 and sp^2 bonding structure, would have a higher bandgap as the sp^3 bonding content increases. Experimentally, a larger optical bandgap is indeed often found to be associated with a higher percentage of sp^3 bonds in hydrogen-free DLC films. However, the assumption by some that there exists a simple linearity relationship between the film optical bandgap and its sp^3 content is often false. This is because the optical bandgap of DLC depends not only on the relative amount of sp^3/sp^2 bonds, but also their distribution in the film structure.

Robertson [4] has demonstrated that a mere presence of sp^3 sites in amorphous diamond-like carbons was not sufficient to produce an optical bandgap. Instead, the sp^2 sites must be spatially correlated to produce a bandgap even in the presence of sp^3 sites. In other words, unlike most other semiconductors, it appears that the optical bandgap of DLC films depends largely on their degree of medium-range order, rather than just on their short-range order. The bandgap will depend primarily on the concentration and configuration of the sp^2 sites and only indirectly to other factors such as sp^3 or hydrogen content. This is due to the existence of a π orbital associated with each sp^2 bonded carbon atom, in addition to three σ orbitals. The π states are weak bonds that lie closest to the Fermi level. They are therefore responsible for forming both the conduction- and valence-

band states in amorphous DLC films. Opening up a bandgap at Fermi energy will decrease the total π electron energy and thereby stabilize the metastable DLC structure.

In our experiment, for both the Ti:Sapphire and Nd:YAG laser deposited DLC films, their bandgaps showed a tendency to decrease as a function of increasing laser intensity. This can be related to the defect states introduced by the energetic carbon particles. Robertson showed that there existed an inverse correlation between the defect density and the optical bandgap of amorphous DLC films. In a DLC film containing both π and σ bonds, the π defects are expected to be predominant due to their lower creation energy. A higher carbon ion kinetic energy will increase the amount of π defect states in the films, lowering the optical bandgaps of films deposited at higher laser intensities. In the case of Ti:Sapphire laser deposited films, additional σ defects are likely to have been introduced because of the high energy suprathermal ion component found in the laser plasma, thus further decrease the optical bandgap. This may explain the fact that for Ti:Sapphire laser deposited DLC films, the highest Tauc bandgap of 1.5 eV was measured at a laser intensity of 3 x 10^{14} W/cm^2, compared with a value of 2.4 eV for the film deposited at a laser intensity of 2 x 10^{10} W/cm^2 with Nd:YAG pulses. The addition of hydrogen is believed to have the effect of lowering the defect density by increasing the defect creation energy and decreasing their thermodynamic probability, leading to a:C-H films with higher optical bandgaps than that of unhydrogenated ones.

Raman Spectroscopy

Raman spectroscopy, due to its sensitivity to the structural characteristics of materials and its nondestructive nature, is often employed to investigate the details of atomic arrangement and chemical bonding states of thin films.

When a monochromatic incident beam with frequency v_o impinges on the sample, a scattered line at the same frequency v_o is observed in the spectrum. This line is known as

the Rayleigh line. In addition, a series of weaker lines at both lower and higher frequencies are also present. These shifted lines are the so-called Raman bands. The Raman bands occurring at frequencies higher than v_o are referred to as the anti-Stokes scattering (photon acquires a quantum of vibrational energy) while those with frequencies lower than v_o are called Stokes scattering (photon losses a quantum of vibrational energy). The significance of these Raman bands is that their separation Δv from the Rayleigh line v_o is a direct measurement of the vibrational and/or rotational frequencies of the sample under examination. Because anti-Stokes scattering has a much lower intensity and its magnitude depends strongly on sample temperature, only Stokes scattering is taken in a regular Raman spectroscopy.

Raman scattering is a very weak event. Rayleigh scattering from optically transparent samples is on the order of 10^{-3} - 10^{-5} that of the exciting line, whereas Raman scattering is only on the order of one millionth to one billionth that of the incident beam. In a normal Raman experiment, the wavelength of the incident light is usually in the visible range and thereby much greater than any vibrational frequency of the sample molecules. Only the mobile electrons are perturbed by the incident electromagnetic field, whereas the nuclei are too heavy to be effected by the radiation field. This is especially helpful when studying sensitive information such as the chemical bonding states of the molecules.

In our experiment, Raman spectra were taken from the same DLC samples examined with the VASE® technique. The Raman spectrometer used in our study is a Kaiser Optical System, Inc. HoloProbe spectrometer. This spectrometer consists of an imaging spectrograph integrated with a fiber-optic probe head, an Olympus BX60 microscope, a charge-coupled device (CCD) camera, and various compact laser components. Figure 4-27 is the layout of the Holoprobe Raman spectrometer. It has a spectral resolution better than 5 cm^{-1}.

The laser source used in this spectrometer is a 532 nm diode-pumped, frequency-doubled Nd:YAG laser. The green light maximizes the sensitivity of the system. The
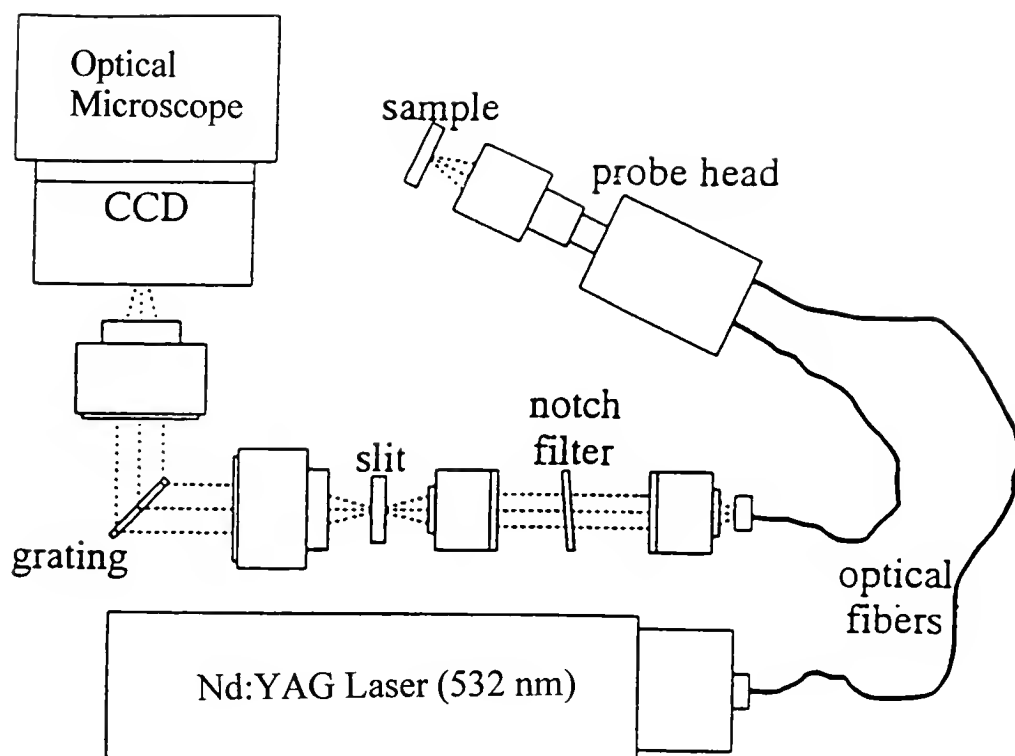
Fig. 4-27 Schematic of the Raman spectrometer [116].

system's imaging spectrograph is equipped with a HoloPlex^{TM} grating and placed in the axial-transmissive spectrograph configuration [116]. This compact design provides spectral coverage up to 4500 cm^{-1} in one single exposure. In comparison, a conventional 1/4- to 1/2-meter Czerny-Turner based Raman spectrometer, which relies on multiple exposure to cover the entire Raman spectrum, may take up to several hours to collect the a similar spectrum.

The Raman spectra were taken with a laser power of 11 mW measured on the film surface. The probe beam diameter was determined to be ~16 μm with a 50X objective lens. Spectra acquisition time was set to be 10 seconds. With the cosmic light filter on, actual acquisition time doubled to 20 seconds.

Fig. 4-28 Raman spectrum of DLC film deposited by Ti:Sapphire laser at 6×10^{14} W/cm^2.

Fig. 4-29 Raman spectrum of DLC film deposited by Ti:Sapphire laser at 1×10^{15} W/cm^2.

Fig. 4-30 Raman spectrum of DLC film deposited by Ti:Sapphire laser at 3×10^{15} W/cm^2.
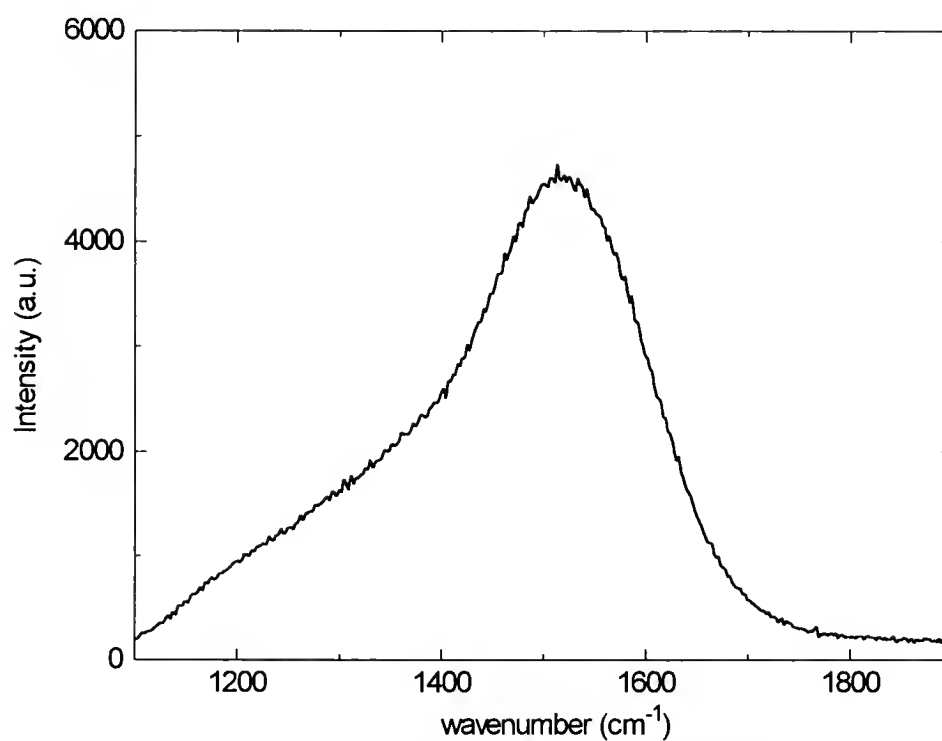
Fig. 4-31 Raman spectrum of DLC film deposited by Ti:Sapphire laser at 6×10^{15} W/cm^2.

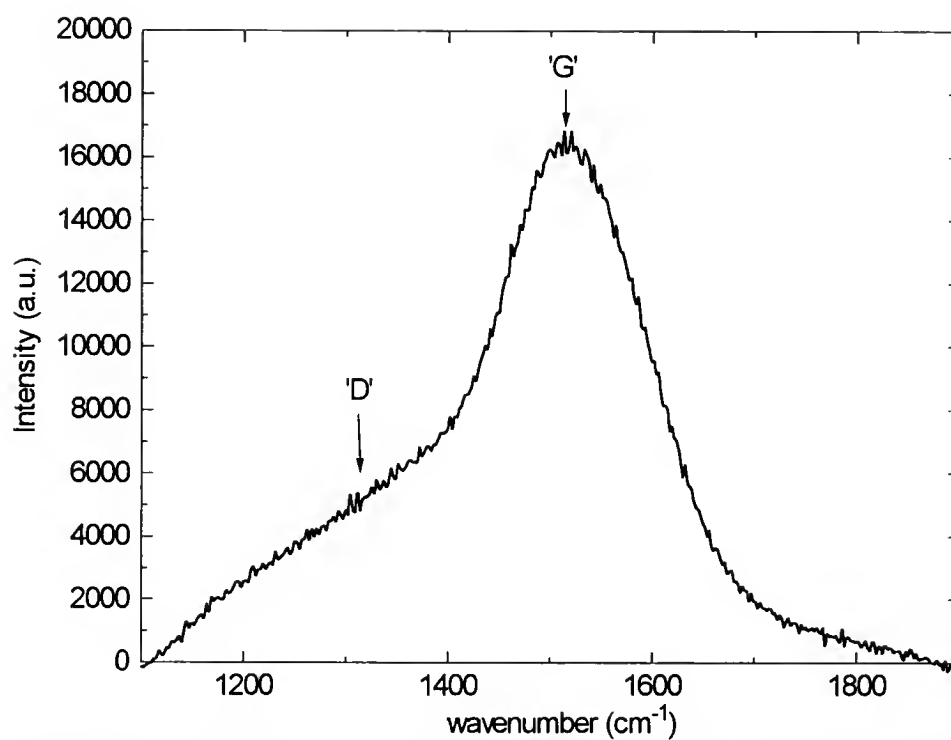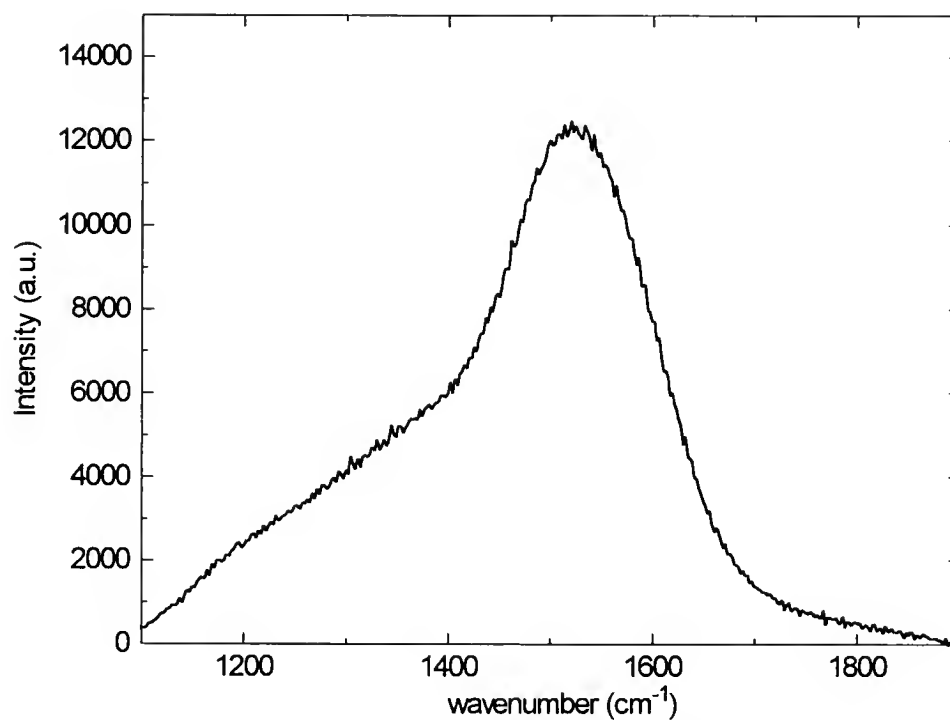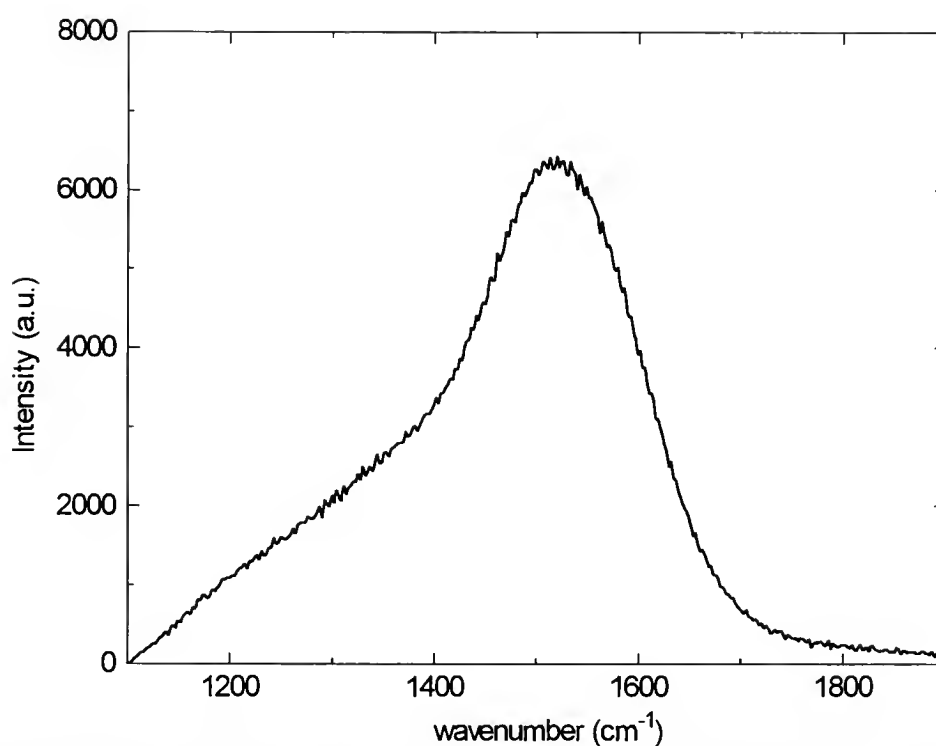Fig. 4-32 Raman spectra of the graphite target and a CVD diamond film.

Fig. 4-33 Raman spectrum of graphitized DLC film deposited by Ti:Sapphire laser at 1 x 10^{15} W/cm^2.

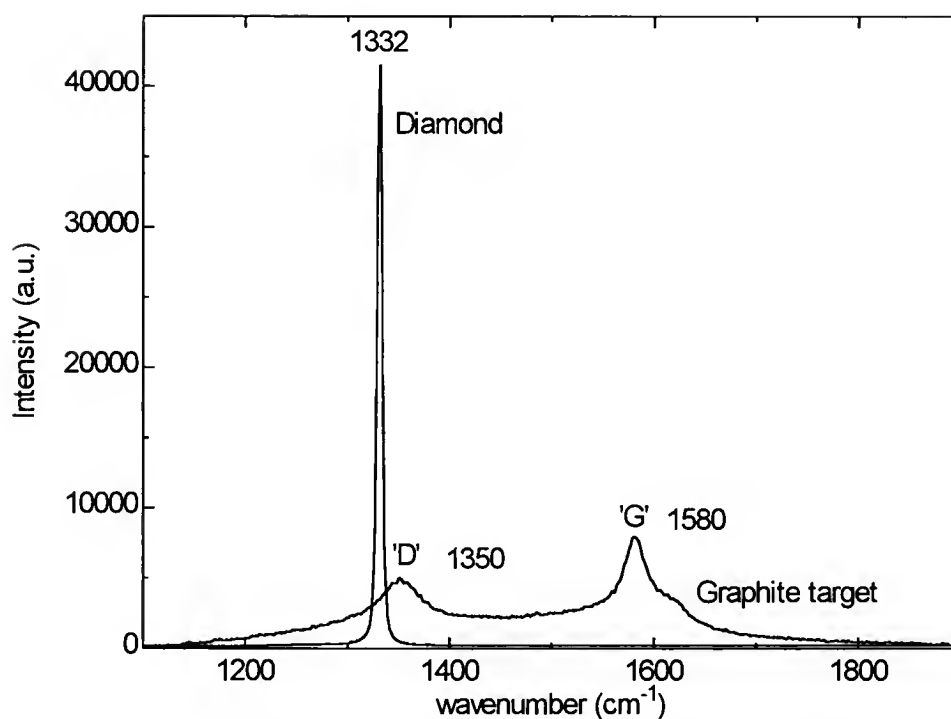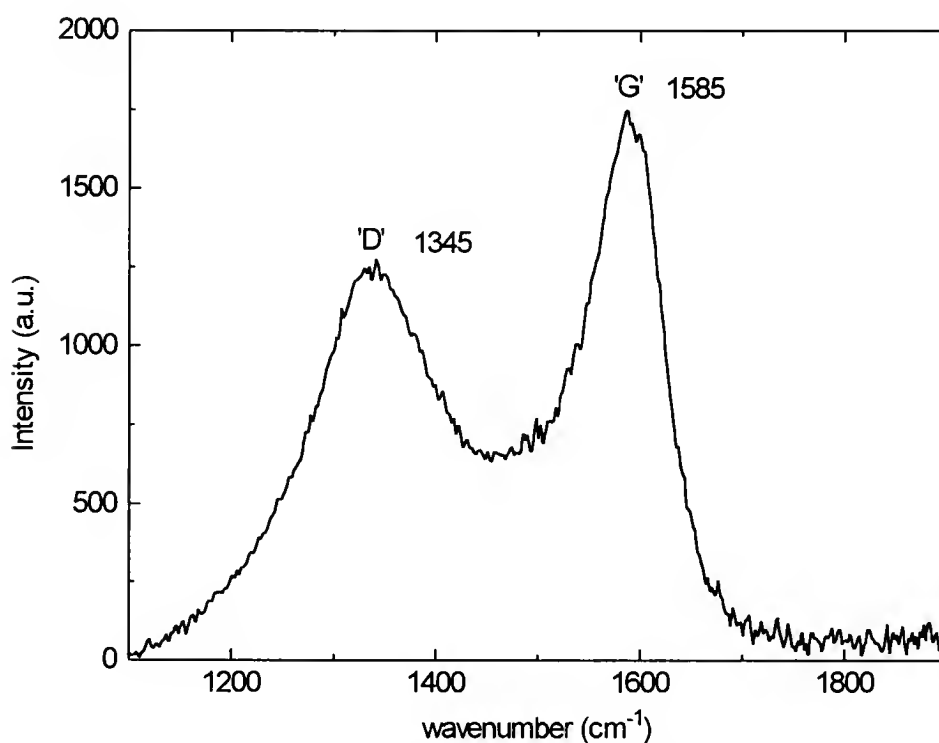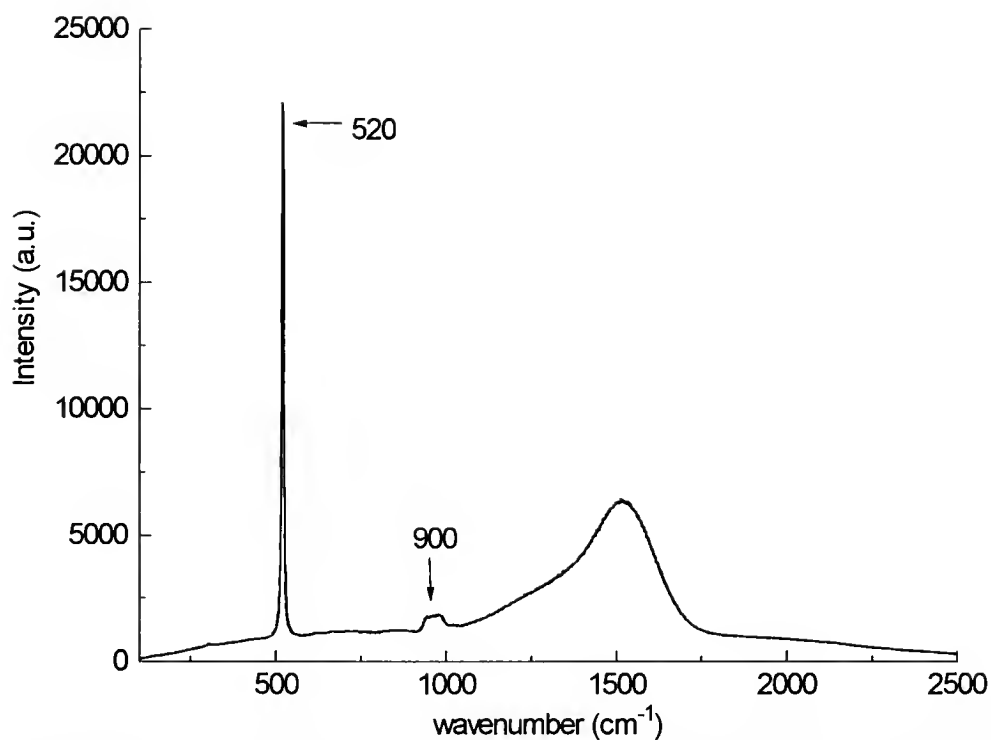Fig. 4-34 Raman spectrum of DLC film deposited by Ti:Sapphire laser on Si substrate at 1×10^{15} W/cm^2.
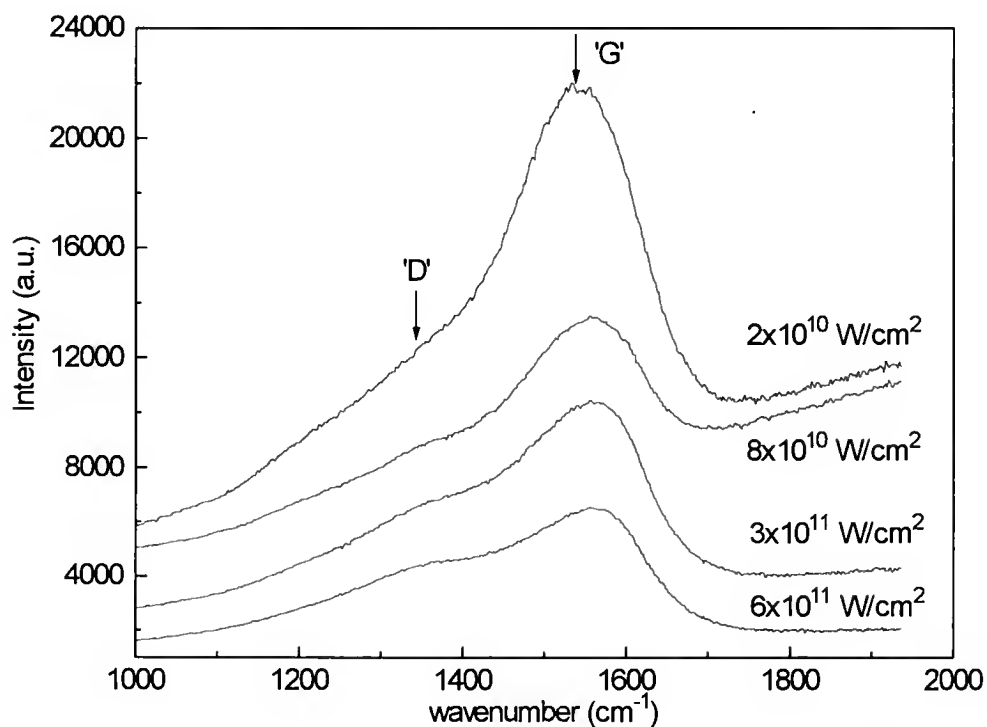

Fig. 4-35 Raman spectra of DLC films deposited by Nd:YAG laser at various intensities.

Shown in Figures 4-28 through 4-31 are the Raman spectra taken from DLC samples deposited on SiO_2 substrates by the Ti:Sapphire laser, at intensities ranging from 6 x 10^{14} to 6 x 10^{15} W/cm². The DLC film deposited at 3 x 10^{14} W/cm² was found to be very photosensitive. The resulting fluorescence created strong background signals that largely smeared out the expected features in the Raman spectrum. Surface contaminant is believed to be responsible for the fluorescence observed on this sample. Increasing the acquisition time did not appear to have alleviated the problem. Fluorescence occurs when the incident light frequency ν_o coincides with an absorption frequency of the contaminant molecule. It is a time dependent event where the incident photon is actually absorbed by the molecule, which is excited to a higher energy state and then relaxes back to the ground state with a well defined lifetime. Fluorescence, however, is not to be confused with the Raman scattering phenomenon called "resonant Raman scattering" (RRS). RRS occurs only when the incident light frequency ν_o approaches an electronic absorption of the sample molecule. Instead of a noisy background, RRS should give rise to enhanced signals characteristic of the sample molecule. Also, from a theoretical point of view, in RRS the absorption and emission of the photon are two simultaneous events and can not be separated in time.

In comparison, the Raman spectra taken from the graphite target and a free standing CVD diamond film are plotted in Figure 4-32. Diamond belongs to FCC lattice structure with space group Fd3m. The two carbon atoms in the primitive unit cell comprise a single triply degenerate first order phonon with symmetry T_{2g}. From the factor group O_h selection rules, this mode is Raman active and leads to a single sharp line at 1332 cm^{-1} [117] as shown in Figure 4-32. On the other hand, the graphite target displayed two well defined Raman bands centered at 1350 cm^{-1} and 1580 cm^{-1}, respectively. The 1580 cm^{-1} band is by convention called the "G" band. It is predicted from the D_{6h} factor group as the first order E_{2g} mode, resulting from in-plane C-C stretching vibration. The 1350 cm^{-1} peak, which is generally termed as the "D" band ("D" as in disordered), can be

assigned to the A_{1g} mode activated by the disorder associated with a finite graphite crystalline size. The D peak bandwidth is believed to be inversely related to the effective sp^2 cluster size in the graphite material [118]. The existence of the D band in a graphitic material is a result of relaxation of the wave-vector k selection rule: when the long-range translational symmetry is lost in a disordered material such as amorphous or polycrystalline graphite, crystal moment no longer needs be conserved, thus any k vector in the Brillouin zone may contribute to additional lines in the Raman spectrum.

The Raman spectral features of the DLC films are distinctively different from that of the CVD diamond and the graphite target. Instead of well defined D and G peaks, these DLC samples exhibited a broad band structure covering the spectrum ranging from about 1000 to 2000 cm^{-1}. This broad band can be interpreted as a convolution of the two-component structure of a microcrystalline graphite: a relatively narrow G band centered at around 1550 cm^{-1} and a much broader D shoulder embedded at a lower wavenumber.

When compared with one another, the Raman spectra from DLC films deposited at very different laser intensities are observed to be rather similar. Their G and D bandwidth and peak position do not appear to vary much from one sample to another. A common practice in analyzing the small differences amongst these spectra is to mathematically fit them with two damped harmonic oscillator functions [119]:

$$\frac{dI}{d\omega} = \frac{\Gamma\omega_0}{[(\omega_0^2 - \omega^2)^2 + 4\Gamma\omega_0^2\omega^2]} \tag{4-6}$$

where dI/dω is proportional to the detector signal at ω, ω_0 is the undamped mode frequency, ω is the frequency shift from the laser line, and Γ is the damping constant. An integration of the above equation gives the intensity I associated with each Raman band.

In our analysis, the Raman spectra were fitted in the spectral range between 1200 and 1800 cm^{-1}. Taking background signal into consideration, a linear function was added as a third variable during the fitting process, in addition to the two harmonic oscillator

functions.

Summarized in Table 8 are the parametric values used in fitting the Raman spectra, including peak center position for the G and D bands, as well as their respective full-width-half-maximum (FWHM).

Table 8. Fitted Raman parameters of Ti:Sapphire laser deposited DLC films.

Sample	Laser Intensity (W/cm^2)	G band (cm^{-1})		D band (cm^{-1})	
		Center	FWHM	Center	FWHM
Femto-A	3×10^{14} (Fluorescence)	-	-	-	-
Femto-B	6×10^{14}	1520	181	1321	150
Femto-C	1×10^{15}	1527	177	1327	215
Femto-D	3×10^{15}	1528	185	1325	270
Femto-E	6×10^{15}	1530	183	1342	340
Accuracy	-	±1	±3	±5	±10

When compared with the graphite target, the G band of every DLC sample was observed to have shifted from 1580 cm^{-1} down to the 1520 - 1530 cm^{-1} range. As the laser intensity increased from 6×10^{14} to 6×10^{15} W/cm^2, the G bands showed a slight upward shift, but their bandwidths (FWHM) did not exhibit a well defined trend and remained largely unchanged. On the other hand, the D bandwidths (FWHM) displayed a clear upward drift as a function of increasing laser intensity, their values more than doubled from 150 cm^{-1} to 340 cm^{-1} as the laser intensity was increased from 6×10^{14} to 6×10^{15} W/cm^2. The D band center did not have a well-defined correlation with the laser intensity either, though they also appeared to have downshifted to lower wavenumbers (1321 - 1343 cm^{-1}) when compared with that of the graphite D band at 1345 cm^{-1}.

Using computer simulated Raman and vibrational density-of-states (DOC) spectra, Beeman et al. [120] showed that a downshift of the graphite G band from 1580 cm^{-1} to lower wavenumbers in DLC films is a result of bond-angle distortion, as well as a decrease in the average bond angle of the sp^2 sites. They also suggested that a further downshift of the Raman G band is possible with the addition of four-coordinated sp^3 bonds in a DLC film, and the amount of this downshift is roughly proportional to the percentage of sp^3 bonds added to the model. Dillon's results [119] also indicated a similar downward trend of the G band as a result of the bond-angle disorder. The relationship between the D band center position and that of the DLC structure is less well established. Though both Dillon [119] and Beeman [120] have suggested a possible D band downshift as a result of increasing sp^3 content and/or bond-angle distortion, their observation has been rebuted by recent experiments [31].

The G band downshifting from that of the graphite target, which was observed in our Raman study, has confirmed the notion that there exists a certain amount of sp^3 bonds as well as a certain degree of bond-angle distortion in these DLC films. It is also tempting to suggest that the films deposited at lower laser intensities have higher sp^3 fractions, in light that their G bands are centered at lower wavenumbers and they have higher optical bandgaps measured from our ellipsometry experiments. However, we have to be cautious because the effects of sp^3 content and bond-angle disorder on the G band downshift may not be easily differentiated, considering the fact that the existence of bond-angle distortion and sp^3 bonds in a DLC film are often correlated. In addition, it has been demonstrated that Raman band shift could be introduced as a result of residual stress in the DLC films [117]. Our TOF and ellipsometry measurements have indicated that the DLC films are condensed from carbon particles with very different kinetic energy and they have unequal film thickness, which could give rise to various compressive stress at the film/substrate interface. This residual stress can not be easily relaxed because of the rigid SiO$_2$ substrate. Thereby the Raman band shift resulting from residual stress and that from the change of

structure disorder in the films are often not separable.

Another conclusion that can be drawn from our Raman study is that the DLC films have a higher degree of bond-angle distortion at higher laser intensity levels. As higher particle energies associated with higher laser intensities would likely lead to a higher degree of disorder in the film structure. This is consistent with the study of Enke [121], who found a direct relationship between the D bandwidth and that of the film bond-angle distortion.

As mentioned earlier, the D band center position did not exhibit a clear correlation with the laser intensity. In addition to possible complications caused by the presence of residual stress, we believe some of the artifacts associated with the fitting process may have played a role. These include selection of the fitting range, background intensity treatment, and the choice of oscillating functions, all of which are to some degree user dependent. Thereby for DLC films, which do not have well defined vibrational/translational peaks, Raman spectroscopy can at best be treated as a semi-quantitative analytical tool.

Sinha et al. [122] also observed that DLC films made from different techniques and with very different sp^3/sp^2 ratios seemed to have rather similar Raman features. This can be explained by the fact that sp^2 bonds, with a Raman scattering cross section of $500 \times 10^{-7} cm^{-1} sr^{-1}$, are as much as 50 times stronger Raman scatters than the sp^3 bonds [123]. As a result, the Raman spectrum will be most sensitive to the presence of sp^2 bonds in a DLC film, even when they only constitute a relatively small fraction of the total bonding sites.

It has been found that at room temperature, the D band appeared only as a largely buried "shoulder" along side the dominant G band, but it reemerged as a well defined peak after annealing at higher substrate temperatures [30-32]. By increasing the probe beam power from 11 mW to 50 mW on the film surface, we were able to induce similar annealing effects. This is because with increasingly larger amount of laser energy being pumped to a tightly focused spot of ~16 μm, the DLC film, which is a relatively poor

thermal conductor, would not be able to sufficiently dissipate the excessive heat into the surrounding area. As a result, a thermal graphitization process was effectively introduced into the film. The graphitized area appeared as a burned spot under the optical microscope.

Shown in Figure 4-33 is the Raman spectrum taken from a DLC film deposited at 1×10^{15} W/cm^2 after graphitization. Two well defined G and D bands centered at around 1585 cm^{-1} and 1345 cm^{-1}, respectively, can once again been seen in the spectrum.

Figure 4-34 displays the Raman spectrum taken from a DLC film deposited at 1×10^{15} W/cm^2 on Si substrate, with a thickness of ~500 Å. The first order Oτ phonon line at 520 cm^{-1} and the second order 2TO peak centered at ~900 cm^{-1} from the silicon substrate are clearly visible. This observation supports the transmittance measurements that the DLC film is largely transparent in the visible wavelength of 532 nm.

Table 9. Fitted Raman parameters of Nd:YAG laser deposited DLC films.

Sample	Laser Intensity (W/cm^2)	G band (cm^{-1})		D band (cm^{-1})	
		Center	FWHM	Center	FWHM
Nano-A	2×10^{10}	1545	150	1383	184
Nano-B	8×10^{10}	1554	140	1402	203
Nano-C	3×10^{11}	1562	145	1400	230
Nano-D	6×10^{11}	1561	147	1384	313
Accuracy	-	±1	±3	±5	±10

Figure 4-35 shows the Raman spectra taken from the DLC films deposited with the Nd:YAG pulses, at laser intensities ranging from 2×10^{10} to 6×10^{11} W/cm^2. Similar to those deposited with the Ti:Sapphire pulses, their G bands were found to have downshifted from 1580 cm^{-1} to the 1545 - 1562 cm^{-1} range, and their D bandwidths

broadened as a function of increasing laser intensity. Again, no well-defined pattern was observed for either the G bandwidth or the D band center position. Table 9 summarizes the parametric values used in fitting the Raman spectra.

Electron Energy Loss Spectroscopy (EELS)

Analytical techniques such as Raman spectroscopy and ellipsometry, along with others such as electrical resistivity and microhardness measurements, can give a factual description of the diamond-like characteristics of DLC films. But the ultimate determination of how diamond-like these films are requires a direct, quantitative measurement of the sp^3 fraction. Because laser deposited DLC films are amorphous and hydrogen-free, few techniques have proven to be effective in quantifying the sp^3 content. One approach often taken is to extract the DLC film density, either through X-ray specular reflectometry (XRR) or Rutherford backscattering spectroscopy (RBS), and then compare it with respect to that of graphite and diamond. However, experiments have shown that more often than not, a simple linear proportionality relationship between the film density and its sp^3 content does not apply for DLC films. For example, large changes in film density were found to have been induced by a relatively small amount of sp^3 bonding increment, leading to an overestimate of the sp^3 fraction [43]. On the other hand, Beeman et al. [120] have pointed out that though a DLC film with a near 100% sp^3 bonding structure would have a density value very close to that of diamond, it is also possible for a DLC film with roughly 50% sp^3 content to have a density less than 2.8 g/cm^3, which is halfway between 2.2 g/cm^3 for graphite and 3.5 g/cm^3 for diamond. This could happen if a less homogeneous distribution of three and four-coordinated carbon atoms exists, thus giving rise to an underestimate of the sp^3 fraction. In light of the above discussion, we elected to use electron energy loss spectroscopy (EELS) in our study to quantify the sp^3 content.

EELS is most commonly operated in the transmission mode by directing a monoenergetic electron beam through a thin film specimen. The incident electrons lose a specific amount of energy as a result of the collisions between them and the sample nuclei and inner shell electrons. The measured energy loss can then be used to identify the local elemental concentration and bonding structure of each sample species present.

There are three regions in a complete EELS spectrum: zero-loss, low-loss, and core-loss. The zero-loss peak represents those incident electrons that have undergone elastic or negligible inelastic scattering through the sample specimen. This peak itself does not reveal any information about the sample bonding information, but it is often useful in system calibration. The low-loss region extends from about 1 to 50 eV by convention. The spectral features in this regime are related to inelastic scattering between the incident electrons and the sample valence electrons. The core-loss region sees a series of "edges" arising from inelastic scattering between the incident electrons and the core level electrons. The characteristic edge shapes are results of the excitation of electrons from discrete inner shell levels into states above the Fermi level. They reflect the empty density of states above the Fermi level for each sample species. These edges are commonly referred to as the K, L, M edges and so forth, similar to those nomenclatures used in X-ray absorption spectroscopy. One can identify the sample atom responsible for the signal by measuring the threshold energy of each edge. Furthermore, the net integrated signal for the specific edge can be used to calculate the number of atoms responsible for the signal. This institutes the basis for quantitative compositional EELS analysis [124]. Due to sample preparation restrictions, this technique provides information on a more localized scale.

A Gatan electron energy loss spectrometer, attached as an auxiliary to a field-emission analytical TEM, was used in our experiment. It has a maximum resolution of ~ 0.5 eV, defined by the FWHM of the zero loss peak. Carbon K-shell edge spectra were taken between 280 - 320 eV at an accelerating voltage of 150 keV. EELS samples were prepared by first depositing DLC films onto cleaved sodium chloride (NaCl) crystals, they

were then floated off in deionized water onto 300-mesh copper grids. Film thickness was controlled to be less than 700 Å to alleviate the effects of multiple scattering. Multiple scattering is the most important limitation to EELS analysis, as it will result in a decrease of the edge to background ratio, thus effectively smearing out any details in the spectrum.

Two DLC samples made by the femtosecond Ti:Sapphire pulses have been analyzed by EELS. They were deposited at laser intensities of 3 x 10^{14} and 5 x 10^{15} W/cm^2, respectively. Figure 4-36 is the K-shell edge EELS spectra for these two DLC films. We chose to use the K-shell edge of the EELS spectrum over its low-loss region. Because in addition to possible contributions by surface excitations, it is rather difficult to separate the overlapping contribution of the π and σ transitions in the low loss region [125]. An arc evaporated carbon film and a free standing CVD diamond film, presumed to contain 100% sp^2 and 100% sp^3 carbon bonds, respectively, were used as standards. Their EELS spectra are also shown in Figure 4-36 for comparison. All data were collected in one session to minimize the uncertainties caused by different probing conditions.

Notice in Figure 4-36 that transitions from the carbon 1s core level to the empty π^* antibonding states ($\pi \rightarrow \pi^*$ transitions) caused a strong absorption peak at ~ 285.5 eV for the graphitic carbon film, as a result of its local sp^2 bonding structure. On the other hand, the $\pi \rightarrow \pi^*$ peak is totally absent from the EELS spectrum taken from the CVD diamond film. This is because the sp^3 bonds in diamond contain only σ but no π orbitals. Instead, the 1s $\rightarrow \sigma^*$, or $\sigma \rightarrow \sigma^*$ transitions (transitions from the 1s core level to the σ^* antibonding states) start at a higher energy of about 290 eV. These transitions also lead to distinct near-edge features beyond 290 eV. This extended energy-loss fine structure is analogous to the extended absorption fine structure (EXAFS) in X-ray absorption spectroscopy. In comparison, the EELS spectra for the two DLC samples, which contain a mixture of sp^3 and sp^2 bonded carbon atoms, lie somewhere between that of the graphitic carbon and the CVD diamond. The small $\pi \rightarrow \pi^*$ peaks measured in their EELS spectra suggest their
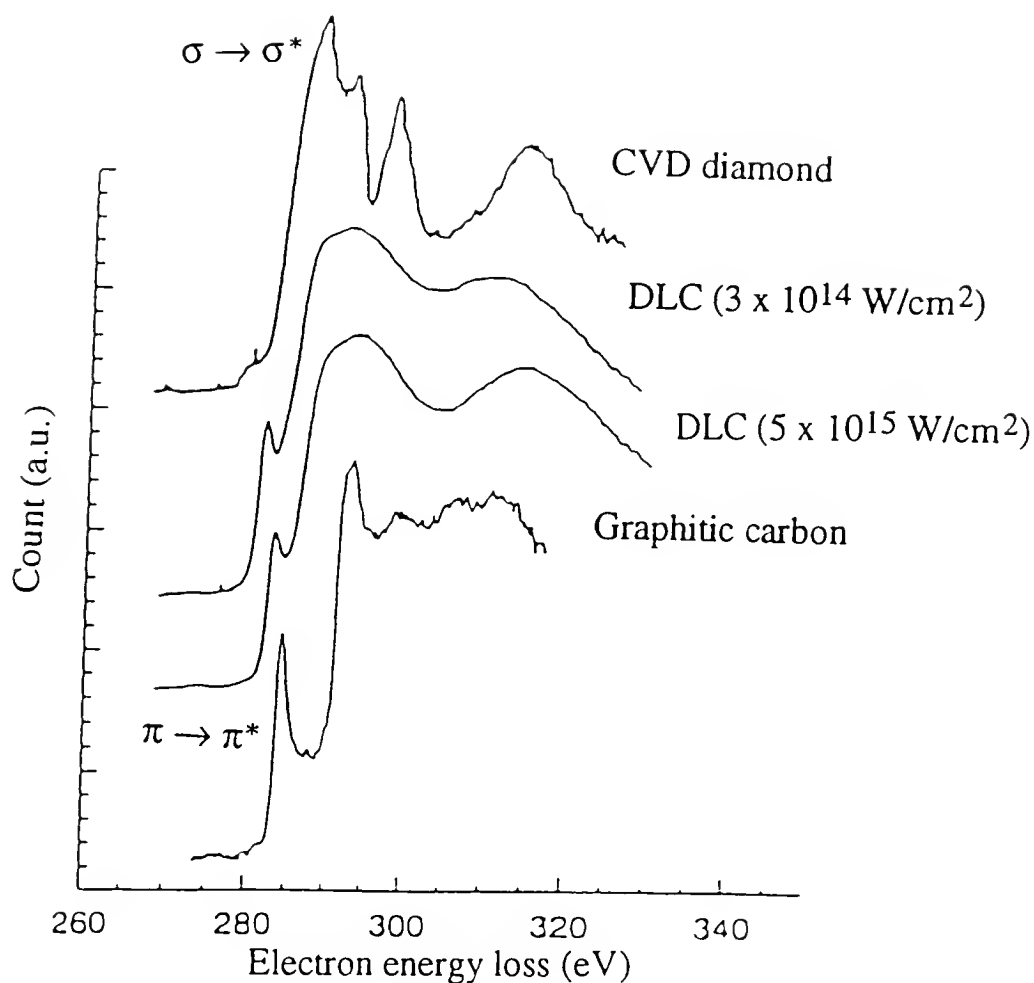
Fig. 4-36 K-shell edge EELS spectra of DLC films deposited by Ti:Sapphire laser at 3 x 10^{14} and 5 x 10^{15} W/cm^2, along with that of a CVD diamond and a graphite film.

diamond-like nature. In addition, due to the amorphous nature of these DLC films, the fine EELS features beyond 290 eV found in the diamond film have been lost.

Because the energy loss signal in a EELS spectrum is derived from primary electron interactions, the number of electrons that have lost energy due to $\pi \rightarrow \pi^*$ and $\sigma \rightarrow \sigma^*$ excitations can be directly estimated by the net integrated intensity of the corresponding peak in the K-shell edge region. A formula for estimating the sp^3 fraction

can be expressed as [50]:

$$\frac{sp^3}{sp^2} = \frac{N_\sigma - 3N_\pi}{4N_\pi} = \frac{(N_\sigma / N_\pi) - 3}{4} \tag{4-7}$$

where

$$\frac{N_\sigma}{N_\pi} = 3\frac{(I_\pi / I_\sigma)_{graphite}}{(I_\pi / I_\sigma)_{DLC}} \tag{4-8}$$

I_π and I_σ in (4.8) are the integrated area underneath the energy window 284 - 289 eV and 290 - 310 eV, respectively. N_σ/N_π is the ratio of the number of σ and π orbitals. It is numerically 3/1 for 100% sp^2 bonds, and 4/0 for 100% sp^3 bonds. Subscripts "graphite" and "DLC" in (4-8) refer to the values obtained from the graphitic carbon film and the as-deposited DLC film, respectively. It has been estimated that the DLC film deposited at 3 x 10^{14} W/cm^2 has a sp^3 fraction of ~ 60%, and the one made at 5 x 10^{15} W/cm^2 has a sp^3 bonded carbon content of ~ 50%. The limiting factors in this estimation include possible bonding state change under the intense electron beam bombardment, as well as the uncertainties involved in background subtraction and integration window cutoffs. To a good approximation, a 10 - 15% margin of error seems to be reasonable [126].

This finding further verifies the results from ellipsometry measurements that the DLC films are more diamond-like at lower laser intensities, for the same reason that the plasma contains particles that are less energetic.

CHAPTER 5
CONCLUSIONS

In summary, we have systematically experimented with the use of intense femtosecond laser beams to deposit thin film materials. Carbon, with its relatively well studied behavior under laser ablation, was selected as the sample material. We have deposited hydrogen-free diamond-like carbon (DLC) films at laser intensities in the 10^{14} - 10^{15} W/cm^2 range, using Ti:Sapphire (100 fs @ FWHM) laser beams. This marks the first time thin film materials have been made in such high intensity regimes, which are at least three orders of magnitude higher than those employed by conventional pulsed laser deposition (PLD) techniques.

The DLC film properties, including their surface topography, optical constants, bonding structure, as well as sp^3 content were studied as a function of laser intensity, with scanning probe microscopy (SPM), variable angle spectroscopic ellipsometry (VASE), Raman spectrometry, and electron energy loss spectroscopy (EELS). Quality DLC films were made at room temperature with good scratch resistance, excellent chemical inertness and high optical transparency in the near infrared (IR) range. Film quality was observed to have decreased as the laser intensity was increased from 3×10^{14} to 6×10^{15} W/cm^2. This was evident by an increased surface particle density, a decreased optical transparency ($85\% \rightarrow 60\%$) and Tauc bandgap ($1.4 \rightarrow 0.8$ eV), as well as a lower tetrahedrally bonded sp^3 carbon atom percentage ($60\% \rightarrow 50\%$).

The formation of laser deposited DLC films is believed to be an ion assisted energetic condensation process, with the carbon particle kinetic energy being one of most important factors affecting the film property. For this reason, the carbon ion kinetic energy as a function of laser intensity was measured with a Faraday ion collector. For the

femtosecond Ti:Sapphire laser induced plasmas, their time-of-flight (TOF) spectra exhibited a double-peak distribution, with a fast moving suprathermal ion component preceding a majority of slower thermal ions. By varying the laser intensity in the 1×10^{14} - 6×10^{15} W/cm^2 range, it was estimated that the most probable ion velocity increased from about 3×10^6 to 1.8×10^7 cm/s. The most probable ion kinetic energy displayed an $I^{0.55}$ dependence, increasing from 60 to over 2000 eV. On the other hand, the suprathermal ions were measured to have kinetic energies ranging from 3 keV to over 20 keV as a function of $I^{0.33}$. Only a small fraction of the carbon particles were made of suprathermal ions. They are believed to be generated by a time dependent electrostatic acceleration field induced by the suprathermal electrons, due to resonant absorption of the intense, p-polarized laser beam.

For comparison, we also deposited DLC films using conventional Nd:YAG (7 ns @ FWHM) laser beams, in the intensity range of 2×10^{10} - 6×10^{11} W/cm^2. It was found that similar to the films deposited with the femtosecond pulses, these DLC films became more absorbing with decreasing Tauc bandgaps (2.4 $\rightarrow$ 0.9 eV), as a function of increasing laser intensity. This was accompanied by a deteriorated surface topography. The nanosecond laser induced plasmas were also studied through TOF experiments. Their TOF spectra exhibited only a single peak distribution, no suprathermal ions were detected. The most probable ion kinetic energy was measured to increase with laser intensity from 200 eV to 1.9 keV as a function of $I^{0.40}$.

We conclude that there is no apparent advantage in the present set-up, to make DLC films with high intensity, femtosecond pulses over conventional nanosecond laser beam. We believe that because of their excessive energy, the highly energetic suprathermal ions in the femtosecond plasma could be detrimental for the DLC film formation. However, it would be interesting to see if femtosecond lasers can be beneficial to the formation of other advanced thin film materials. These include thermodynamically metastable compounds such as c-BN and β-C$_3$N$_4$, where the effective incorporation of

nitrogen ions during film formation has proven to be essential in stabilizing the cubic phases. By using femtosecond pulses, which can generate suprathermal ions with kinetic energies up to several tens of keV, the laser plasma by itself may serve as an ionization source for the background nitrogen gas. In the meantime, the background gas can slow the ions with excessively high energies through collision to moderate values, which could enhance the metastable phase formation.

LIST OF REFERENCES

1. H.O. Pierson, <u>Handbook of Carbon, Graphite, Diamond and Fullerenes</u>, Noyes Publications, Park Ridge, NJ, 1993.

2. S. Aisenberg, R. Chabot, <u>J. Apply. Phys</u>. **42**, 2953 (1971).

3. T. Mori, Y. Namba, <u>J. Appl. Phys</u>. **55**, 3276 (1984).

4. J. Robertson, E.P. O'Reilly, <u>Phys. Rev. B</u>. **35**, 2946 (1987).

5. M. Weiler, S. Sattel, K. Jung, H. Ehrhardt, V.S. Veerasamy, J. Robertson, <u>Appl. Phys. Lett</u>. **64**, 2797 (1994).

6. J. Robertson, <u>Phys. Rev. Lett</u>. **68**, 220 (1992).

7. B. Dischler, A. Bubenzer, P. Koidl, <u>Appl. Phys. Lett</u>. **42**, 636 (1983).

8. J.C. Angus, F. Jansen, <u>J. Vac. Sci. Technol</u>. **A6**, 1778 (1988).

9. C.B. Collins, F. Davanloo, E.M. Juengerman, W.R. Osborn, D.R. Jander, <u>Appl. Phys. Lett</u>. **54**, 216 (1988).

10. J.J. Cuomo, J.P. Doyle, J. Bruley, J.C. Liu, <u>Appl. Phys. Lett</u>. **58**, 466 (1991).

11. S.R. Kasi, H. Kang, J.W. Rabalais, <u>J. Chem. Phys</u>. **88**, 5914 (1988).

12. K. Wasa, S. Hayakawa, <u>Handbook of Sputter Deposition Technology</u>, Noyes Publications, Park Ridge, NJ, 1992.

13. S.D. Berger, D.R. Mckenzie, P.J. Martin, <u>Philos. Mag</u>. **B52**, 285 (1988).

14. A.P. Malshe, S.M. Chaudhari, S.M. Lanetkar, S.B. Ogale, S.V. Rajarshi, S.T. Kshirsagar, <u>J. Mater. Res</u>. **4**, 1238 (1989).

15. K. Deng, W.H. Ko, <u>IEEE Solid-State Sensor and Actuator Workshop</u>. 98, (1992).

16. A.H. Lettington, <u>Phil. Trans. R. Soc. Lond. A</u>. 93 (1993).

17. F.M. Kimock, B.J. Knapp, <u>Surf. Coat. Technol.</u> **56**, 273 (1993).

18. E. Teng, C. Jia, A. Eltoukhy, <u>Surf. Coat. Technol. Proc.</u> **68/69**, 632, (1994).

19. Y. Kokaku, H. Matsumoto, H. Inaba, S. Fujimaki, M. Kitoh, K. Abe, <u>IEEE Transactions on Magnetics.</u> **29**, 3942 (1993).

20. F.X. Lu, B.X. Yang, D.G. Cheng, R.Z. Ye, W.X. Yu, J.B. Sun, <u>Thin Solid Films,</u> **212**, 220 (1992).

21. B. Singh, S. McClelland, F. Tams III, B. Halon, O. Mesker, D. Furst, <u>Appl. Phys. Lett.</u> **57**, 2288 (1990).

22. S.J. Rzad, S.M. Gasworth, C.W. Reed, M.W. DeVre, <u>1992 IEEE 35th International Power Sources Symposium,</u> 358 (1992).

23. R.B. Jackman, L.H. Chua, <u>Diamond Related Mater.</u> **1**, 895 (1992).

24. E. Ohta, Y. Kimura, H. Kondo, M. Takahashi, K. Kameyamma, K, Yamada, I. Fujimura, <u>Extended Abstracts of the 22nd Conference on Solid State Devices and Materials,</u> 589 (1990).

25. S.V. Babu, J. Seth, V.G. Ralchenko, T.V. Kononenko, V.P. Ageev, V.E. Strelnitsky, <u>Thin Solid Films,</u> **254**, 92 (1995).

26. L.A. Thomson, F.C. Law, N. Rushton, J. Franks, <u>Biomater.</u> **12**, 37 (1991).

27. D. Nir, <u>Thin Solid Films,</u> **41**, 112 (1984).

29. S.B. Iyer, K.S. Harshavardhan, V. Kumar, <u>Thin Solid Films,</u> **256**, 94 (1995).

29. Y. Hua, M. Chaker, J.N. Broughton, E. Gat, H. Pépin, T. Gu, X. Bian, M. Sutton, <u>Appl. Phys. Lett.</u> **65**, 830 (1994).

30. M.A. Capano, F. Qian, R.K. Singh, <u>Mat. Res. Soc. Symp. Proc.</u> **285**, 569 (1993).

31. F. Qian, Master's Thesis, University of Florida, 1993.

32. C.W. Ong, S.K. lam, Y. Liu, C.L. Choy, P.W. Chan, X.A. Zhao, J.T. Cheung, <u>Thin Solid Films,</u> **258**, 34 (1995).

33. E.G. Spencer, P.H. Schidt, D.C. Joy, F.J. Salasone, <u>Appl. Phys. Lett.</u> **29**, 118 (1976).

34. D.R. McKenzie, D. Muller, B.A. Pailthorpe, Z.H. Wang, E. Kravtchinskaia, D. Segal, P.B. Lukins, P.D. Swift, P.J. Martin, G. Amaratunga, P.H. Gaskell, A. Saeed, Diamond Related Mater. **1**, 51 (1991).

35. D.R. McKenzie, D. Muller, B.A. Pailthorpe, Phys. Rev. Lett. **67**, 773 (1991).

36. J. Robertson, Phil. Trans. R. Soc. Lond. A. 277 (1993).

37. Y. Lifshitz, S.R. Kasi, J.W. Rabalais, W. Eckstein, Phys. Rev. B. **41**, 10468 (1990).

38. G. Carter, J.S. Colligon, Ion Bombardment of Solids, American Elsevier, New York, 1968.

39. J.A. Thornton, Deposition Technologies for Films and Coatings, Noyes Publications, Park Ridge, NJ,1982.

40. J. Koike, T.E. Mitchell, D.M. Parkin, Apply. Phys. Lett. **60**, 1450 (1992).

41. P.C. Kelires, Phys. Rev. Lett. **68**, 154 (1991).

42. P.J. Fallon, V.S. Veerasamy, C.A. Davis, J. Robertson, G.A.J. Amaratunga, W.1. Milne, J. Koskinen, Phys. Rev. B. **48**, 4777 (1993).

43. F. Rossi, B. André, A. van Veen, P.E. Mijnarends, H. Schut, M.P. Delplancke, W. Gissler, J. Haupt, G. Lucazeau, L. Abello, J. Appl. Phys. **75**, 3121 (1994).

44. S. Fujimori, K. Nagai, Jpn. J. Appl. Phys. **20**, L194 (1981).

45. S. Fujimori, T. Kaisai, T. Inamura, Thin Solid Films, **92**, 71 (1982).

46. C.L. Marquart, R.T. Williams, D.J. Nagel, Mater. Res. Soc. Symp. Proc. **38**, 325 (1985).

47. W. Pompe, H.J. Scheibe, A. Richeter, H.D. Baner, K. Bewilogua, C. Weissmantel, Thin Solid Films, **144**, 77 (1986).

48. T. Sato, S. Furuno, S. Iguchi, M. Hanabusa, Jpn. J. Apply. Phys. **26**, L1487 (1987).

49. C.B. Collins, F. Davanloo, E.M. Juengerman, W.R. Osborn, D.R. Jander, Appl. Phys. Lett. **54**, 216 (1989).

50. D.L. Pappas, K. L. Saenger, J. Bruley, W. Krakow, J.J. Cuomo, T. Gu, R.W. Collins, J. Appl. Phys. **71**, 5675 (1992).

51. P.T. Murray, V.J. Dyhouse, L. Grazulis, D.R. Thomas, Mater. Res. Soc. Proc. **201**,

513 (1991).

52. J. Krishnaswamy, A. Rengan, J. Narayan, K. Vedam, C.J. McHargue, Appl. Phys. Lett. **54**, 2455 (1989).

53. F. Davanloo, E.M. Juengerman, D.R. jander, T.J. Lee, C.B. Collins, J. Appl. Phys. **67**, 2081 (1990).

54. F. Davanloo, E.M. Juengerman, D.R. Jander, T.J. Lee, C.B. Collins, J. Mater. Res. **5**, 2398 (1990).

55. C.B. Collins, F. Davanloo, T.J. Lee, H. Park, J.H. You, J. Vac. Sci. Technol. B. **11**, 1936 (1993).

56. S. Leppävuori, J. Levoska, J. Vaara, O. Kusmartseva, Mat. Res. Soc. Symp. Proc. **285**, 557 (1993).

57. F. Xiong, Y.Y. Wang, V. Leppert, R.P.H. Chang, J. Mater. Res. **8**, 2265 (1993).

58. C.J. Joshi, P.B. Corkum, Physics Today, 36, Jan 1995.

59. S. Watanabe, R.R. Anderson, S. Brorson, G. Dalickas, J.G. Fujimoto, T.J. Flotte, Photochem. and Photobiol. **53**, 757 (1991).

60. P.P. Pronko, S.K. Dutta, J. Squier, J.V. Rudd, G. Mourou, Opt. Comm. **114**, 106 (1995).

61. J. Kruger, SPIE Proc. **2403**, 436 (1995).

62. F. Müller, K. Mann, P. Simon, J.S. Bernstein, G.J. Zaal, SPIE Proc. **1858**, 464 (1993).

63. D.L. Pappas, K. Saenger, J.J. Cuomo, R.W. Dreyfus, J. Appl. Phys. **72**, 3966 (1992).

64. J.J. Cuomo, D.L. Pappas, J. Bruly, J.P. Doyle, K. Saenger, J. Appl. Phys. **70**, 1706 (1991).

65. C. Germain, C. Girault, J. Aubreton, A. Catherinot, Appl. Surf. Sci. **69**, 359 (1993).

66. P.T. Murray, D.T. Peeler, AIP Conference Proceedings 288, Laser Ablation: Mechanism and Applications II. 359 (1994).

67. D.T. Peeler, P.T. Murray, AIP Conference Proceedings 288, Laser Ablation: Mechanism and Applications II. 248 (1994).

68. J. Diaz, S. Ferrer, F. Comin, AIP Conference Proceedings, **288**, 198 (1994).

69. W.S. Fann, R. Storz, H.W.K. Tom, J. Bokor, Phys. Rev. Lett. **68**, 2834 (1992).

70. W.L. Kruer, The Physics of Laser Plasma Interactions, Addison-Wesley, Redwood City, CA, 1988.

71. W.J. Fader, Phys. Fluids. **11**, 2200 (1968).

72. R.K. Singh, Ph.D. Dissertation, North Carolina State University, 1989.

73. T.P. Hughes, Plasma and Laser Light, Wiley, New York, 1975.

74. R. Kelly, R.W. Dreyfus, Nucl. Inst. Meth. **B32**, 341 (1988).

75. J.M. Dawson, Laser Interaction and Related Phenomena, Plenum Press, New York, 1971.

76. H. Puell, Z. Naturforsch, **25a**, 1807 (1970).

77. H. Puell, H.J. Neusser, W. Kaiser, Z. Naturforsch, **25a**, 1815 (1970).

78. R.V. Ambartsumyan, N.G. Basov, B.A. Bouko, V.S. Zuev, Soviet Phys. **21**, 1061 (1965).

79. A.F. Haught, D.H. Polk, Phys. Fluids, **9**, 2047 (1966).

80. W. Demtröder and W. Jantz, Plasma Phys. **12**, 691 (1970).

81. J. Stevefelt, C.B. Collins, J. Phys. D. **24**, 2149 (1991).

82. M. Mattioli, Plasma Phys. **13**, 19 (1971).

83. M.K. Matzen, J.S. Pearlman, Phys. Fluids, **22**, 449 (1979).

84. R.W. Boyd, Nonlinear Optics, Academics Press, Boston, 1992.

85. D. Duston, J. Davis, Phys. Rev. A. **21**, 1664 (1980).

86. X. Liu, Ph.D. Dissertation, University of Michigan, 1994.

87. H. Hora, Plasma at High Temperature and Density, Springer-Verlag, Berlin, 1991.

88. D. Strickland and G. Mourou, Opt. Comm. **56**, 219 (1985).

89. J. Squier and G. Mourou, Laser Focus World, June 1992.

90. J.F. Ready, Effects of High Power Radiation, Academic Press, New York, 1971.

91. A. Braun, G. Korn, X. Liu, D. Du, J. Squier, G. Mourou, Optics. Lett. **20**, 73 (1995).

92. A.E. Siegman, Lasers, University Science Books, Mill Valley, CA, 1986.

93. D.W. Gregg, S.J. Thomas, J. Appl. Phys. **37**, 4313 (1966).

94. M.J. Shea, R.N. Compton, R.L. Hettich, Phys. Rev. A. **42**, 3579 (1990).

95. L. Wiedeman, H. Helvajian, Mat. Res. Soc. Symp. Proc. **285**, 3 (1993).

96. J.P. Zheng, Z.Q. Huang, D.T. Shaw, H.S. Kwok, Appl. Phys. Lett. **54**, 280 (1989).

97. A.W. Ehler, J. Appl. Phys. **46**, 2464 (1975).

98. J.S. Pearlman, J.P. Anthes, Appl. Phys. Lett. **27**, 581 (1975).

99. P.M. Campbell, R.R. Johnson, F.J. Mayer, L.V. Powers, D.C. Slater, Phys. Rev. Lett. **39**, 274 (1977).

100. P.D. Gupta, Y.Y. Tsui, R. Popil, R. Fedosejevs, A.A. Offenberger, Phys. Rev. A. **33**, 3531 (1986).

101. T.P. Hughes, Laser-Plasma Interactions, Proceedings of the Twentieth Scottish Universities Summer School in Physics, R.A. Cairns and J.J. Sanderson eds, 1-90, 1980.

102. D.V. Giovanielli, J.F. Kephart, A.H. Williams, J. Appl. Phys. **47**, 2907 (1976).

103. D.W. Forslund, J.M. Kindel, K. Lee, Phys. Rev. Lett. **39**, 284 (1977).

104. K. Estabrook, W.L. Kruer, Phys. Rev. Lett. **40**, 42 (1978).

105. J.D. Hares, J.D. Kilkenny, M.H. Key, J.G. Lunney, Phys. Rev. Lett. **42**, 1216 (1979).

106. J.P. Freidberg, R.W. Mitchell, R.L. Morse, L.I. Rudsinski, Phys. Rev. Lett. **28**, 795 (1972).

107. M.G. Haines, Laser-Plasma Interactions, Proceedings of the Twentieth Scottish Universities Summer School in Physics, R.A. Cairns and J.J. Sanderson eds, 145-

218, 1980.

108. R.L. Morse, C.W. Nielson, <u>Phys. Fluids,</u> **16**, 909 (1973).

109. E.J. Valeo, I.B. Bernstein, <u>Phys. Fluids,</u> **19**, 1348 (1976).

110. D.H. Reitze, H. Ahn, M.C. Downer, <u>Phys. Rev. B</u>. **45**, 2677 (1992).

111. D.S. Misra, S.B. Palmer, <u>Physica C</u>, **176**, 43 (1991).

112. L.C. Chen, E.L. Hall, <u>Mater. Res. Soc. Symp. Proc</u>. **285**, 519 (1993).

113. P.G. Synder, J.A. Woollam, S.A. Alterovitz, and B. Johs, <u>J. Appl. Phys</u>. **68**, 5925 (1990).

114. F. Demichelis, C.F. Pirri, A. Tagliaferro, <u>Phys. Rev. B</u>. **45**, 14364 (1992).

115. J. Tauc, <u>Amorphous and Liquid Semiconductors</u>, J. Tauc eds, Plenum Press, London, 159-220, 1974.

116. H. Owen, D.E. Battey, M.J. Pelletier, and J.B. Slater, <u>SPIE Proc</u>. **2406**, 260 (1995).

117. D.S. Knight, W.B. White, <u>J. Mater. Res</u>. **4**, 385 (1989).

118. F. Tuinstra, J.L. Koenig, <u>J. Chem. Phys</u>. **53**, 1126 (1970).

119. R.O. Dillon, J.A. Woollam, V. Katkanant, <u>Phys. Rev. B</u>. **29**, 3482 (1984).

120. D. Beeman, J. Silverman, R. Lynds, and M.R. Anderson, <u>Phys. Rev. B</u>. **30**, 870 (1984).

121. K. Enke, <u>Thin Solid Films</u>, **80**, 227 (1981).

122. K. Sinha, J. Menendez, O.F. Sankey, D. A. Johnson, W.J. Varhue, J.N. Kidder, P.W. Pastel, W. Lanford, <u>Appl. Phys. Lett</u>. **60**, 562 (1992).

123. N. Wada, P.J. Gaczi, S.A. Solin, <u>J.Non-Cryst. Solids</u>. **35/36**, 543 (1980).

124. R.F. Egerton, <u>Electron Energy Loss Speactronscopy in the Electron Microscope</u>, Plenum, New York, 1986.

125. S.D.Berger, D.R. McKenzie, P.J. Martin, <u>Phil. Mag. Lett</u>. **57**, 285 (1988).

126. D.N. Belton, S.J. Schmieg, <u>J. Vac. Sci. Technol. A</u>. **8**, 2353 (1990).

BIOGRAPHICAL SKETCH

When asking how one feels about writing a dissertation, I often hear the phrase "Am I glad it is over!". Well, no argument here. There is a brief sign of relief, but more persistent are anticipation and anxiety. Such feelings are not exactly unique, I believe, for someone who has been in school for the most part of his life.
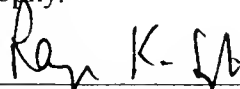
I studied from 1985 to 1990 at Tsinghua University, Beijing, and graduated with two BS degrees, both as majors: one in materials science and the other one in economics. Those were the carefree years, relatively speaking. I earned my master's degree in materials science and engineering in 1993, after two years at the University of Florida. There were good and sometimes less than inviting days, nothing unlike what one would have expected in a wholly new world. I relish what I have learned outside the laboratory just as much as I did inside. Since 1994, as part of a collaborative research project, I have been working as a visiting student at the Center for Ultrafast Optical Science, University of Michigan. This experience has given me a unique opportunity to think and experiment independently, which I hope would someday pay its dividends.

For people who care to go through the preceding pages, it should be fairly obvious, I would hope, that my main research focus has been on thin film materials deposition and characterizations.

Some may be tempted to abstract my life so far as typical of that of a nerd, but I have yet to concede to the very suggestion.
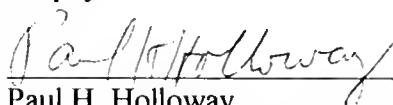
Twenty-eight years is not a short time, it, however, shall not warrant a complete biography, one has to believe. May the coming years be more fruitful.

I certify that I have read this study and that in my opinion it conforms to acceptable standards of scholarly presentation and is fully adequate, in scope and quality, as a dissertation for the degree of Doctor of Philosophy.
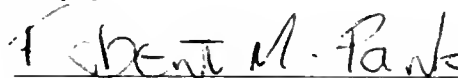
Rajiv K. Singh, Chair
Associate Professor of Materials Science
and Engineering

I certify that I have read this study and that in my opinion it conforms to acceptable standards of scholarly presentation and is fully adequate, in scope and quality, as a dissertation for the degree of Doctor of Philosophy.
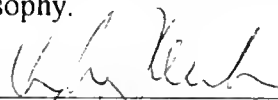
Paul H. Holloway
Professor of Materials Science and
Engineering

I certify that I have read this study and that in my opinion it conforms to acceptable standards of scholarly presentation and is fully adequate, in scope and quality, as a dissertation for the degree of Doctor of Philosophy.
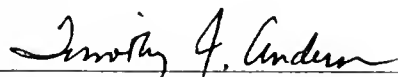
Robert M. Park
Professor of Materials Science and
Engineering

I certify that I have read this study and that in my opinion it conforms to acceptable standards of scholarly presentation and is fully adequate, in scope and quality, as a dissertation for the degree of Doctor of Philosophy.

Stephen J. Pearton
Professor of Materials Science and
Engineering

I certify that I have read this study and that in my opinion it conforms to acceptable standards of scholarly presentation and is fully adequate, in scope and quality, as a dissertation for the degree of Doctor of Philosophy.

Timothy J. Anderson
Professor of Chemical Engineering

I certify that I have read this study and that in my opinion it conforms to acceptable standards of scholarly presentation and is fully adequate, in scope and quality, as a dissertation for the degree of Doctor of Philosophy.

Peter P. Pronko
Research Scientist, Center for Ultrafast
  Optical Science, the University of
  Michigan

This dissertation was submitted to the Graduate Faculty of the College of Engineering and to the Graduate School and was accepted as partial fulfillment of the requirements for the degree of a Doctor of Philosophy.

August, 1996

Winfred M. Phillips
Dean, College of Engineering

Karen A. Holbrook
Dean, Graduate School